

FLOW FIELD PREDICTION AND ANALYSIS PROJECT FIRE

29 MAY 1964

by

M. J. Brunner
C. V. Dohner
V. A. Langelo
H. Rie

NASA Contract No. NAS 1-3418
Langley Research Center
Langley Station, Hampton, Va.



GENERAL  ELECTRIC

RE-ENTRY SYSTEMS DEPARTMENT
A Department Of The Missile and Space Division
3198 Chestnut Street, Philadelphia 4, Penna.

TABLE OF CONTENTS

	Page
TABLE OF CONTENTS.....	i
LIST OF ILLUSTRATIONS	ii
LIST OF TABLES	v
FOREWORD	1
1. Abstract	1
2. Introduction	1
3. Application	2
4. Flow Field Analysis	3
4.1 Analysis.....	3
4.2 Results of Field Flow Analysis	8
4.3 Check on Non-Equilibrium Effects	8
5. FIRE Flow-Heat Transfer Analysis	8
5.1 Analysis	9
5.2 Results	15
6. Spectral Distribution	18
6.1 Analysis.....	18
6.2 Results	23
7. Conclusion	24
Illustrations	25
Tables	75
Nomenclature	104
References	105

LIST OF ILLUSTRATIONS

Figure No.	Title	Page
1	Sketch of FIRE Vehicle Outer Surface After First Beryllium and Ablation Layer Has Been Removed	25
2	Sketch of FIRE Vehicle Showing Shock Shape, 15° Separation Line and Constant Pressure Separation Line	26
3	Lines of Constant Temperature in Subsonic and Transonic Regions of Flow Field	27
4	Lines of Constant Density in Subsonic and Transonic Regions of Flow Field	28
5	Lines of Constant Temperature and Density in Supersonic Region of Flow Field	29
6	Temperature vs x/D on Lines of Constant r/D in Subsonic and transonic Regions	30
7	Electron Density vs x/D on Lines of Constant r/D in Subsonic and Transonic Regions	31
8	O_2 Concentration vs x/D on Lines of Constant r/D in Subsonic and Transonic Regions	32
9	N_2 Concentration vs x/D on Lines of Constant r/D in Subsonic and Transonic Regions	33
10	NO Concentration vs x/D on Lines of Constant r/D in Subsonic and Transonic Regions	34
11	O Concentration vs x/D on Lines of Constant r/D in Subsonic and Transonic Regions	35
12	N Concentration vs x/D on Lines of Constant r/D in Subsonic and Transonic Regions	36
13	O^+ Concentration vs x/D on Lines of Constant r/D in Subsonic and Transonic Regions	37
14	N^+ Concentration vs x/D on Lines of Constant r/D in Subsonic and Transonic Regions	38
15	O^- Concentration vs x/D on Lines of Constant r/D in Subsonic and Transonic Regions	39
16	Temperature vs r/D on Lines of Constant x/D in Supersonic Region of Flow Field	40
17	Density vs r/D on Lines of Constant x/D in Supersonic Region of Flow Field	41

LIST OF ILLUSTRATIONS (CONT)

Figure No.	Title	Page
18	Electron Density vs. r/D on Lines of Constant x/D in Supersonic Region of Flow Field	42
19	O_2 Concentration vs r/D on Lines of Constant x/D in Supersonic Region of Flow Field	43
20	N_2 Concentration vs r/D on Lines of Constant x/D in Supersonic Region of Flow Field	44
21	NO Concentration vs r/D on Lines of Constant x/D in Supersonic Region of Flow Field	45
22	O Concentration vs r/D on Lines of Constant x/D in Supersonic Region of Flow Field	46
23	N Concentration vs r/D on Lines of Constant x/D in Supersonic Region of Flow Field	47
24	O^+ Concentration vs r/D on Lines of Constant x/D in Supersonic Region of Flow Field	48
25	N^+ Concentration vs r/D on Lines of Constant x/D in Supersonic Region of Flow Field	49
26	O^- Concentration vs r/D on Lines of Constant x/D in Supersonic Region of Flow Field	50
27	Streamlines in the Subsonic Region of the Flow Field	51
28	Pressure at the Body Surface	52
29	Mach Number vs x/D on Lines of Constant r/D in Subsonic and Transonic Region of Flow Field	53
30	Mach Number vs r/D on Lines of Constant x/D in Supersonic Region of Flow Field	54
31	Temperature vs Distance Downstream of a Normal Shock for Non-equilibrium Flow	55
32	Density vs Distance Downstream of a Normal Shock for Non-equilibrium Flow	56
33	Spectral Absorptance of Beryllium Oxide	57
34	Laminar Convective Heat Flux on FIRE Vehicle	58
35	Turbulent Convective Heat Flux on FIRE Vehicle	59

LIST OF ILLUSTRATIONS (CONT)

Figure No.	Title	Page
36	Radiative Heat Flux on FIRE Vehicle	60
37	Spectral Steradiancy of N^+ Deionization - Wavelength .05 μ to .16 μ . .	61
38	Spectral Steradiancy of O^+ Deionization - Wavelength .05 to .13 μ . . .	62
39	Spectral Steradiancy of N^+ Deionization - Wavelength .16 to 10 μ	63
40	Spectral Steradiancy of ($N^+ + O^+$) Free-Free - Wavelength16 to 10 μ	64
41	Spectral Steradiancy of O^+ Deionization - Wavelength .16 to 10 μ	65
42	Spectral Steradiancy of O^- Free-Bound - Wavelength .16 to 10 μ	66
43	Spectral Steradiancy of N_2 First Positive - Wavelength .16 to 10 μ . .	67
44	Spectral Steradiancy of N_2 Second Positive - Wavelength .16 to 10 μ	68
45	Spectral Steradiancy of N_2 First Negative - Wavelength .16 to 10 μ . .	69
46	Spectral Steradiancy of O_2 Schumann-Runge - Wavelength .16 to 10 μ	70
47	Spectral Steradiancy of NO Gamma - Wavelength .16 to 10 μ	71
48	Spectral Steradiancy of NO Beta - Wavelength .16 to 10 μ	72
49	Sum of Spectral Steradiancy - Wavelength .05 to 16 μ	73
50	Sum of Spectral Steradiancy - Wavelength .16 to 10 μ	74

LIST OF TABLES

Number	Title	Page
1	Subsonic and Transonic Region-Tabulation of Results	75
2	Supersonic Region-Tabulation of Results	77
3	Shock Wave Shape (x-r) Origin at Stagnation Point)	79
4	Pressure at Body Surface	80
5	Fire Flow Field - Conditions at Stagnation Point	81
6	Laminar Convective Heat Fluxes	82
7	Turbulent Convective Heat Fluxes	83
8	Radiative Heat Fluxes	84
9	Re-Radiative Heat Fluxes	85
10	Spectral Steradiancy N^+ Deionization	86
11	Spectral Steradiancy O^+ Deionization	88
12	Spectral Steradiancy ($N^+ + O^+$) Free-Free	90
13	Spectral Steradiancy O^- Free-Bound	91
14	Spectral Steradiancy N_2 1st. Positive	92
15	Spectral Steradiancy N_2 2nd Positive	93
16	Spectral Steradiancy N_2^+ 1st. Negative	95
17	Spectral Steradiancy O^2 Schumann-Runge	96
18	Spectral Steradiancy NO Gamma	98
19	Spectral Steradiancy NO Beta	100
20	Sum of Spectral Steradiancies	102

FOREWORD

The work reported herein was performed by the General Electric Company, Re-Entry Systems Department, Philadelphia, Pa. under NASA Contract NAS 1-3418. The program was initiated on November 29, 1963 by the Langley Research Center, Langley Station, Hampton, Va. The authors wish to acknowledge the help and guidance throughout the project of R. Dingeldein and D. Cauchon of the Flight Re-Entry Systems Office of NASA/Langley.

The authors wish to acknowledge the assistance of the following consultants who were active participants in this program:

Dr. F. G. Gravalos

Dr. J. M. Botje

Dr. J. B. Gilstein

H. W. Ridyard

J. B. Arnaiz

T. E. Shaw

1. Abstract

The Flow Field Prediction and analysis was determined for the Project FIRE vehicle at flight conditions of 34,582 ft/sec velocity and 171,611 feet altitude for basically equilibrium conditions at zero angle of attack. The flow field predictions were made for the shock shape, local velocity, density, temperature and specie concentration over the vehicle. The heat transfer predictions were made for both the convective (laminar and turbulent) and radiative heat flux input over the vehicle. The spectral distribution was determined at the stagnation point.

12008
Author

2. Introduction

The work presented in this document fulfills the requirements stated in Case I of the statement of work for the Flow Field Prediction and Analysis - Project FIRE #L-2649 dated September 21, 1962 NASA Langley Research Center, Langley Station, Hampton, Va.

NASA has undertaken Project FIRE to provide basic flight research data on the environment associated with re-entry into the earth's atmosphere at superorbital velocity. At the prescribed re-entry conditions heat input from gas radiation and convection will take place at a relatively high level of ionization. The flow field analysis was performed in order to predict the flow field, thermal environment and spectral distribution at the stagnation point. The total program will utilize a flight test vehicle to obtain similar measured flight data. The objective of Project FIRE is to obtain bench mark type data that will define the aerodynamic heating over the entire vehicle and the spectral distribution at the stagnation point.

The Project FIRE flight test vehicle was flown on April 14, 1964. The results of this flight test were not available at the time this report was written.

3. Application

For the purpose of the analysis the Project FIRE vehicle was assumed to re-enter as a ballistic vehicle at 37,000 ft/sec velocity and at -15° re-entry angle. The re-entry package heat shield consists of a series of beryllium and ablation material layers. The outer beryllium layer will be used as a calorimeter to determine the aerodynamic heat input during specific portions of re-entry. The radiation including spectral distribution will be viewed and measured at the stagnation point through an optical window.

The flow field prediction and analysis is based on the configuration when the second calorimeter layer is cleanly exposed. It is assumed that the first calorimeter has been previously melted off and the adjacent layer of ablative material has been ejected. The re-entry configuration for this condition is shown in Figure 1. This condition, which exists prior to the maximum aerodynamic heating rate, is assumed to be at zero angle of attack; for the nominal trajectory the velocity is 34,582 ft/sec at an altitude of 171,611 feet.

The analysis will determine the following:

- a. The state of the gas throughout the flow field extending downstream to approximately the region of wake closure.

- b. The magnitude and the distribution of the convective and radiative heating over the complete re-entry package.
- c. The spectral intensity and distribution of the gas radiation at the stagnation point.

4. Flow Field Analysis

4.1 The flow field in the shock layer surrounding the NASA FIRE vehicle in flight was computed by the method of Gravalos (reference 1). This method is a numerical solution of the laws of conservation of mass, momentum and energy:

$$1) \quad \nabla \cdot (\rho \bar{U}) = 0$$

$$2) \quad \frac{D\bar{U}}{Dt} + \frac{1}{\rho} \nabla p = 0$$

$$3) \quad \frac{DS}{Dt} = 0$$

and the state relations:

$$4) \quad \frac{p}{\rho} = Z RT$$

$$5) \quad S = S(\rho, T)$$

where

$$6) \quad Z = Z(\rho, T), \quad Z = Z(\rho, S)$$

$$7) \quad p = p(\rho, S)$$

$$8) \quad h = h(\rho, S)$$

The last five of these relations are in tabular form, for air treated as a real gas in chemical equilibrium.

The G.E. solution uses a γ^* - gas, where γ^* is defined as:

$$9) \quad \gamma^* = \frac{\rho}{p} \left(\frac{\partial p}{\partial \rho} \right)_s$$

and is computed as a function of s and p using the expression:

$$10) \quad \gamma^* = \frac{a}{p} + b$$

The coefficients a and b are tabulated as functions of entropy and pressure. Reference 1 gives a detailed description of this gas.

The boundary conditions imposed on the problem are: the ambient conditions upstream of the shock wave (applied through the conservation laws at the shock wave); and the statement that no mass can flow through the body surface. Since the mathematical character of the governing equations is different on opposite sides of the sonic line, the solution is carried out in different ways in the subsonic, transonic and supersonic regions of the shock layer. The solution in each of these three regions is computed on an IBM 7094 computer.

4.1.1 Transonic Region

The computation is started in the transonic region, which includes the sonic line and a small part of the shock layer on each side of the sonic line. A coordinate grid of streamlines and the lines normal to them is used. The solution is a direct one. It is started by making an initial estimate of the shock shape and of the pressure distribution at the body surface. The location of a streamline a small distance from the body is then computed (as well as the values of the flow field variables on it), to satisfy the governing equations. This process of stepping to the next streamline is repeated until a new shock

wave location which satisfies the condition of conservation of mass is reached. The shape of this new shock wave, as well as the pressures just downstream of it are compared with the shape and corresponding pressures for the initial estimate. New estimates of shock shape and body pressure distribution are based on this comparison and on a general inspection of the results obtained in the entire transonic region. This iterative cycle is repeated until the estimates and computed values agree closely. In the final iteration of the FIRE flow field solution, pressures agreed within 3%, and the estimated and computed shock wave location nowhere differed by more than 0.5% of the frontal diameter of the vehicle. Computations in the Transonic region were carried out on a total of sixty-six streamlines.

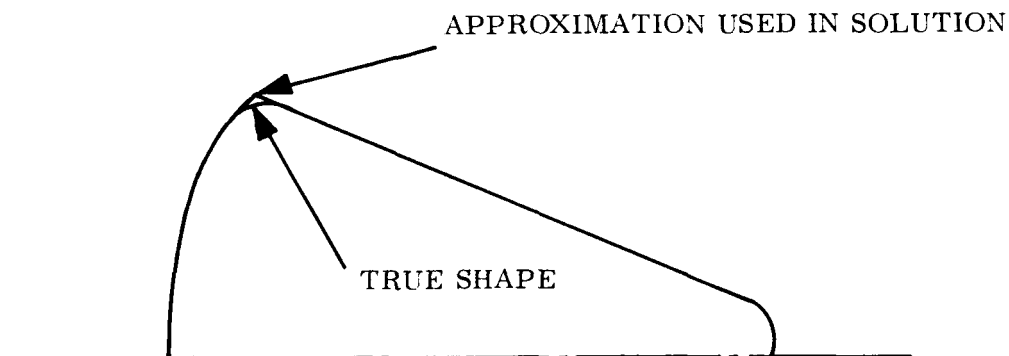
4.1.2 Supersonic Region

The solution in the supersonic region is obtained by the method of characteristics. Values of the flow field parameters along an initial line are provided by the transonic solution.

Since separation was expected in the FIRE flow fields, an estimate of the shape of the separation line was required. It was assumed to be a straight line, 15° from the axial direction, and tangent to the surface of the FIRE vehicle (Figure 2). This choice was based on references 2, 3, and 4, and discussions with Mr. R. Dingeldein of NASA Langley Research Center. The G. E. flow field solution is capable of computing the solution for flow along a constant pressure boundary as well as along a solid boundary. As a check on the chosen separation line, a solution was carried out along a constant pressure line with a pressure equal to that which existed at the upstream end of the 15° separation line (26.25 psf). The resulting separation line fell very near the assumed one as shown in Figure 2.

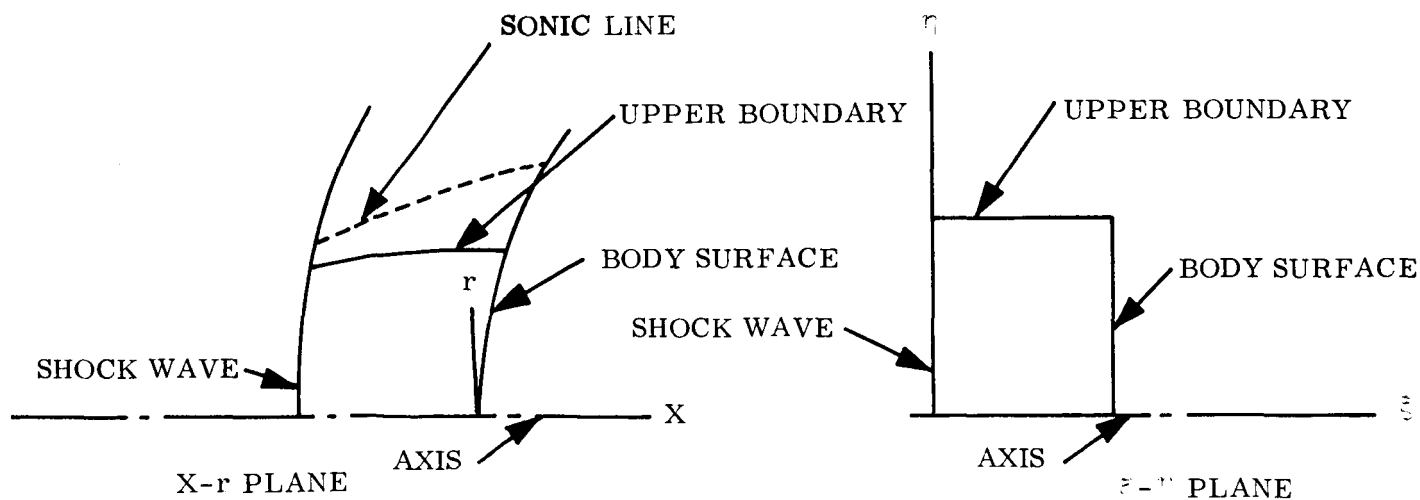
One special procedure was used in the supersonic solution for the FIRE flow field. In order to obtain a valid solution in the vicinity of a large curvature in

the body surface, one must use a very closely spaced characteristics grid. If the body curvature is extremely large, it may be best to approximate it by two straight lines intersecting at a sharp corner. The solution can then be carried out using a Prandtl-Meyer expansion (for real air in chemical equilibrium) at the corner. The latter procedure was used at the suggestion of Dr. F. G. Gravalos.* A sketch (not to scale) of the Fire vehicle profile and of approximation used, is shown below. The approximate shape nowhere differs from the true shape by more than 0.2% of the frontal diameter, and is well within the accuracy of the numerical flow field calculation method.



4.1.3 Subsonic Region

The subsonic solution uses a coordinate transformation which transforms the shock layer between the axis and an upper boundary, into a square. A sketch showing the subsonic region in the physical ($x-r$) plane and in the transformed ($\xi-\eta$) plane appears below.



*A detailed description of the method is given in reference 5.

The governing equations are expressed in terms of the stream function, Ψ :

$$11) \quad A \Psi_{\zeta\zeta} + 2B \Psi_{\zeta\eta} + C \Psi_{\eta\eta} + D \Psi_{\zeta} + E \Psi_{\eta} + F = 0$$

$$\text{where} \quad A = \zeta_x^2 + \zeta_r^2$$

$$B = \zeta_x \eta_x + \zeta_r \eta_r$$

$$C = \eta_x^2 + \eta_r^2$$

$$D = \zeta_{xx} + \eta_{rr} - \frac{\zeta_r}{r} - \frac{A \rho \zeta}{\rho} - \frac{B \rho \eta}{\rho}$$

$$E = \eta_{xx} + \eta_{rr} - \frac{\eta_r}{r} - \frac{B \rho \zeta}{\rho} - \frac{C \rho \eta}{\rho}$$

and

$$F = r^2 \rho^2 \frac{ds}{d\Psi} \frac{p(\rho, s)}{\rho Z(\rho, s)}$$

and as the Bernoulli integral:

$$12) \quad h(\rho, s) + \frac{\frac{\Psi_x^2}{x} + \frac{\Psi_r^2}{r}}{2 r^2 \rho^2} = H$$

The dimensionless entropy, S , is computed at the shock boundary and tabulated as a function of Ψ . It is constant along streamlines. The stagnation enthalpy, H , is constant throughout the field. A solution is obtained by relaxation methods, on a uniform rectangular grid in the ζ - η plane. The "input" information which is obtained from the solution in the transonic region consists of the shock wave shape, and the stream function distribution along the upper boundary of the subsonic region.

4.2 Results of Flow Field Analysis

The results of this analysis include the shape of the bow shock wave, and values of the flow field parameters in the shock layer surrounding the FIRE vehicle in flight at a velocity of 34,582 ft/sec and altitude of 171,611 ft. The results at selected points in the flow field are given in Tables 1 to 5, and are plotted in figures 2 through 30. Temperature, density, Mach number, pressure and shock shape were obtained directly from the flow field solution. Electron density and the various species concentrations were obtained from reference 9 using the local temperatures and densities from the flow field solution.

The stagnation point shock detachment distance was found to be .064 frontal diameters (1.59 inches). This value compares well with the correlations in references 7 and 8.

4.3 Check on Non-Equilibrium Effects

It should be noted that all results presented in section 4 were computed for chemical equilibrium conditions. To check on the validity of these results, a non-equilibrium calculation was carried out for a short distance downstream of a normal shock at the same free stream conditions as the FIRE calculations. The temperature and density reached equilibrium approximately 0.1 inches (approximately 7% of shock detachment distance) downstream of the shock wave. The results of this calculation are shown in figures 31 and 32. This clearly indicates that the air for this flight condition for the FIRE vehicle can be considered to be essentially in chemical equilibrium.

5.0 FIRE Flow Field-Heat Transfer Analysis

The heat transfer analysis for the FIRE vehicle is presented in the following section. Convective, radiative, and reradiative heat flux distributions are analyzed and presented for the FIRE configuration shown in Figure 1.

5.1 Analysis

A. Convective Heating

1. Forebody

The stagnation heat flux for the FIRE vehicle was calculated using Lees' classical laminar solution for hypersonic heating combined with Eckert's reference enthalpy relationship. The equation for this is given (Reference 10) as:

$$13) \quad \dot{q}_0 = \frac{.778}{P_r^{2/3}} \left[\rho^* u^* \left(\frac{du_e}{ds} \right)_{s=0} \right]^{1/2} (h_0 - h_w)$$

This equation is for a hemisphere. Since the FIRE forebody is essentially a cut-hemisphere shape, Reference 8 was used to correct equation (13) for the FIRE vehicle. This amounted to multiplying \dot{q}_0 obtained from equation (13) by the factor 1.072.

For body locations off the stagnation point, both laminar and turbulent heat fluxes were calculated. The off-stagnation point laminar heat fluxes were computed using a compressible reference enthalpy relation based on Lees' solution. The equation for the laminar heat fluxes is given (Reference 10) as:

$$14) \quad \dot{q}_L = \frac{.389}{P_r^{2/3}} \frac{\rho^* u^* U_e r (h_r - h_w)}{\left[\int_0^S \rho^* u^* U_e^2 ds \right]^{1/2}}$$

The off-stagnation point turbulent heat fluxes were computed using the G.E. turbulent integral equation employing Eckert's reference enthalpy relationship. The equation for the turbulent heat fluxes is given (Reference 10) as:

$$15) \dot{q}_t = \frac{.0296}{P_r^{2/3}} \frac{\rho_e U_e \mu_e^{.25} (\mu^*/\mu_e)^{.2} (\rho^*/\rho_e)^{.8} r^{.25} (h_r - h_w)}{\left[\int_0^s \rho_e U_e \mu_e^{.25} r^{1.25} ds \right]^{.2}}$$

This equation satisfies both the momentum and energy integral equations and includes the effect of a finite pressure gradient. The solution was obtained by use of the Blasius incompressible flat plate skin friction coefficients modified for compressible flow employing Eckert's reference enthalpy relationship.

All heat fluxes are based on real gas relationships and properties of air in chemical equilibrium (Reference 12). In addition, the effect of entropy gradients has been factored into the analysis even though these effects may be small for this vehicle.

The pressure at the edge of the boundary layer was obtained from the flow field solution.

2. Afterbody

The convective heat fluxes to the afterbody for the region of separated flow were determined by semi-empirical methods developed from flight test data from the Mark 2 Re-entry Vehicle. Results show the convective heating for laminar and turbulent separated flow, which are given (References 13 and 14) by the following equations:

$$16) \dot{q}_{LD} = .0192 (Re_{\Delta})^{.5} \frac{\mu_e}{\Delta} (h_o - h_w)$$

$$17) \dot{q}_{TD} = .0069 (Re_{\Delta})^{.8} \frac{\mu_e}{\Delta} (h_o - h_w)$$

where

$$18) Re_{\Delta} = \frac{\rho_e U_e \Delta}{\mu_e}$$

Since the Mark 2 configuration resembles the FIRE shape, the convective fluxes calculated for the separated region should be quite accurate.

B. Radiative Heating

In order to calculate the incident and absorbed radiative heat fluxes to the FIRE vehicle, the "Hot Gas Radiation Computer Program" was developed for the IBM 7094 computer. The radiation data available as a tape input covered the spectral region between the wave length of .16 μ and 10 μ . In addition some hand calculations were made for the spectral region of wave length .05 μ to 10 μ . These calculations were based on the results of Reference 15.

1. Hot Gas Radiation Computer Program

The Hot Gas Radiation (HGR) Computer Program was developed from the procedure presented in Reference 16. This program can compute the radiative flux for equilibrium air in the spectral region of wave length .16 μ to 10 μ . Both the fluxes incident on and absorbed by a surface are computed employing the following equations:

$$19) \epsilon_v = 1 - e^{-K_v \Delta r}$$

$$20) B_v = \frac{2hc^2}{\lambda^5} \left[e^{\frac{hc}{kT\lambda}} - 1 \right]^{-1}$$

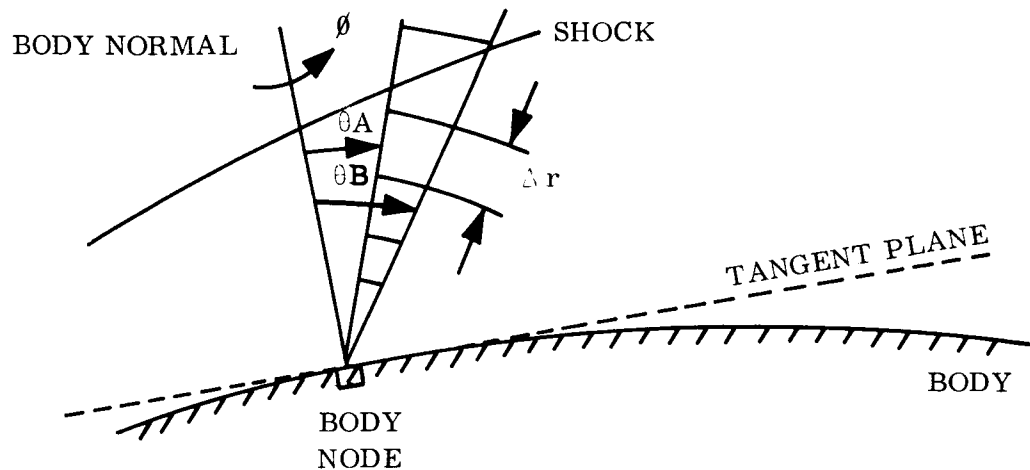
$$21) \dot{q}_{HG \vee \text{INCIDENT}} = \epsilon_{\vee} B_{\vee} \left(\frac{\sin^2 \theta_B - \sin^2 \theta_A}{2} \right) \Delta \theta \prod_i \tau_i$$

$$22) \dot{q}_{HG \vee \text{ABSORBED}} = \alpha_{\vee} \dot{q}_{HG \vee \text{INCIDENT}}$$

$$23) \dot{q}_{HG \text{INCIDENT}} = \sum_{\vee} \dot{q}_{HG \vee \text{INCIDENT}}$$

$$24) \dot{q}_{HG \text{ABSORBED}} = \sum_{\vee} \dot{q}_{HG \vee \text{ABSORBED}}$$

A hemispherical geometry is assumed as illustrated by the following sketch:



The radiation data of Breene, et al (Reference 17) is used as tape input to determine K_{\vee} in equation (19) (as a function of T and ρ).

Several features have been incorporated into the HGR Program to make it more accurate and increase its versatility. These features are briefly discussed below.

- 1) Absorptance (α) of the vehicle surface may be specified as a function of wavelength (λ), i. e., α_λ is the input. This is necessary for obtaining an accurate value for absorbed radiative flux, since the contributions to the radiative flux from different regions of the spectrum vary markedly in magnitude.
- 2) Emissivity of an incremental volume of the hot gas is calculated according to equation (19) and consequently is applicable for non-optically thin gases.
- 3) Radiative fluxes from any incremental gas volume or any pencil of rays may be calculated.
- 4) Absorption of part of the radiative flux by intermediate gas volumes (i. e., volumes between the emitting volume and the vehicle surface) is included assuming non-optically thin gases.

2. Hand Calculations

As stated previously, several hand calculations (in addition to those made for purposes of checking the HGR Program) were made to extend the spectral region of the calculated incident and absorbed radiative fluxes. These hand calculations were made for wavelengths from $.05\mu$ to 10μ ; the total radiance values given in Reference 15 were employed.

For these hand calculations, the gas layer was broken up into volume increments (similar to the method used for the HGR Program), and the contribution of radiative heating from each increment was determined. It was assumed that the gas was nearly optically thin, so that absorption of the radiation by intermediate gas volumes could be neglected. The incident radiative fluxes in the $.05\mu$ to 10μ region were calculated, and the absorbed radiative fluxes were found according to:

$$\begin{aligned}
 25) \quad \dot{q}_{.05 - 10\mu \text{ ABSORBED}} &= \dot{q}_{.16 - 10\mu \text{ ABSORBED}} + \\
 &\alpha_{.05 - .16\mu} (\dot{q}_{.05 - 10\mu \text{ INCIDENT}} \\
 &\quad - \dot{q}_{.16 - 10\mu \text{ INCIDENT}})
 \end{aligned}$$

It was assumed that the surface of the FIRE beryllium calorimeter would oxidize to form beryllium oxide (BeO). The values of α_{λ} for BeO were taken from reflectance data given in Reference 18 and are shown in Figure 33. The dashed lines in Figure 33 are extrapolations of the data. It may be seen that $\alpha_{.05 - .16\mu} = .9$.

This value was used in equation (25).

C. Re-radiative Cooling

The equation used for the re-radiative heat flux from the FIRE vehicle was:

$$26) \quad \dot{q}_{RR} = \epsilon \sigma T^4$$

For (BeO), it was assumed that $\epsilon = .6$ (Reference 18).

5.2 Results

A. Laminar Convective Heating

Figure 34 and Table 6 present the values of laminar convective heat flux versus body axial location (X). The calculations were made with wall temperature (T_w) as a parameter, and are shown for $T_w = 0, 1000, 2000$, and 2800°R . (The temperature $T_w = 2800^\circ\text{R}$ was assumed as the melting point of beryllium.) It may be seen from Figure 34 that the heating decreases as you move away from the stagnation point, and then increases again near the sonic throat, where the convective heating is almost as high as at the stagnation point. Upon leaving the sonic throat the heating decreases again, and is quite small over the afterbody portion of the vehicle.

B. Turbulent Convective Heating

Figure 35 and Table 7 present the values of turbulent convective heat flux versus body axial location (X). Again the wall temperature values of $T_w = 0, 1000, 2000$, and 2800°R were used as parameters. It should be noted that although the turbulent convective heat flux values are given, turbulent flow is not expected to occur, since the value of the local Reynolds numbers (based on wetted length) calculated for the FIRE vehicle (at a 171,611 ft. altitude and 34,582 fps velocity) were less than 35,000 (Table 7). For blunt bodies, experience indicates that transition can be expected to occur at a Local Reynolds number of 150,000. Hence, the laminar heat fluxes should be the ones of real significance.

When a boundary layer becomes relatively thick compared to the shock stand off distance from the body, vorticity effects will occur. The outer edge conditions of the viscous merged boundary shock layer are not based on an isentropic analysis. The boundary layer thickness for the case studied in this report was found to be only 10% or less of the corresponding shock layer thickness. Since the boundary layer thickness is a relatively small portion of the total shock stand off distance, vorticity effects have been considered to be negligible.

C. Radiative Heating

Figure 36 and Table 8 present the values of radiative heat flux versus axial location (X). The incident and absorbed radiative heat fluxes are both plotted for the spectral regions of wave length from $.16\mu$ to 10μ and $.05\mu$ to 10μ . The absorptance used for calculating the absorbed fluxes was obtained from reflectance data for Beryllium oxide BeO (Reference 18). This is shown in Figure 33.

It may be seen from Figure 36 that the hand calculations (based on Reference 15) for the spectral region from $.05\mu$ to 10μ show the absorbed radiative heat flux at the stagnation point ($875 \text{ BTU/sec. ft}^2$.) to be larger in magnitude than the convective heat flux at the stagnation point ($654 \text{ BTU/sec. ft}^2$, for $T_w = 0^\circ\text{R}$). The absorbed radiative heat flux for the spectral range from $.16\mu$ to 10μ , however, is only $173 \text{ BTU/ft}^2\text{sec}$, which is considerably lower than the convective heat flux.

D. Radiation Coupling of Flow Field

It should be noted that the information presented in this report concerning the flow field, heat transfer and spectral distribution at the stagnation point is based on the flow field properties derived in Section 4. When

the gas cap radiation is appreciable, however, the local flow field properties (especially the temperature) may be affected since the temperature may be reduced due to the energy radiated away from the flow field.

In order to evaluate the possible magnitude of this coupling effect, the region at the stagnation point will be examined. Any coupling existing at the stagnation point will be a maximum since the radiation at this location is a maximum. The radiation enthalpy can be compared to the flow field enthalpy to indicate the extent of the coupling. The resulting coupled temperature may be evaluated by reducing the local flow field enthalpy by the enthalpy loss due to radiation. A new temperature can then be obtained at this point. The radiation enthalpy may be defined as:

$$27) \ h_{\text{RAD}} = \frac{J}{\rho} \frac{\delta}{U}$$

Where the term (δ/U) denotes the resident time in the streamline increment. Using this new flow field temperature a new value of the radiance was obtained. This procedure was repeated until the radiance matched the requirements of the radiation enthalpy and flow field temperature. The coupling between the radiation and the flow field may be evaluated by the coupling ratio (F_r) where

$$28) \ F_r = \frac{h_{\text{RAD}}}{h_{\text{FLOW FIELD (UNCOUPLD)}}}$$

Since the amount of radiation is a function of the wave length range (see Figure 36) the amount of coupling will also depend on the wave length range. Radiation coupling (F_r) at the stagnation point can vary from about 4.3% to 1.8% for spectral ranges of .05 to 10μ and .16 to 10μ respectively. It is noted that although the radiation coupling for this case seems relatively small, its influence on the radiation heat flux may be considerably greater. The radiation heat flux with coupling will be about 65% and 90%

of the non-coupled radiation for the spectral ranges of $.05$ to 10μ and $.16$ to 10μ respectively. The coupling effect at other locations on the vehicle will not only be considerably less than at the stagnation point but will be more complicated to evaluate due to the variations in local properties across the shock.

E. Re-radiative Cooling

The re-radiative heat fluxes are given in Table 9 for the wall temperatures of $T_w = 0, 1000, 2000,$ and 2800°R . These values are based on $\epsilon = .6$ and are applicable at any body station.

6. Spectral Distribution

6.1 Analysis

The properties of the gas in the shock layer were defined in Section 4. Once the temperature and concentration distribution was determined, the radiation from each of the species in the flow was determined over the complete spectrum of interest. The method used to accomplish this task was the method of Breene, et al (Reference 15). The important radiating species of high temperature air for several selected temperatures and density ratios for equilibrium air have been determined in Reference 15. The method covers radiation in the ultraviolet, visible and infrared range for both the band spectra and continua radiation. The radiation is treated in four parts, namely, ultraviolet band spectra, infrared band spectra, bound free continua and free-free continua. The ultraviolet band radiation consists of the beta system and gamma system of nitric oxide, the Schumann - Runge system of oxygen, the first and second positive system of nitrogen and the first negative system of the positive nitrogen ion. The infrared spectra is determined entirely by the infrared spectrum of nitric oxide. The bound-free continua radiation is determined from the bound-free continuum of oxygen, and the deionization continuum of the oxygen and

nitrogen. The final spectra contributing to the radiation are the free-free continua which is comprised of the free-free continua of oxygen and nitrogen, and of the free-free continua of singly and doubly ionized nitrogen and oxygen. A brief description of the method will be given here for completeness, but the reader is referred to references 15 and 17 for more detailed explanation.

For the ultraviolet-visible band spectra the frequency dependent emissivity is given by

$$29) \quad e_{\nu} = 1 - e^{-D \sum K}$$

where

$$D = L \frac{\pi e^2}{mc^2} \left[N \frac{1}{1 - e^{-h\nu/kT}} \right]$$

and

$$K = \left(\frac{f_{nm}}{2 |B_{\nu'} - B_{\nu}|} \right) \frac{g}{Q} \exp \left[\frac{-hc G_{el, \nu}}{kT} \right] \exp \left[\frac{-hc B_{\nu}}{kT} \right] \\ \times \left[\frac{\nu - \nu_{\nu\nu'}}{B_{\nu'} - B_{\nu}} \right]$$

The K is the absorption coefficient and other symbols are as defined in Reference 15 and the table of symbols herein. It should be emphasized at this point that the oscillator strengths f_{nm} are obtained from experimental measurements and uncertainties in these critical constants are directly reflected in uncertainties in the resulting calculated emissivities. Reference 15 presents a comparison of calculations with those of other investigators.

Infrared Band Systems

The basic assumption used here is that the rotational constants are practically the same in the upper and lower states for rotational-vibrational bands.

The equation for the emissivity is:

$$30) \quad \epsilon_{\nu} = 1 - e^{-D \sum K}$$

where

$$K = \frac{f_{\nu\nu'} \nu - \nu_{\nu\nu'}}{4 B_v^2 Q} \exp \left[\left(-\frac{G_v}{kT} \right) (\nu - \nu_{\nu\nu'})^2 \left(\frac{h}{4 B_v kT} \right) \left(- \left(\nu - \nu_{\nu\nu'} \right) \frac{hc}{2kT} \right) \right]$$

$$D = L \frac{\pi e^2}{mc^2} N \left[1 - e^{-(h\nu/kT)} \right]$$

Since no electronic transitions take place in this spectral range, the oscillator strength will be simply that of the vibration transition.

Continua Radiation

A. Bound-Free Continua

Collisions between electrons and ions in electron capture can be quantitatively described in terms of suitable collision cross sections. The spectral absorption coefficient of such processes is related to the cross section of electron capture.

$$31) \quad K = \sigma_c N Q$$

where Q is the partition function

N is the number density of the particles.

The radiation, or emission of a photon, results from the capture of an electron by a negative ion (O^-). The cross section for the bound free continua of O^- are experimental results by Branscomb using the method of Breene, et al (Reference 15).

B. N^+ and O^+ Deionization

Again the absorption coefficient is a function of the cross section of collision. Here the cross section of electron capture by a positive ion (N^+ or O^+) was obtained by Bates. The ionization cross section is related to the capture cross section determined by Bates.

Free-Free Continua

This type of radiation arises from transitions between different states of an electron in the presence of the particular atom. Here again the cross sections provide the key to the calculation of the radiation.

The results provided herein for the spectral gas radiation include the major species, such as, N^+ and O^+ deionization, N_2^+ first negative, N_2 first and second positive, O_2 Schumann-Runge, and NO band systems $O^+ + N^+$ free-free, and O^- free bound continua. The method of calculation used was that of reference 17 according to the formula discussed in section 6.1. In order to provide useful information for comparison with flight test data, the spectral radiation is presented in the form of steradiancy is defined as the radiant flux emitted per unit

of solid angle per unit area of the projection of the emitted surface on a solid angle per unit area of the projection of the emitted surface on a plane perpendicular to the direction of observation (watts/cm^2 steradian). In the case of a volume of gas emitting radiation, such radiation can still be considered as steradiancy except for the units of volume instead of area. The energy reaching the collector is a function of its surface area and the square of the distance away from the source of the radiation. In order to determine the energy reaching the collector, one must know the surface area of the collector and its distance from the shock as well as the viewing angle of the radiometer. It was indicated from telephone conversations that the view angle was 7° at the stagnation point. This appears likely that the radiometer may be somewhat inside of the vehicle and have a finite surface area of collectors somewhat greater than implied by the 7° angle alone. If the apex of the 7° angle is 10cm inside of the vehicle, the volume of gas seen by the radiometer will be 6.88 cm^3 as compared with $.266 \text{ cm}^3$ if the 7° apex is at the stagnation point of the body. A simple expression can be used for the conversion of results given here for conditions at the stagnation point to data comparable with flight test results. Let us define the quantities r_i , A , and V_i as the distance between the emitting gas and the collector surface in cm, the collector area in cm^2 and the incremental volume of hit air in cm^3 , respectively. Thus the formula for the multiplicative factor is

$$32) \quad F_S = A \sum_i^n \left(\frac{V_i}{r_i^2} \right) \text{ where } i = 1, 2, \dots, n$$

Once the quantities A , r_i and V_i are known, it is a simple matter to choose an n , where n is the total number of incrementals between the shock and the body, and calculate F . The value of F then is multiplied by the value of the spectral distribution of steradiancy given in curves

37 through 50 to obtain the calculated value of radiation which should reach the collector if the quartz window had a transmissivity of 1.0 for all radiating species of air. This means that the observed radiation due to the hot gases in the shock layer will radiate to a detector area of one square centimeter at the stagnation point the amount presented in the results for each micron of wave length over the ranges given by Reference 15 (.05 μ to 10 μ microns). It is a simple matter to compare the flight test results, once the details of the measurements are known, i.e., the transmissivity of the window and the surface area of the radiometer cells and their wave length band pass.

6.2 Results

The major radiation for the stagnation region is in the ultra-violet and due mostly to N^+ and O^+ deionization band spectra. The N^+ spectral distribution for the .05 μ to .16 μ range appears in Figure 37 and the radiation for O^+ deionization in the same range is plotted on Figure 38. The spectral radiation due to N^+ deionization in the range from .16 μ to 10 μ is shown on Figure 39. The (N^+ and O^+) free-free continua contribution is shown on Figure 40 from .16 to 10 μ . These are the major contributors for the gas radiation from .05 μ to 10 μ . All of the other systems are orders of magnitude less radiation. However, these are also shown on Figures 41 to 48. The sum of the spectral radiation for all these processes is shown on Figures 49 and 50. Since the values of the absorption coefficients calculated by the method Reference 15 are considered zero when the value falls below a given value, the results shown on these figures are necessarily spotty.

It should be noted that the spectral distribution and the radiative flux evaluation were based on the data presented in reference 15. At the present time the authors are re-evaluating this information. It is

believed that re-evaluation may reduce the N^+ and O^+ deionization in the ultraviolet region (.05 to .2 μ wave length). The complete details of the change will be forthcoming in the near future.

7. Conclusions

The flight predictions were calculated for the flow field, heat transfer and spectral distribution of the FIRE vehicle at conditions after the first beryllium calorimeter and ablation layer are removed at 34,582 ft/sec velocity and 171,611 ft altitude for zero angle of attack.

The flow field was calculated using the Gravalos solution for the subsonic, transonic, and supersonic portion of the vehicle. The flow field properties between the body and shock were determined over the entire vehicle. The shock shape, temperature, pressure, density, local Mach number and specie concentration were specified throughout the flow field.

The heat input over the entire vehicle was calculated. The convective (Laminar and turbulent), radiation (incident and absorbed) and the re-radiation heat flux were obtained for assumed wall temperatures of 0, 1000, 2000, and 2800°R. The radiative heat flux was determined for wave length ranges from .05 μ to 10 μ utilizing Breene's radiation data.

The spectral distribution was obtained at the stagnation point for radiation in the ultraviolet, visible and infrared range for both the band spectra and continua radiation. The radiation was treated in four parts namely ultraviolet band spectra, infrared band spectra, bound-free continua and free-free continua.

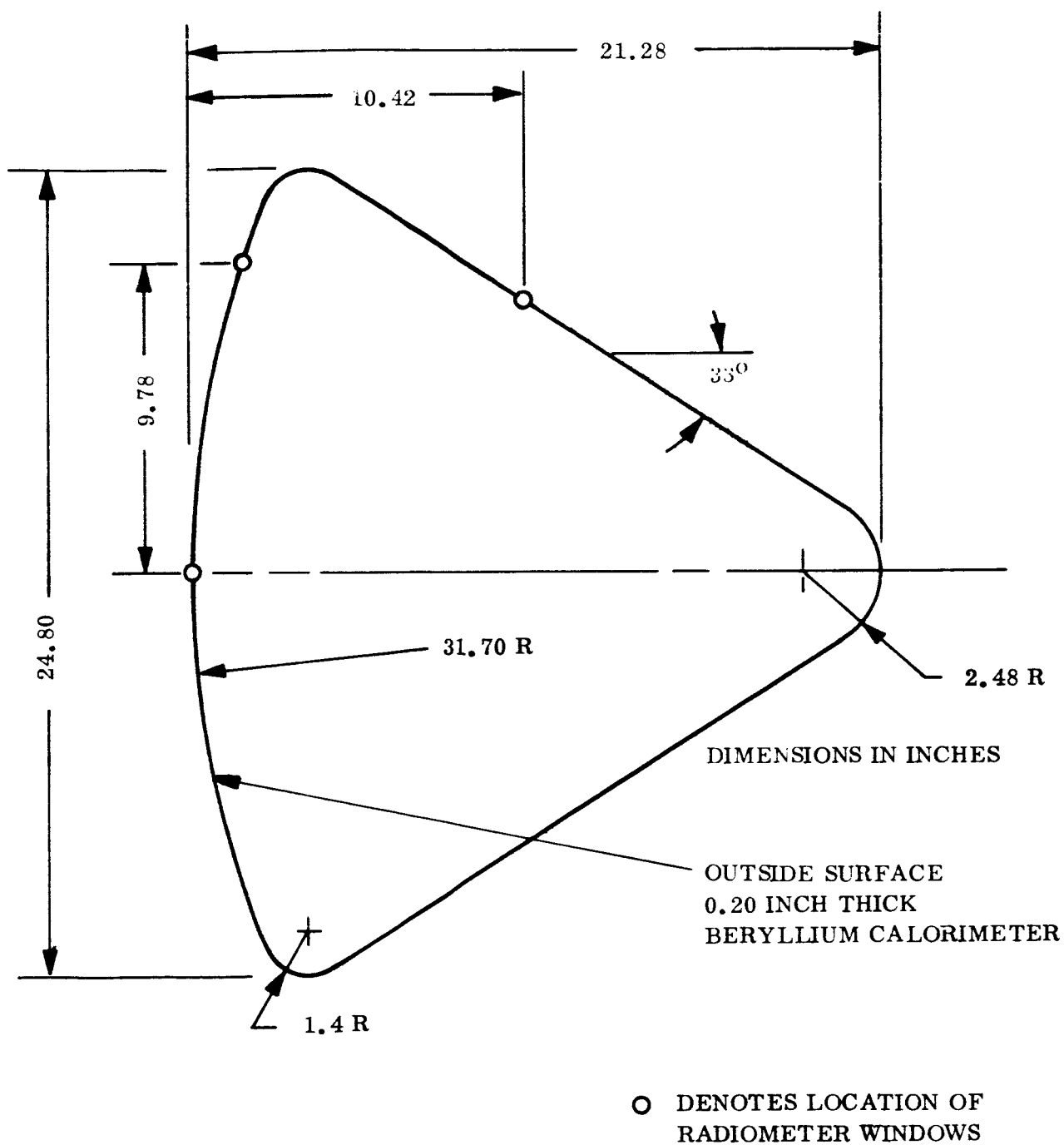


Figure 1. Sketch of FIRE Vehicle Outer Surface After First Beryllium and Ablation Layer Has Been Removed

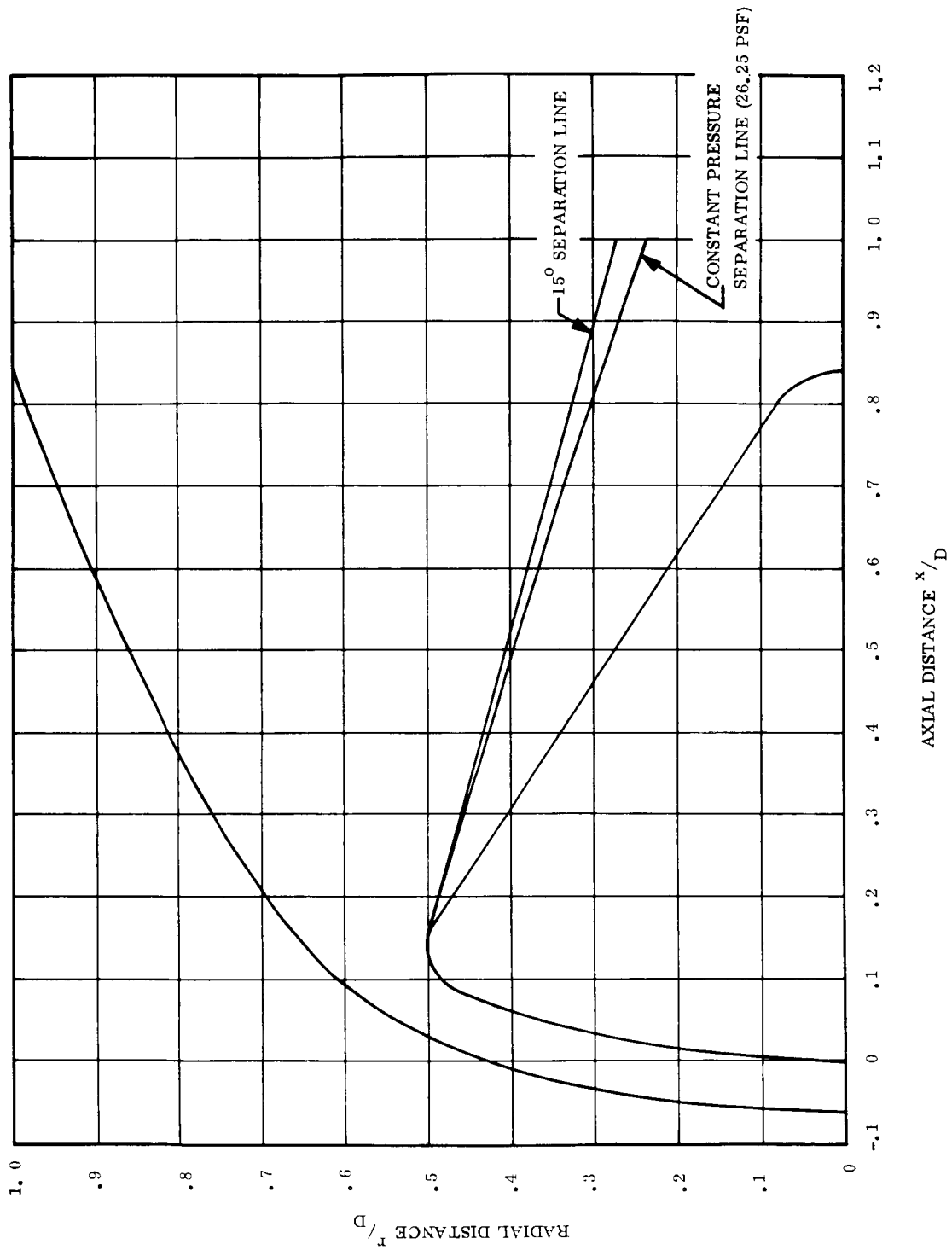


Figure 2. Sketch of FIRE Vehicle Showing Shock Shape, 15° Separation Line and Constant Pressure Separation Line

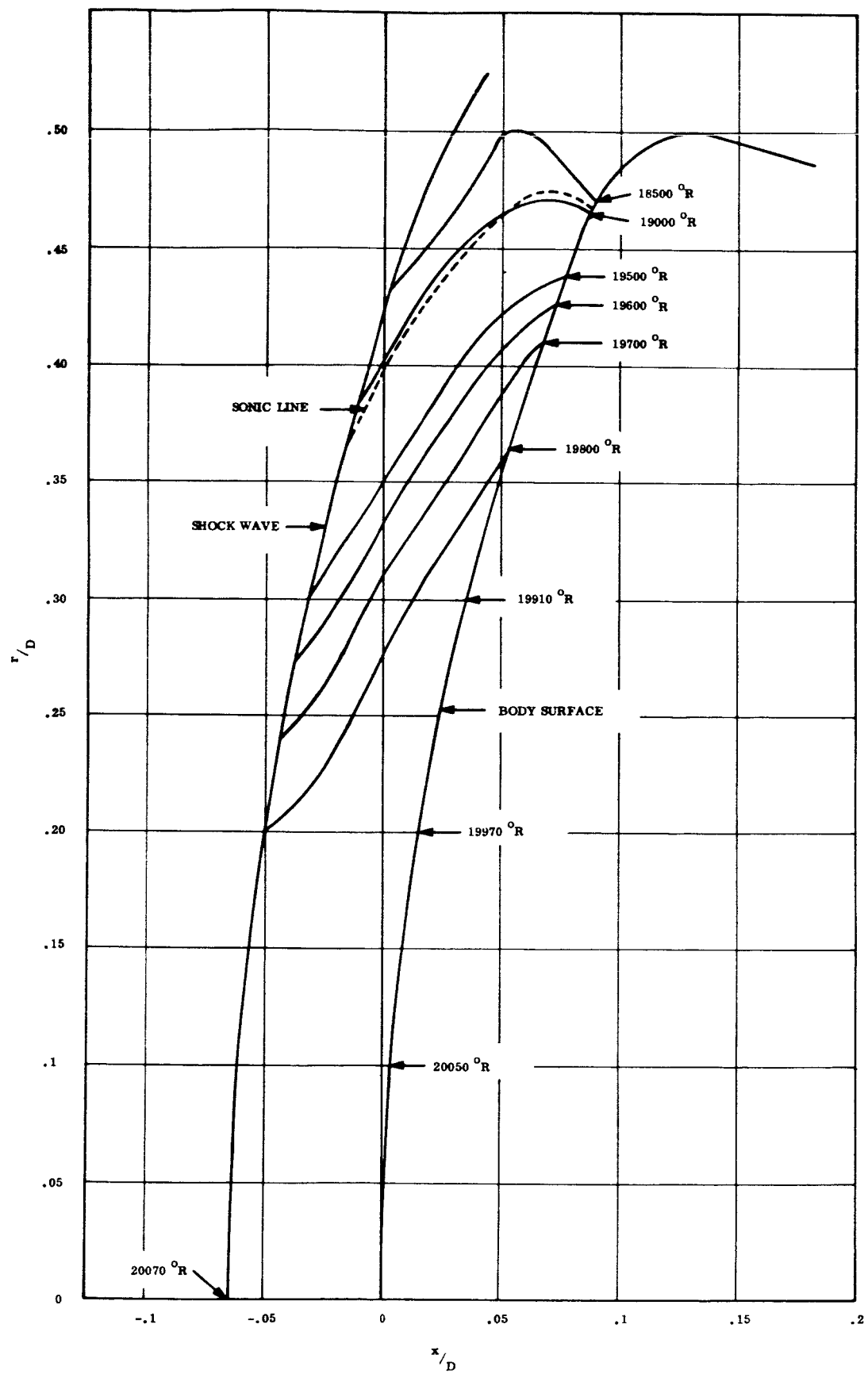


Figure 3. Lines of Constant Temperature in Subsonic and Transonic Regions of Flow Field

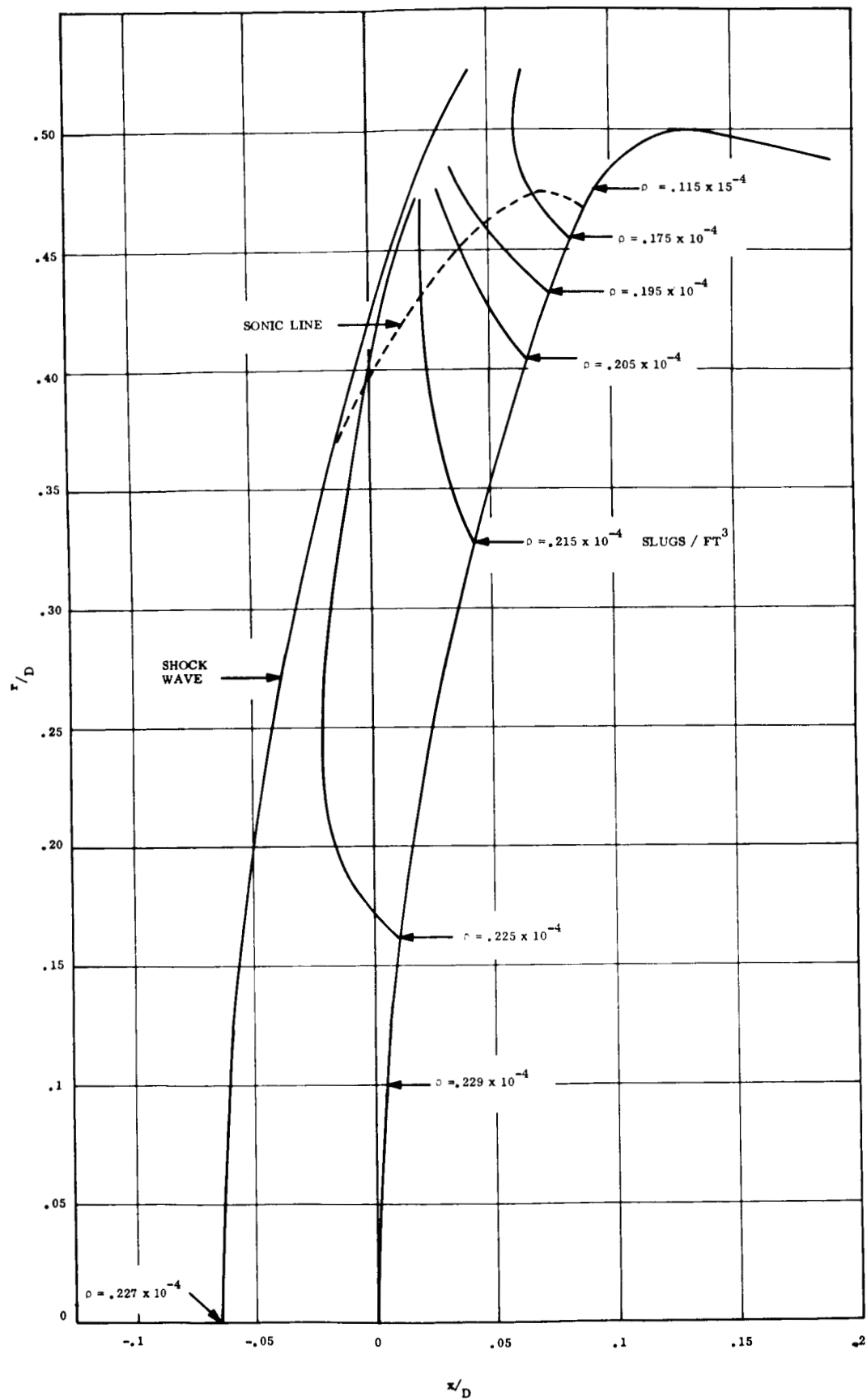


Figure 4. Lines of Constant Density in Subsonic and Transonic Regions of Flow Field

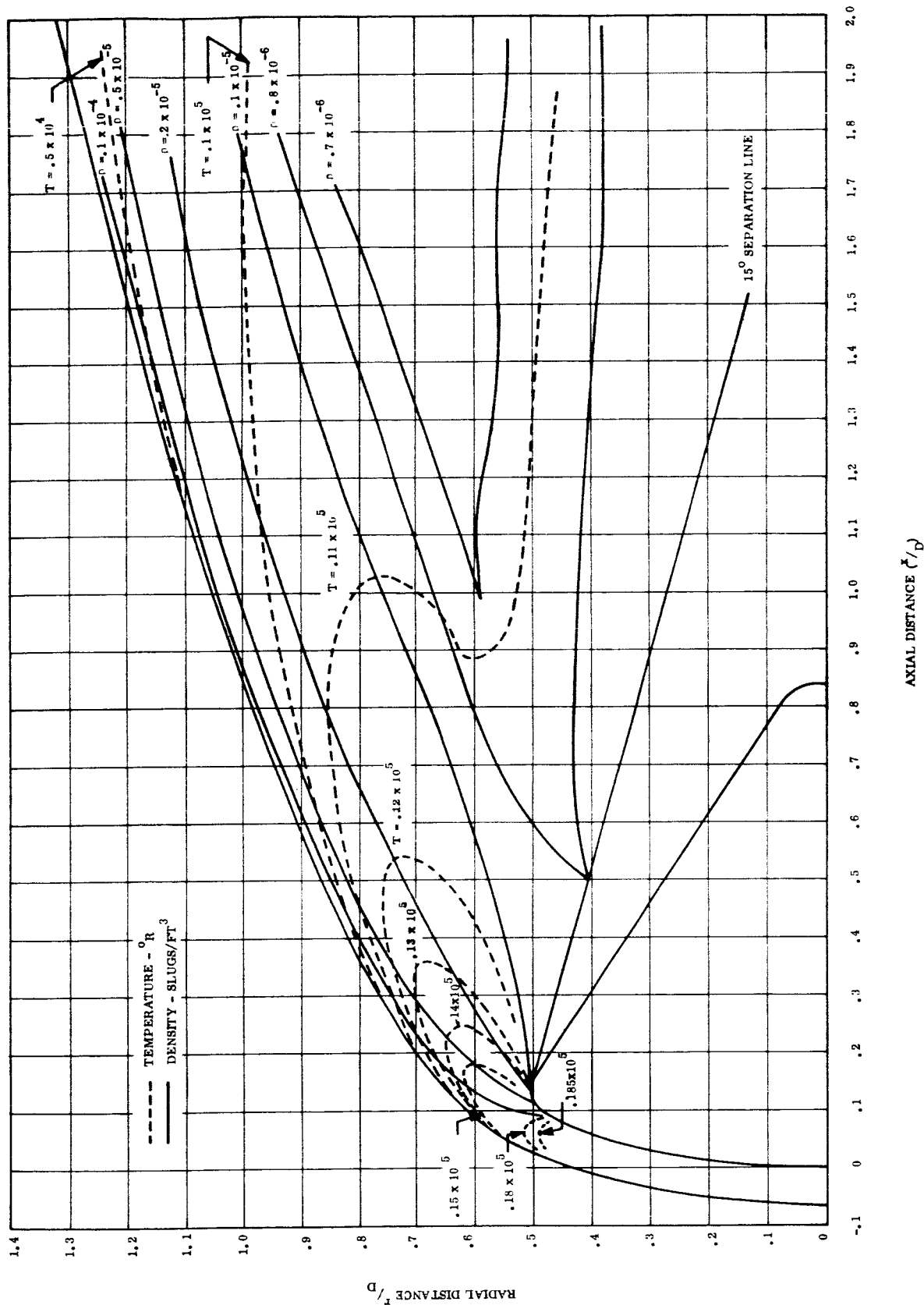


Figure 5. Lines of Constant Temperature and Density in Supersonic Region of Flow Field

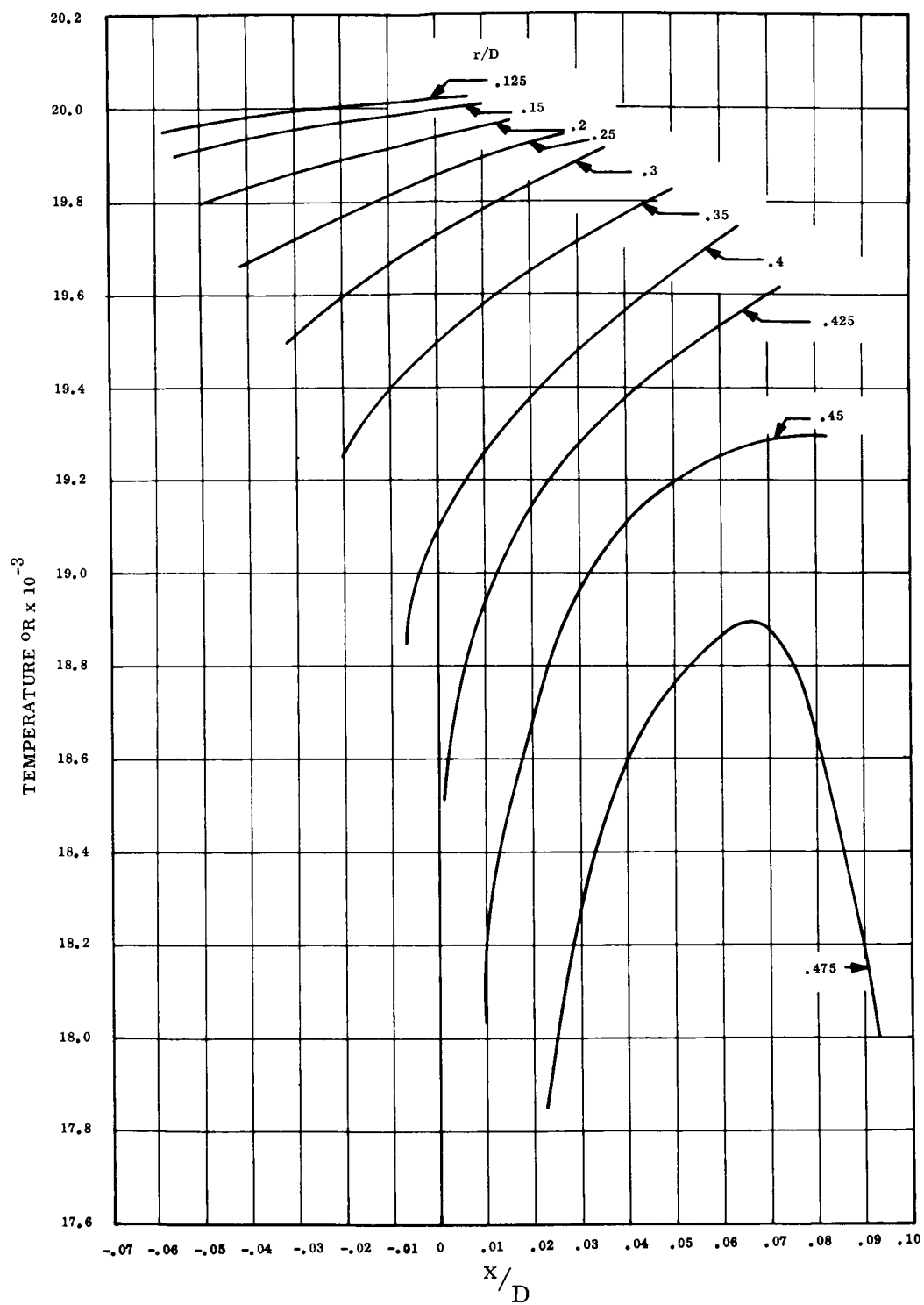


Figure 6. Temperature vs X/D on Lines of Constant r/D in Subsonic and Transonic Regions

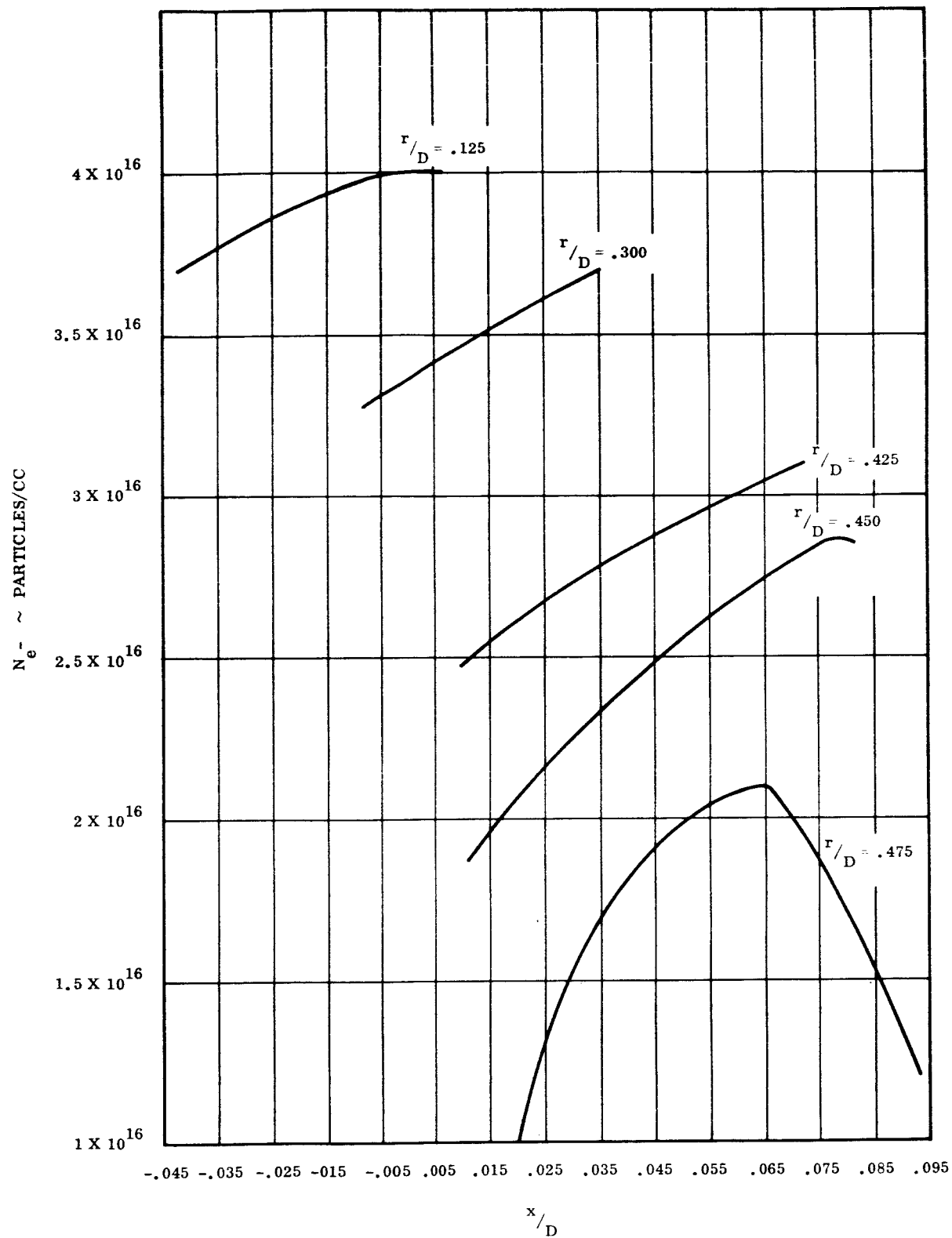


Figure 7. Electron Density vs x/D on Lines of Constant r/D in Subsonic and Transonic Regions

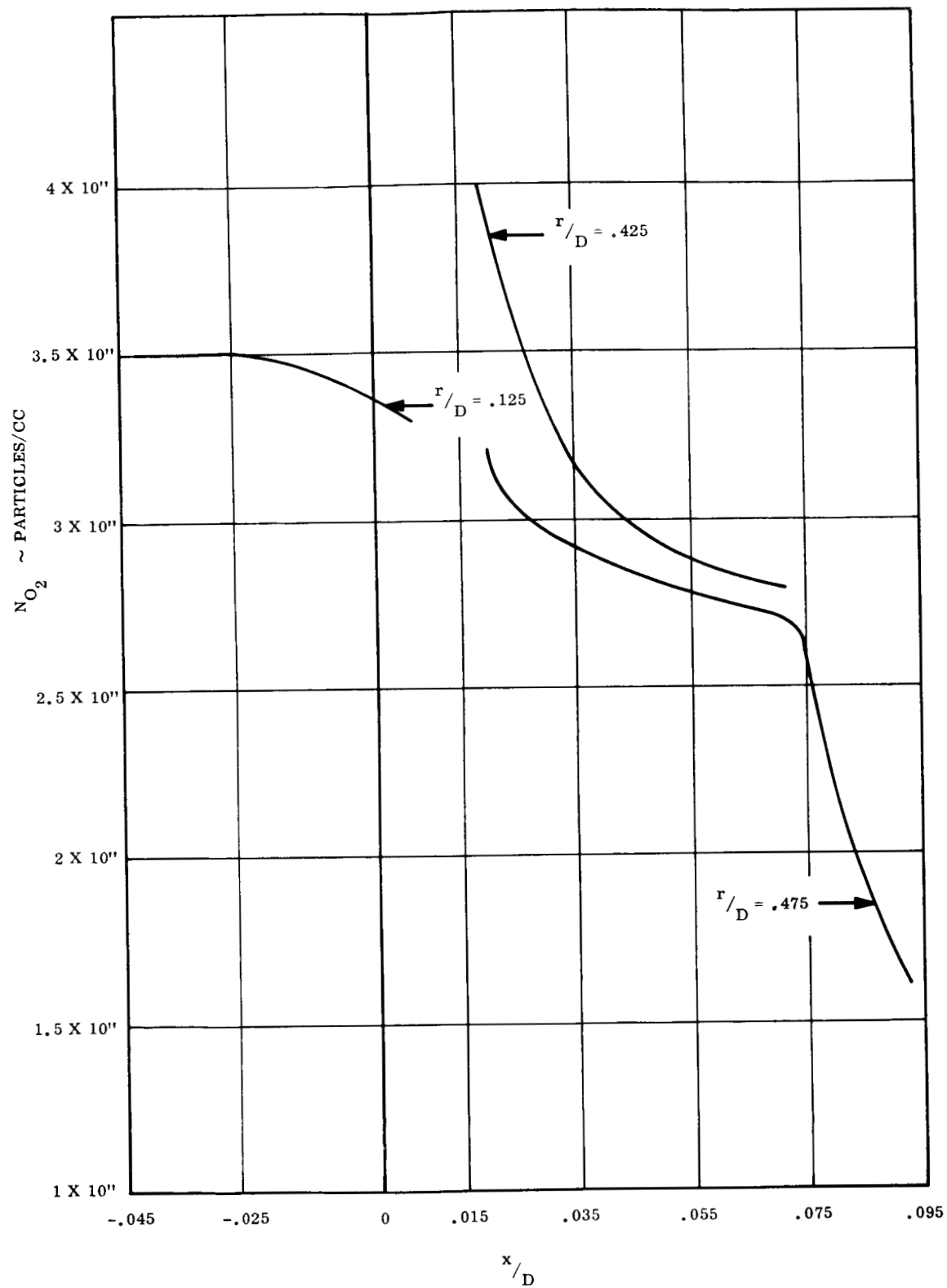


Figure 8. O_2 Concentration vs x/D on Lines of Constant r/D in Subsonic and Transonic Regions

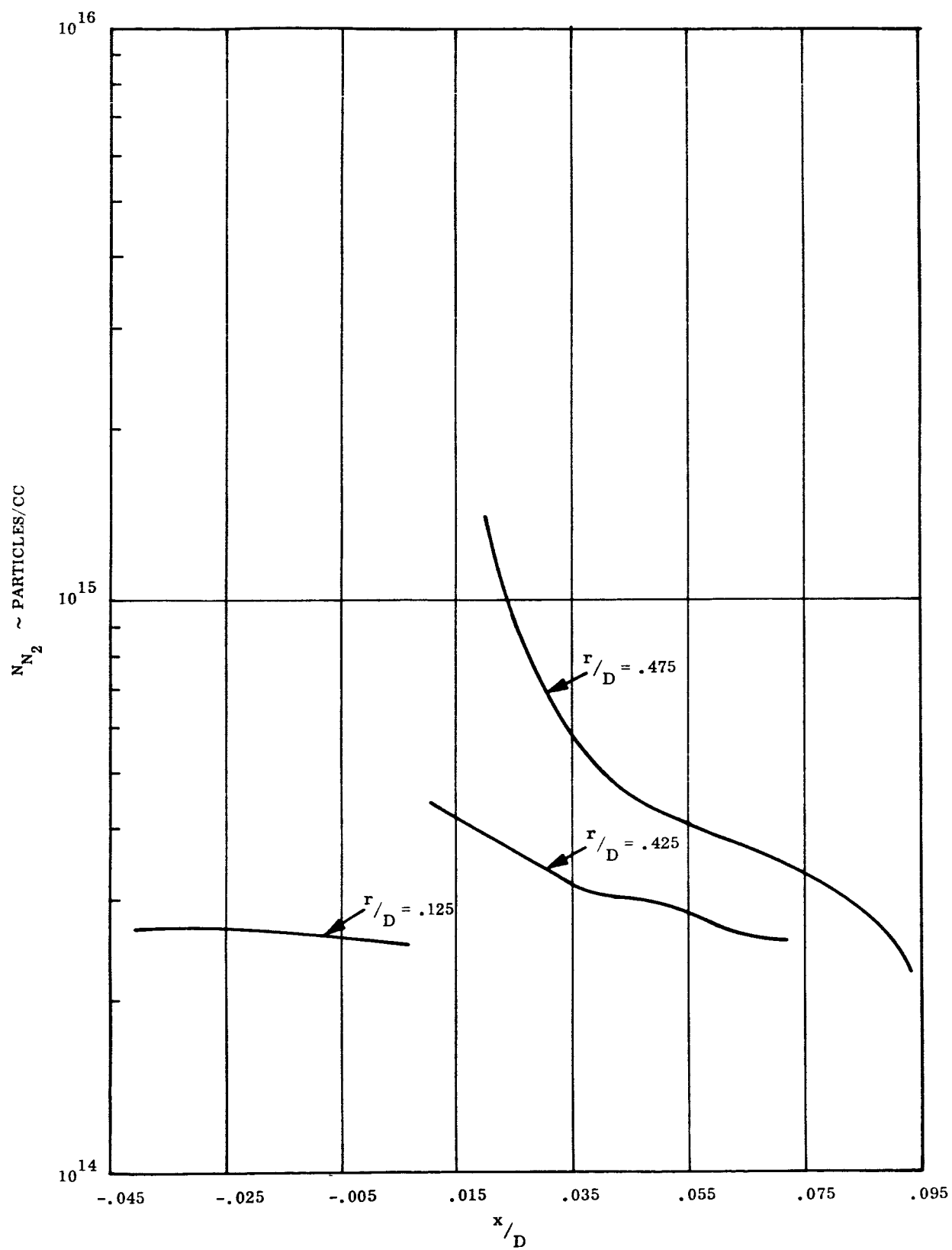


Figure 9. N_2 Concentration vs x/D on Lines of Constant r/D in Subsonic and Transonic Regions

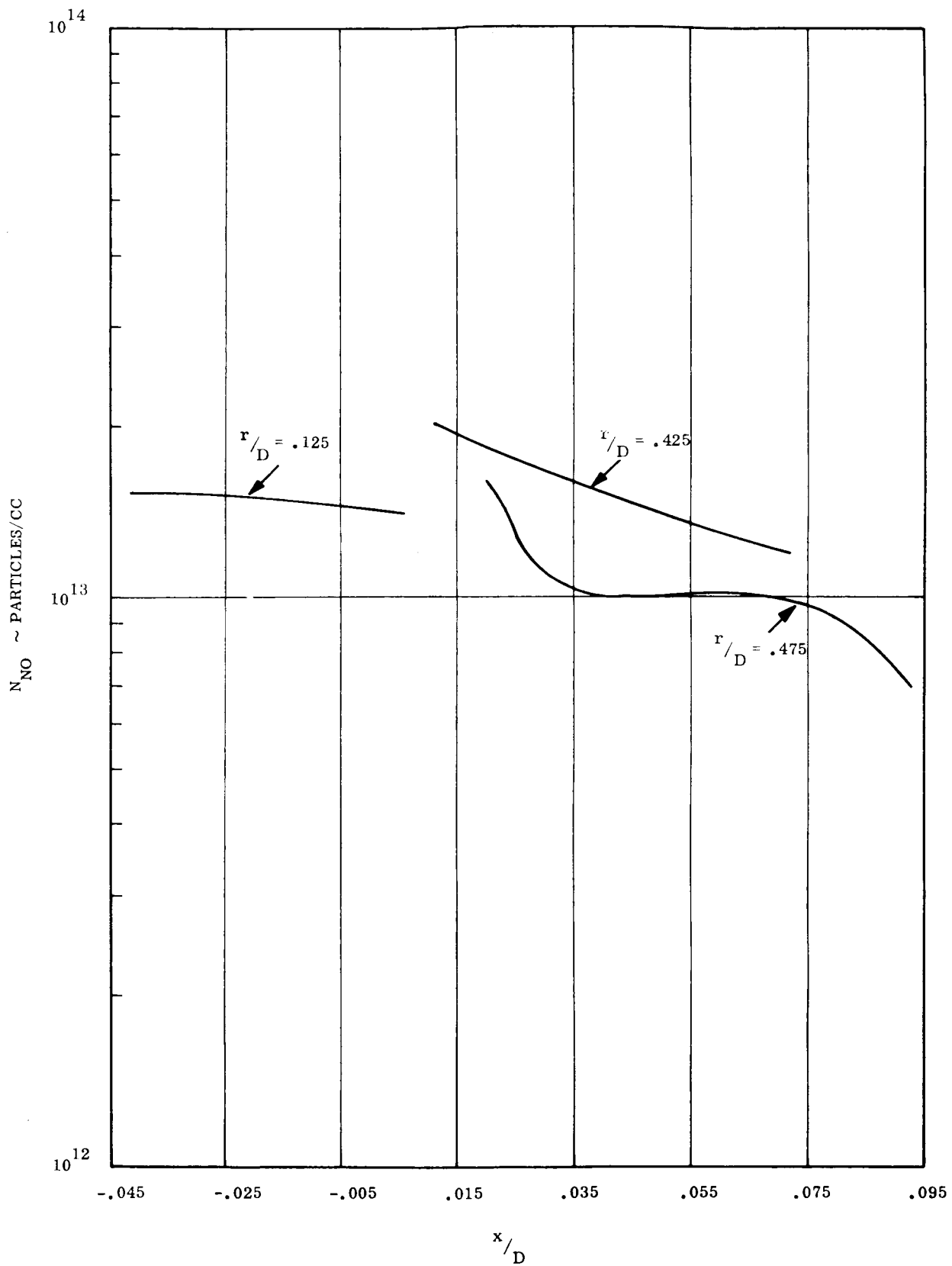


Figure 10. NO Concentration vs x/D on Lines of Constant r/D in Subsonic and Transonic Regions

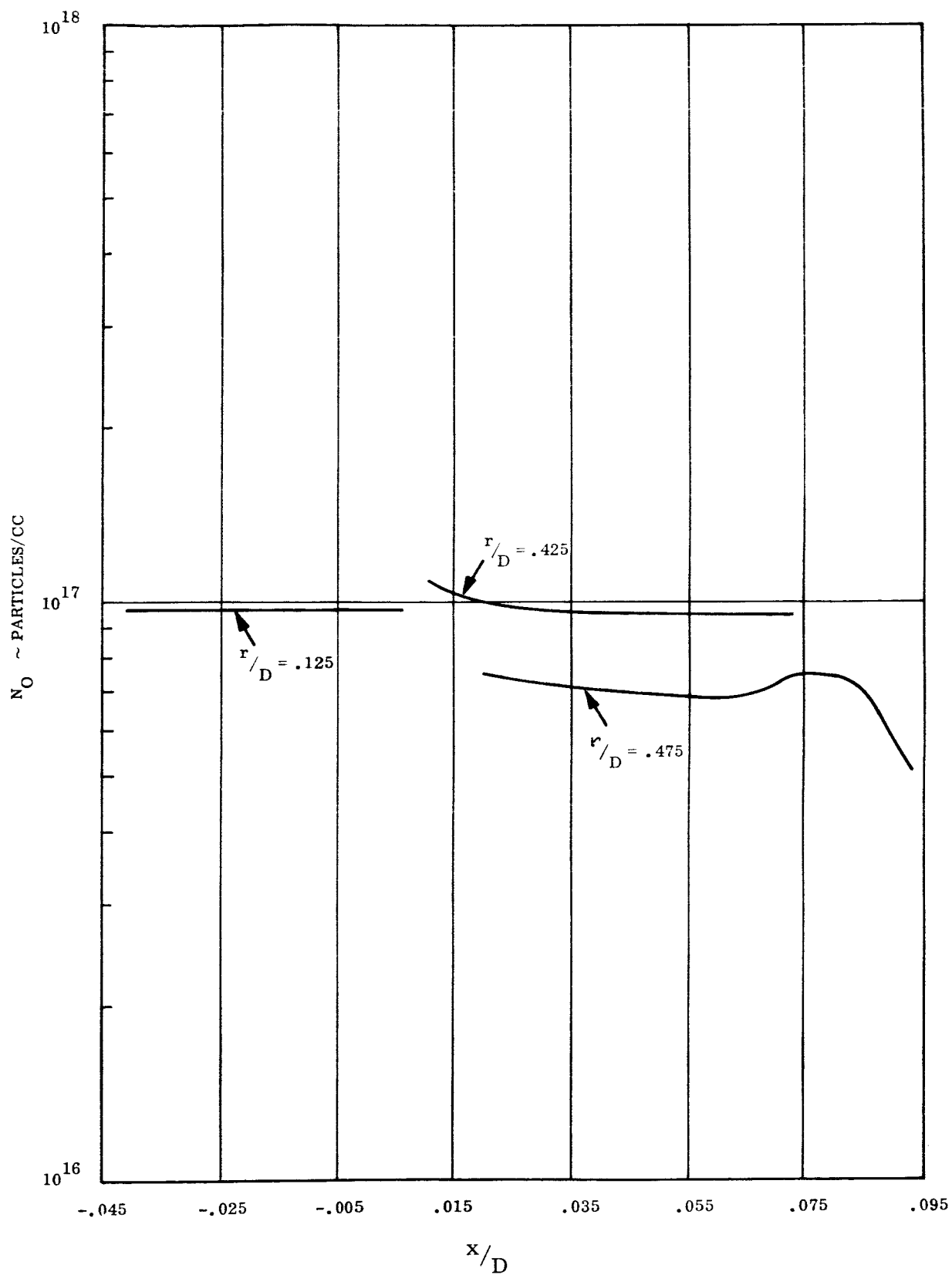


Figure 11. O Concentration vs x/D on Lines of Constant r/D in Subsonic and Transonic Regions

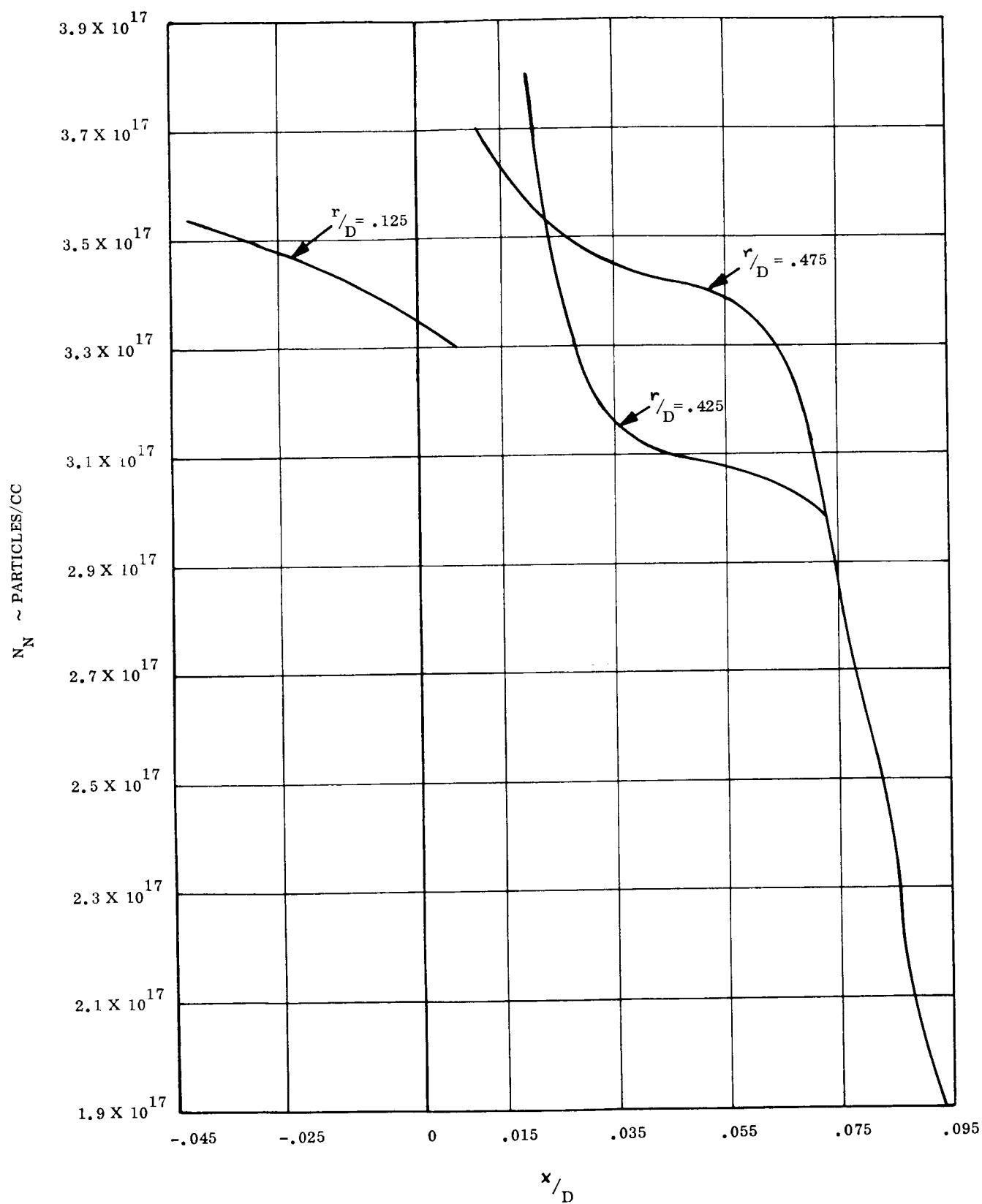


Figure 12. N Concentration vs x/D on Lines of Constant r/D in Subsonic and Transonic Regions

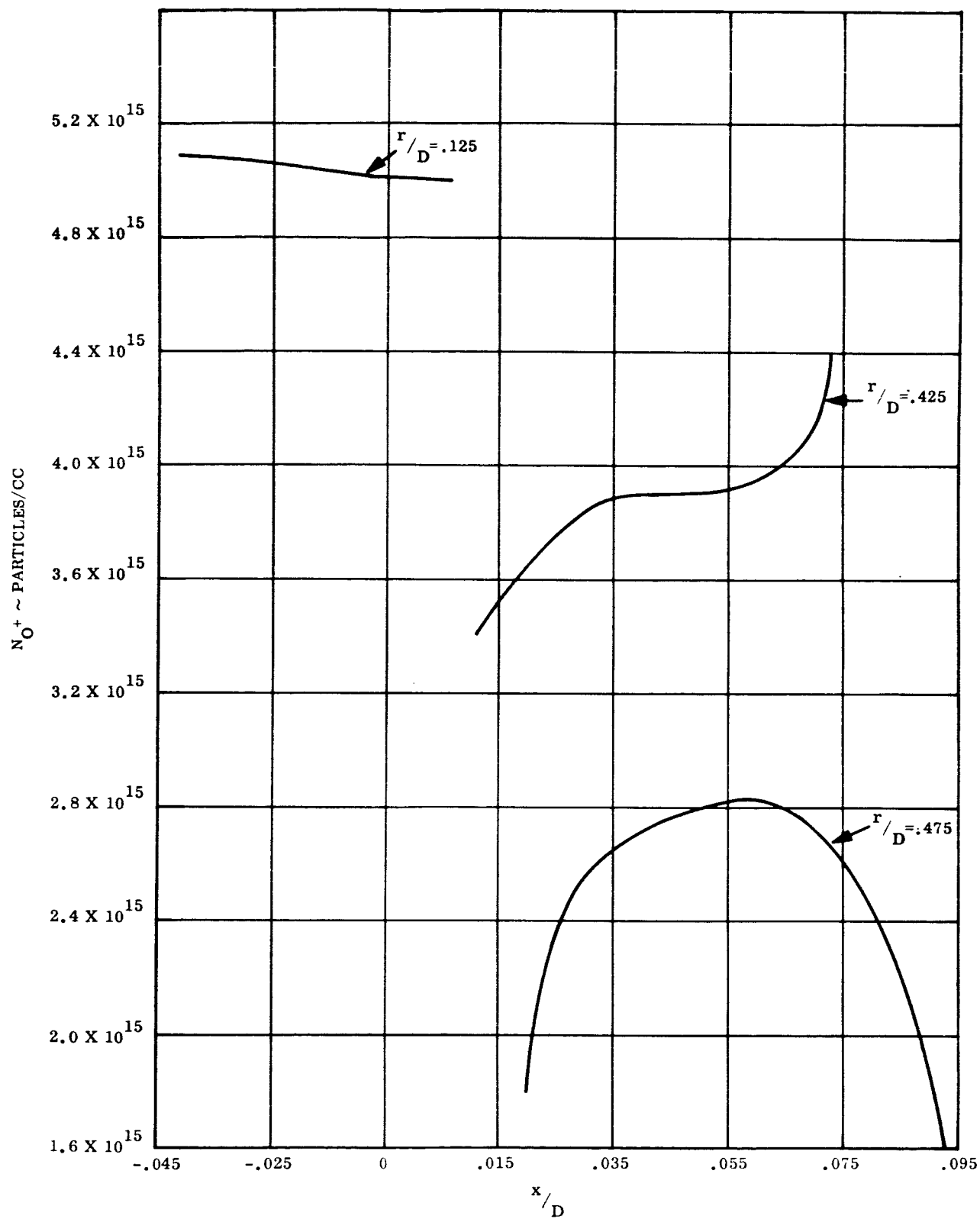


Figure 13. O^+ Concentration vs x/D on Lines of Constant r/D in Subsonic and Transonic Regions

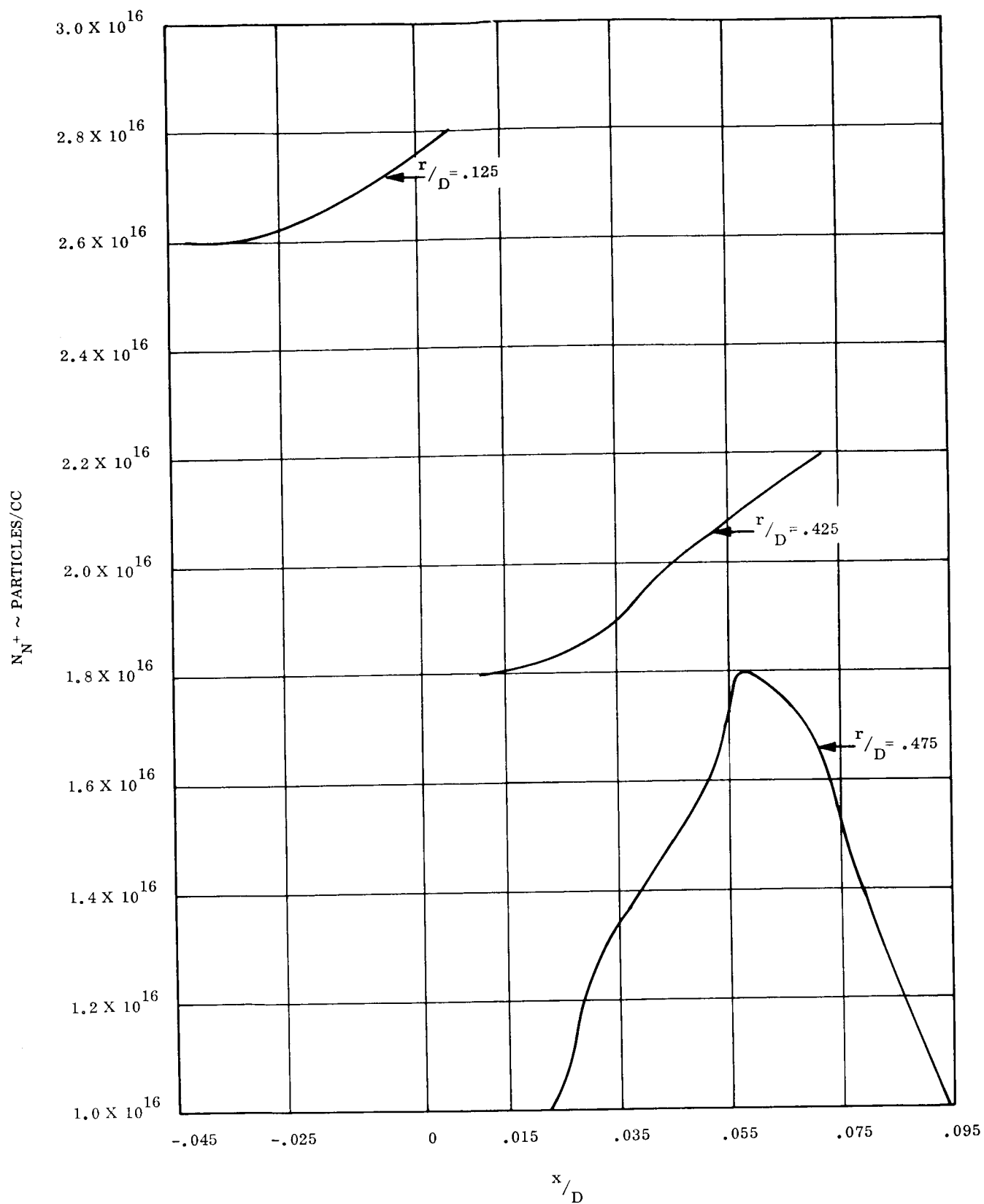


Figure 14. N^+ Concentration vs x/D on Lines of Constant r/D in Subsonic and Transonic Regions

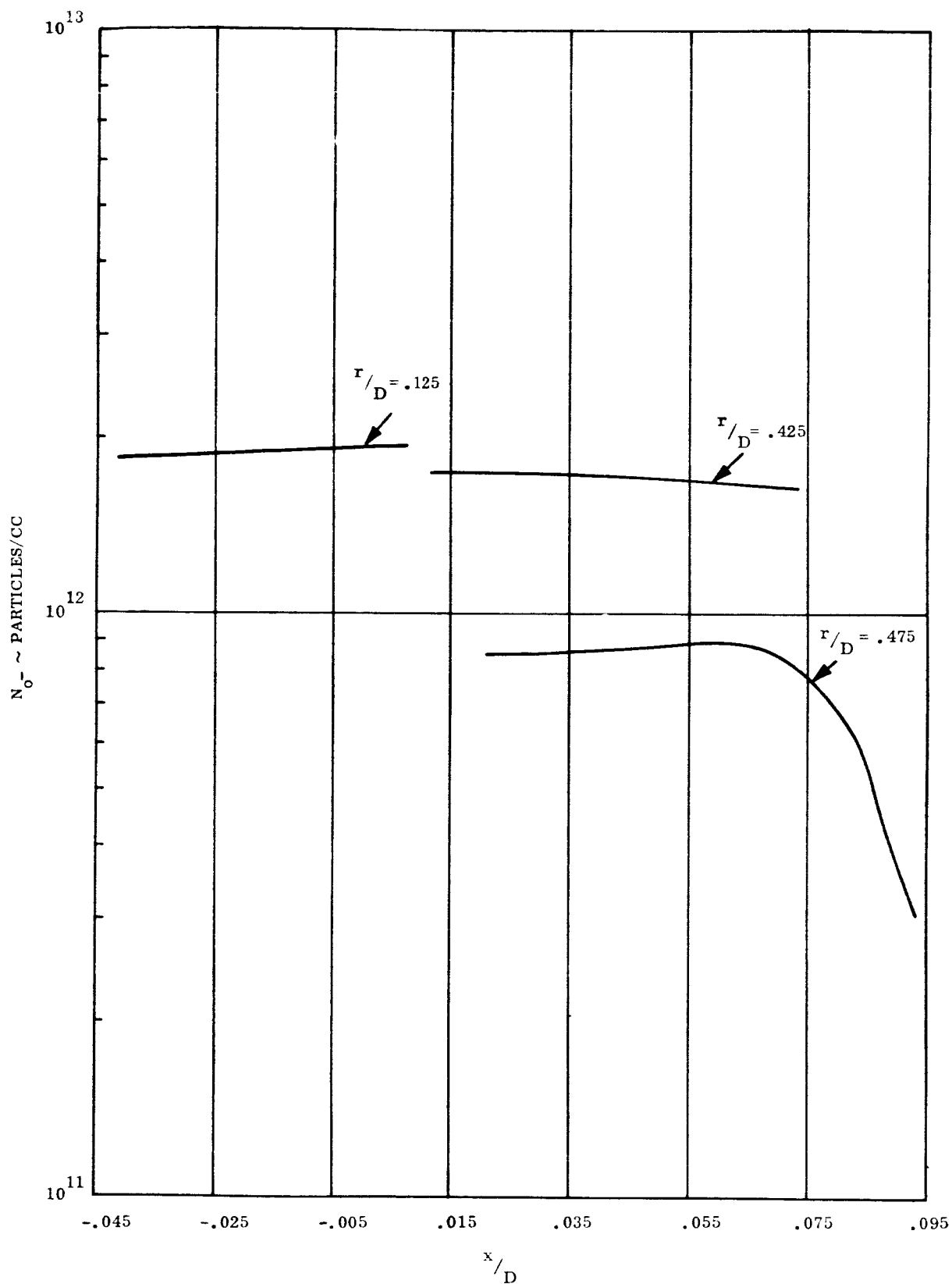


Figure 15. O^- Concentration vs x/D on Lines of Constant r/D in Subsonic and Transonic Regions

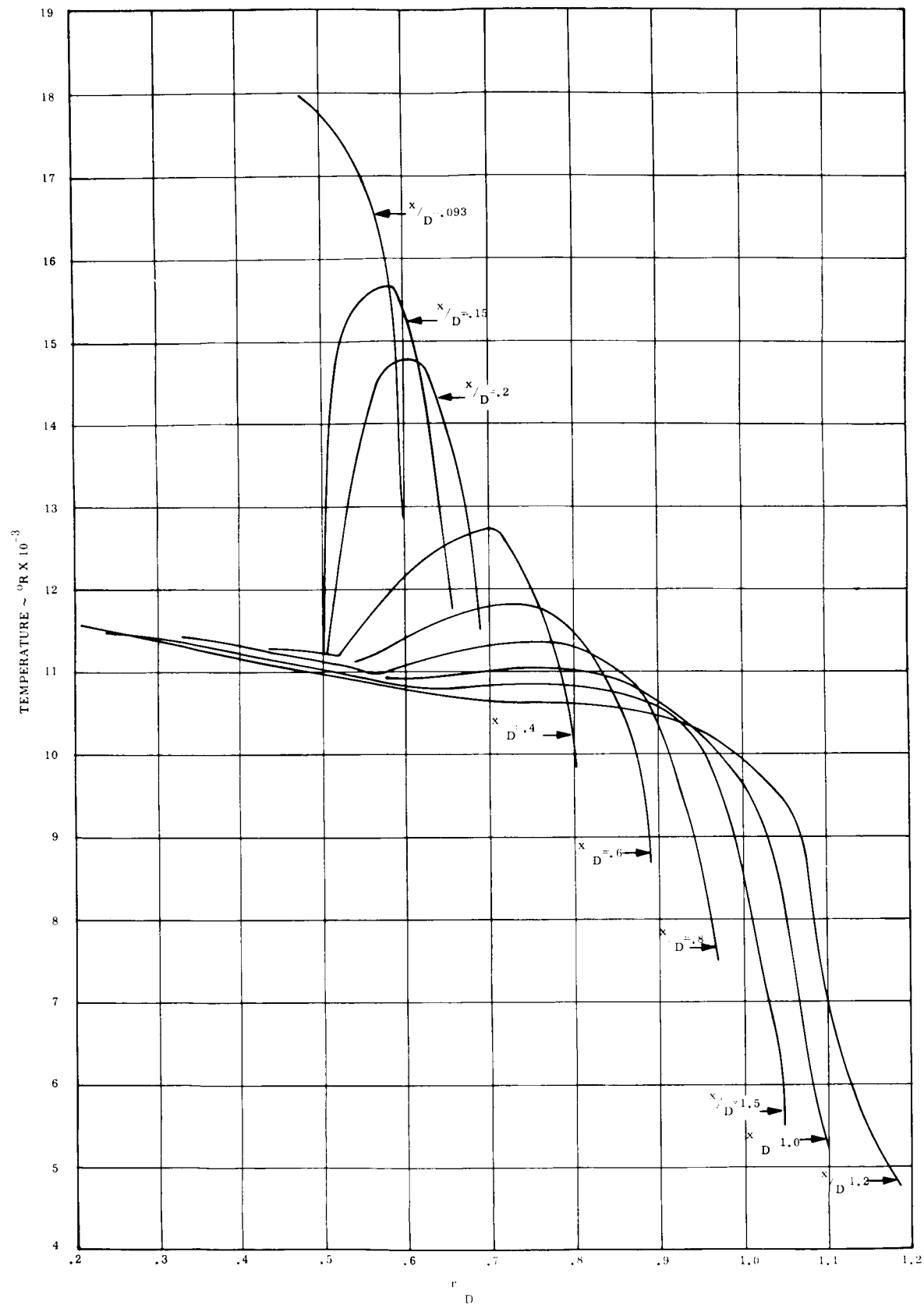


Figure 16. Temperature vs r/D on Lines of Constant x/D in Supersonic Region of Flow Field

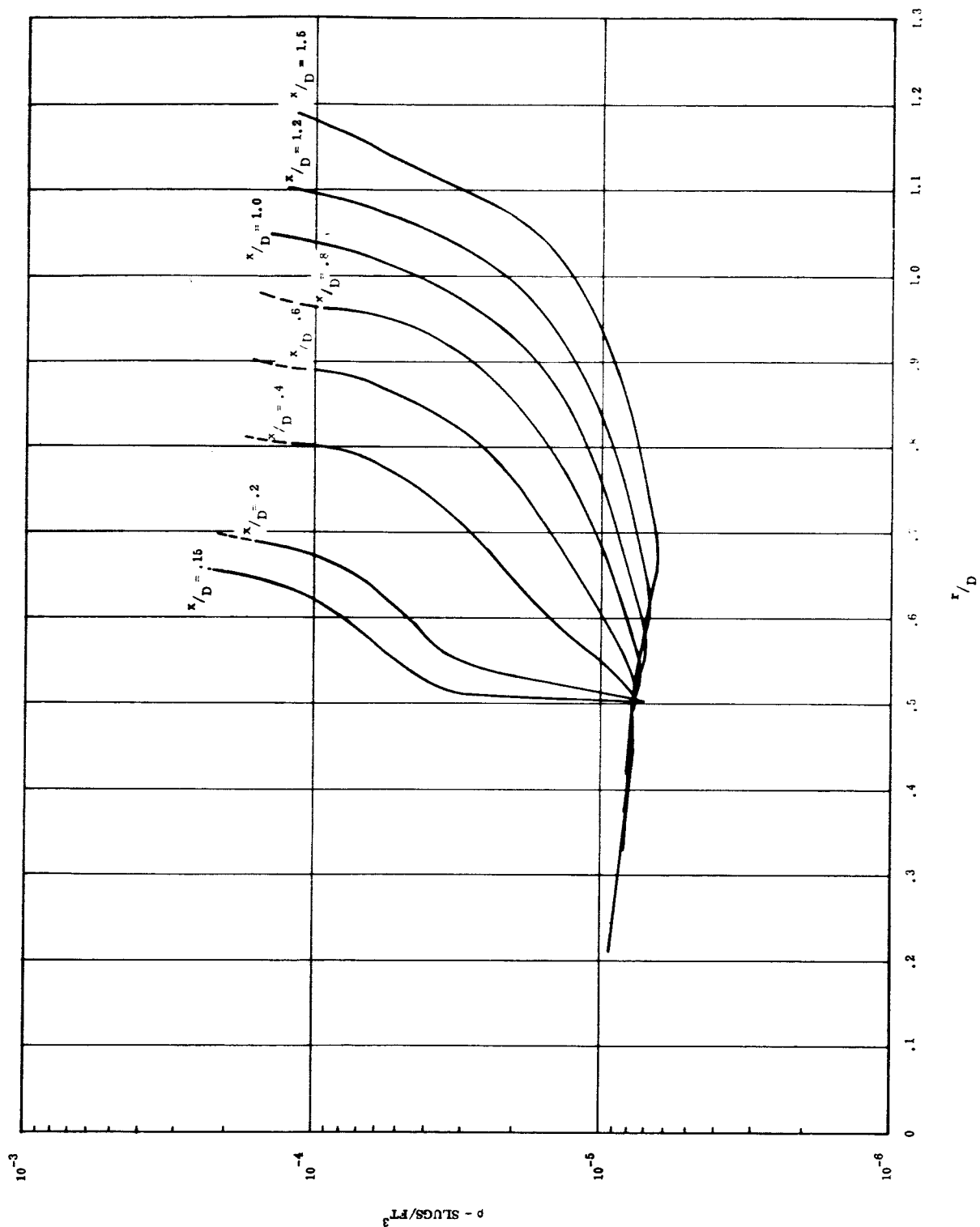


Figure 17. Density vs r/D on Lines of Constant x/D in Supersonic Region of Flow Field

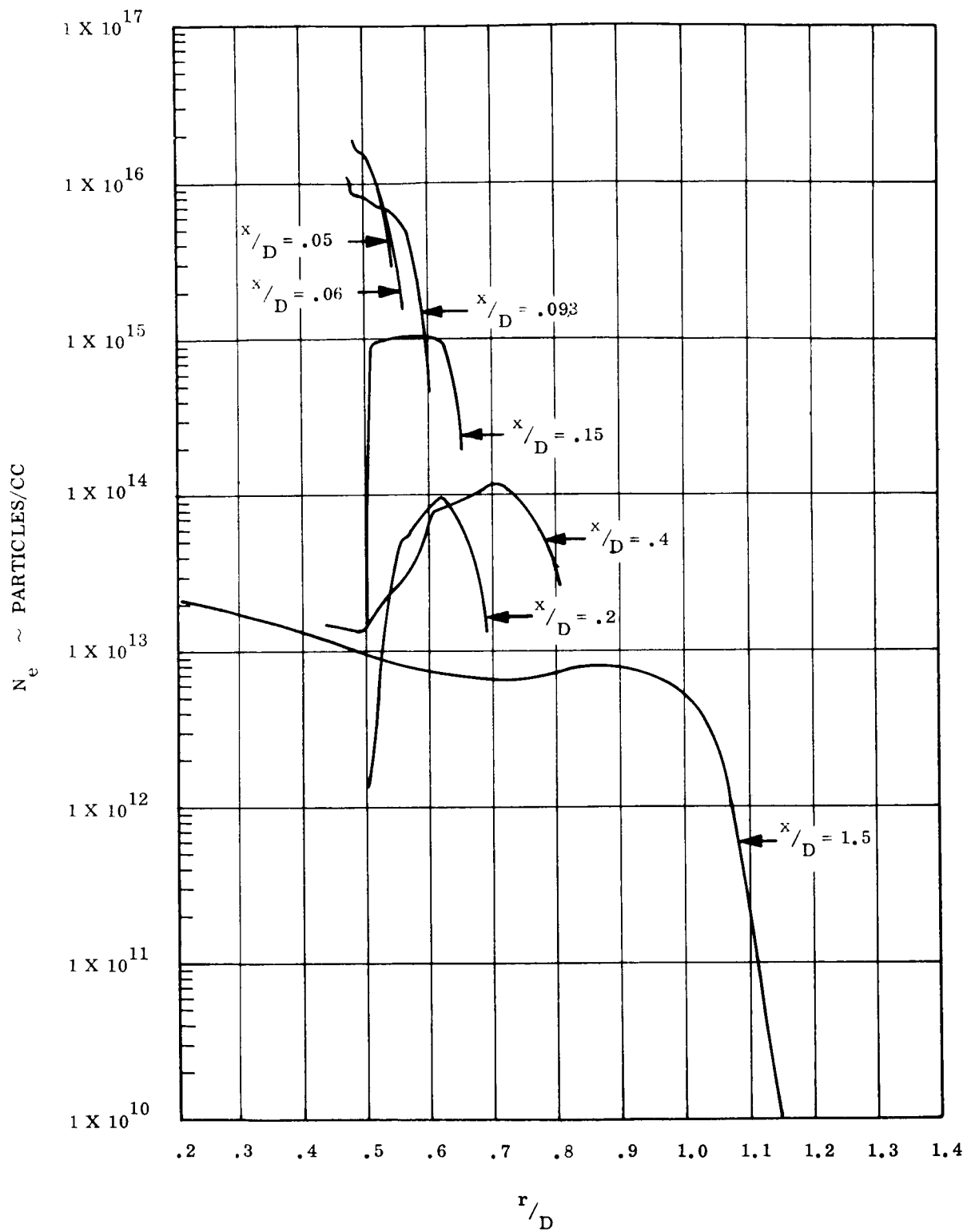


Figure 18. Electron Density r/D on Lines of Constant x/D in Supersonic Region of Flow Field

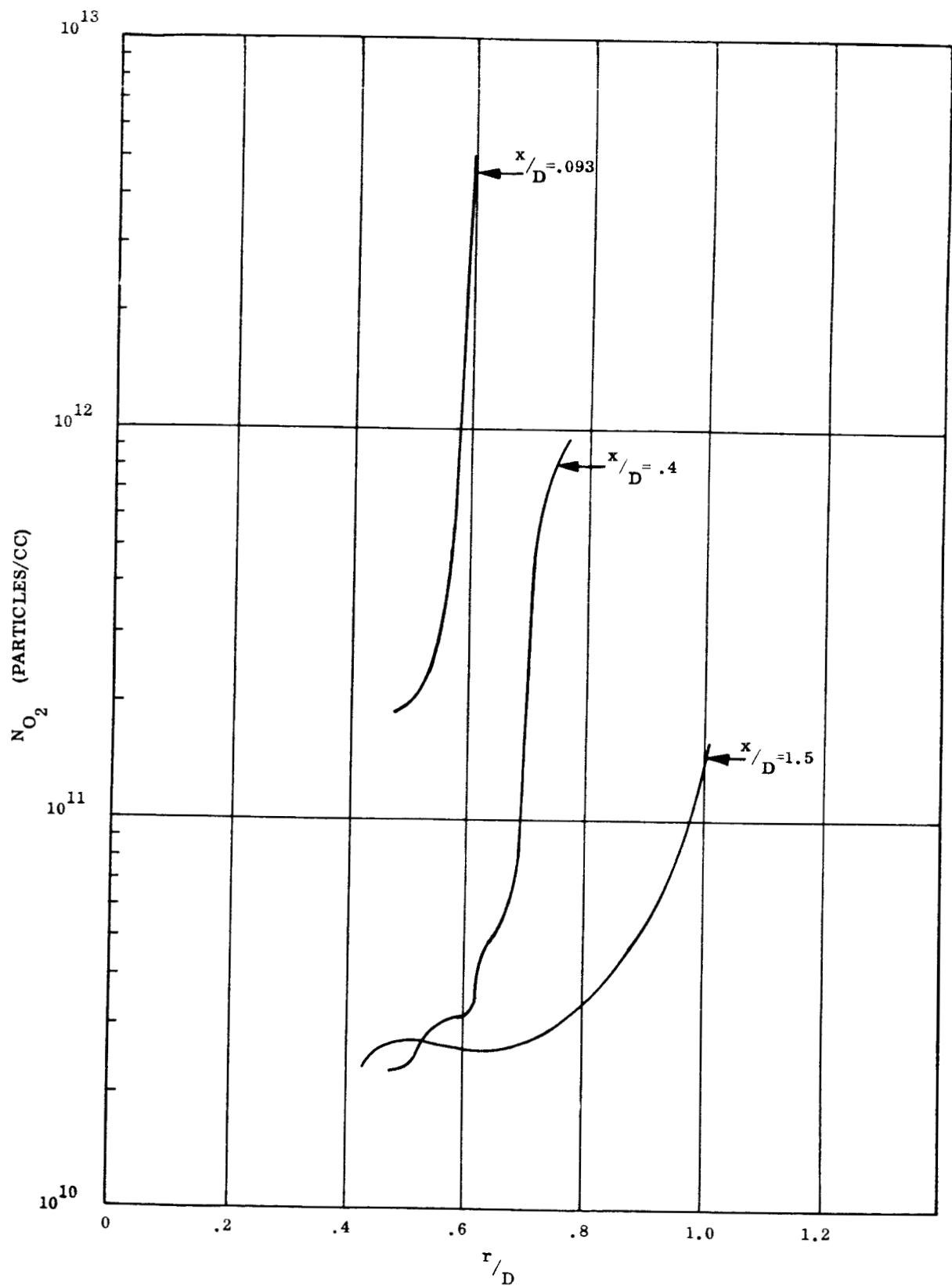


Figure 19. O_2 Concentration vs r/D on Lines of Constant x/D in Supersonic Region of Flow Field

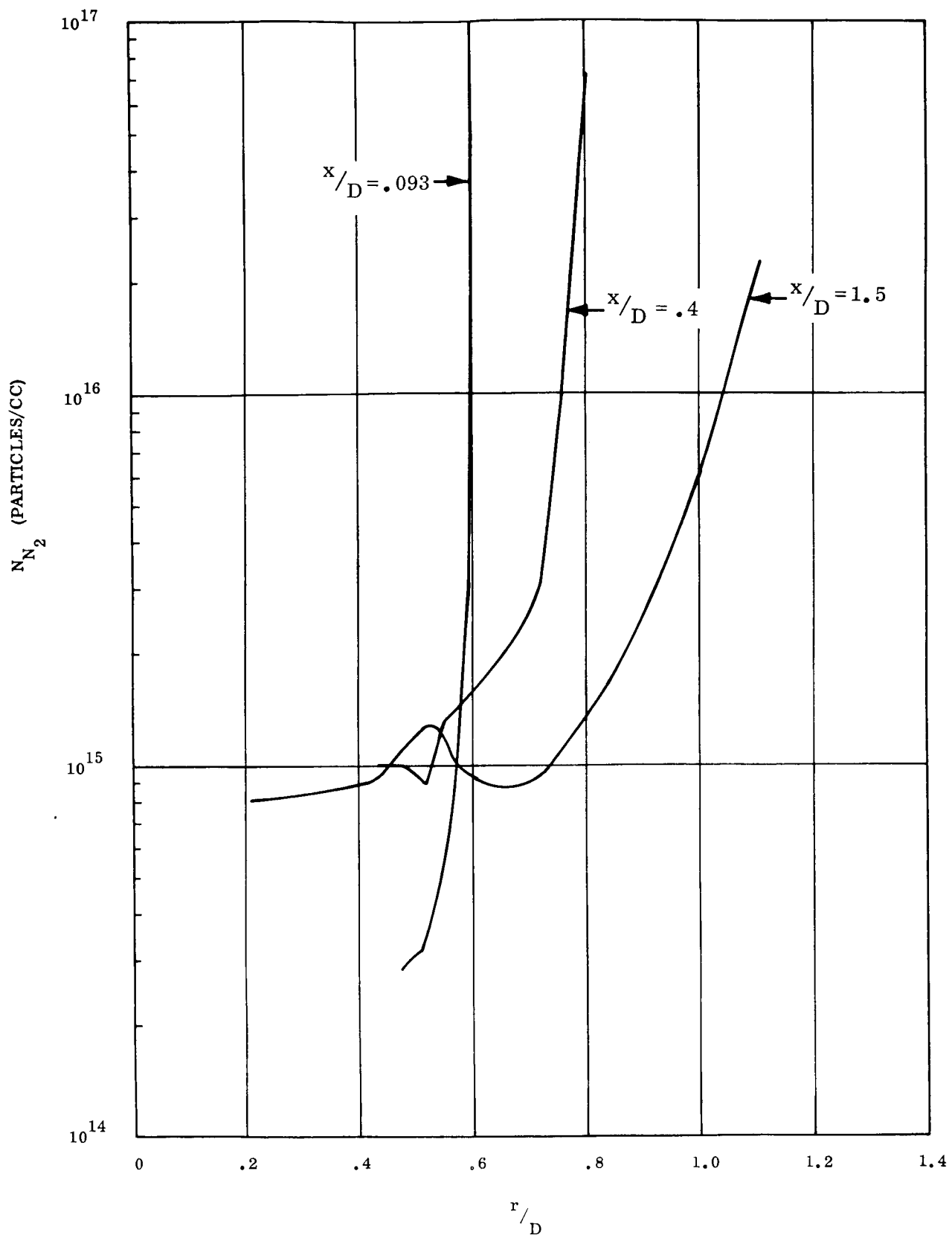


Figure 20. N_2 Concentration vs r/D on Lines of Constant x/D in Supersonic Region of Flow Field

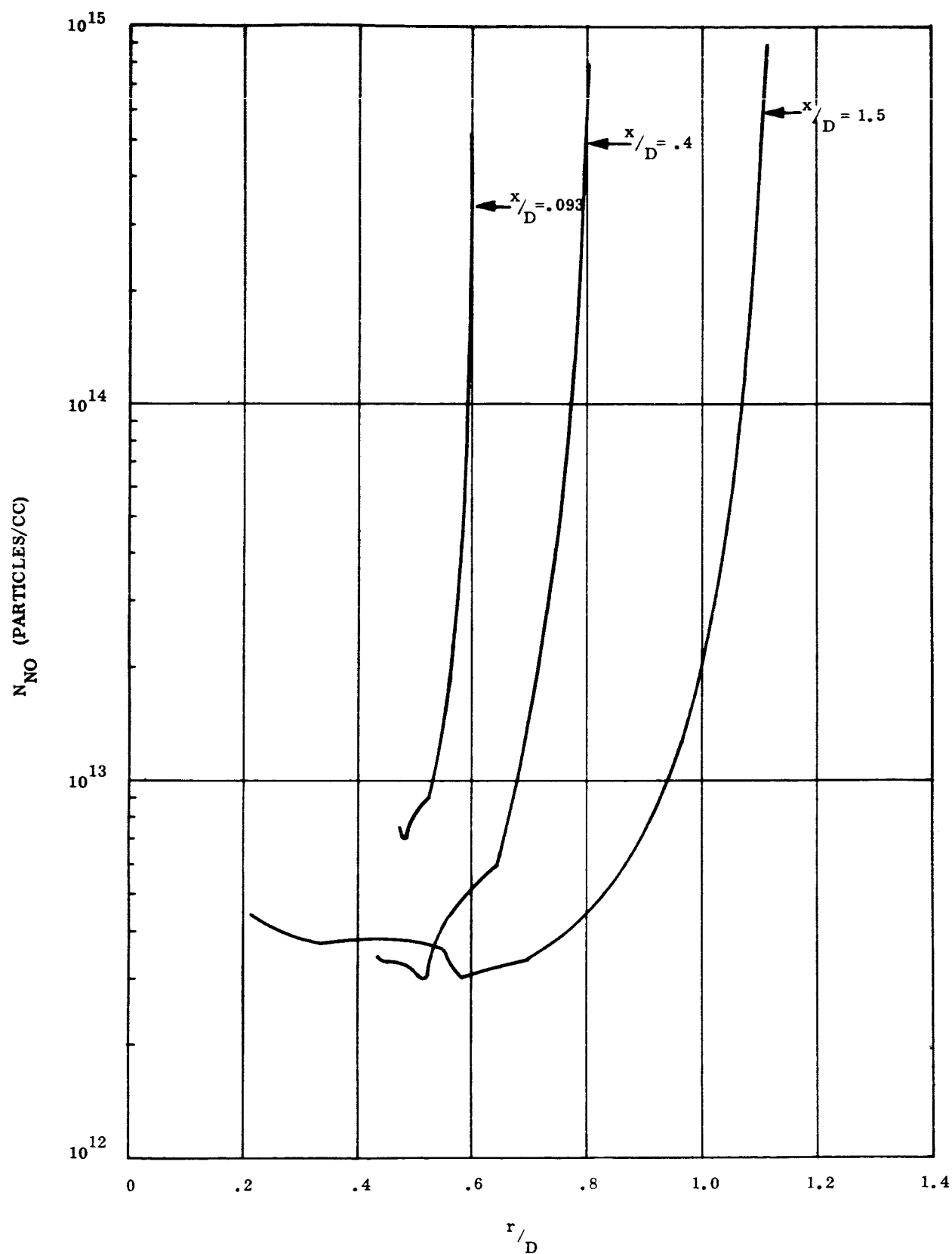


Figure 21. NO Concentration vs r/D on Lines of Constant x/D in Supersonic Region of Flow Field

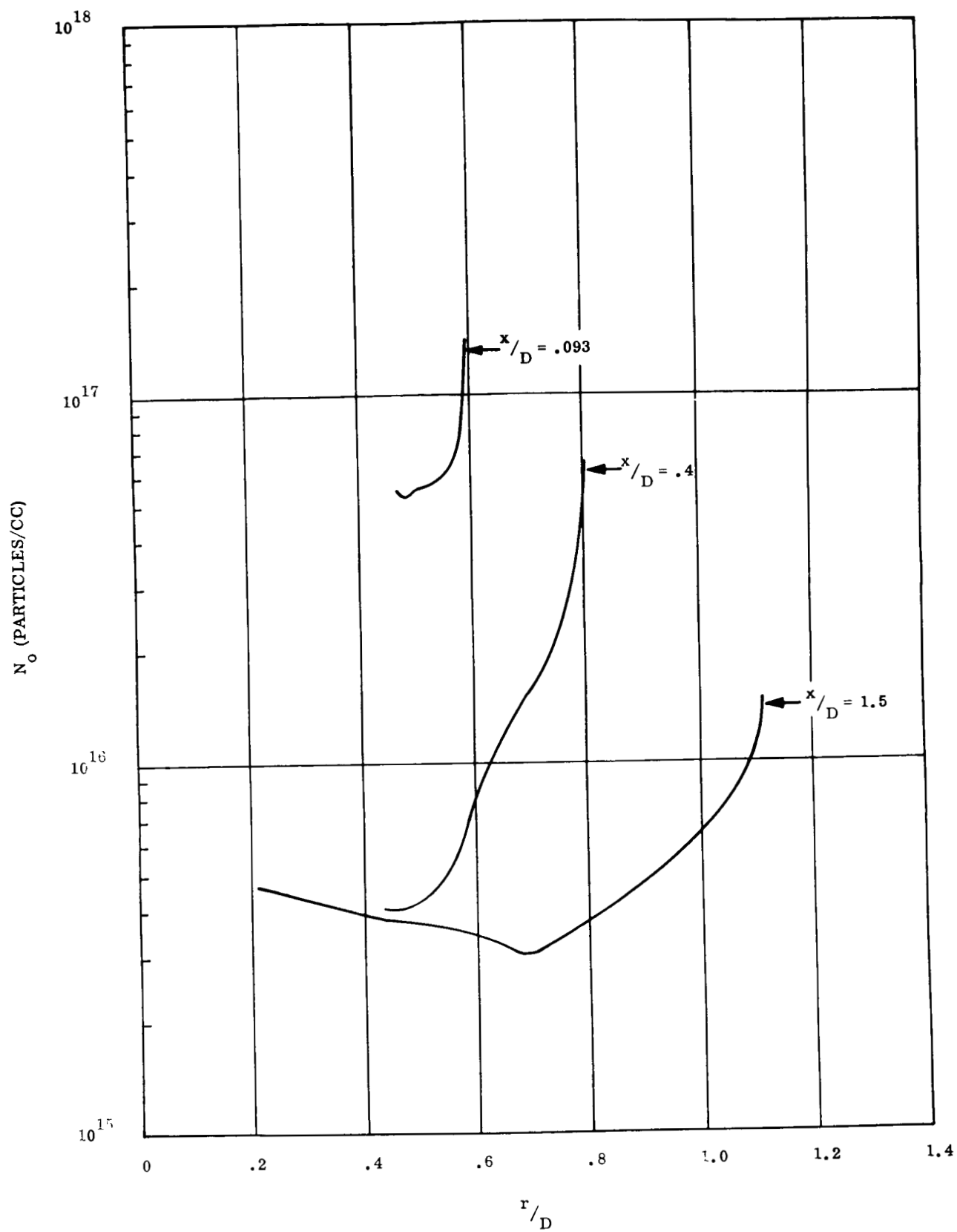


Figure 22. O Concentration vs r/D on Lines of Constant x/D in Supersonic Region of Flow Field

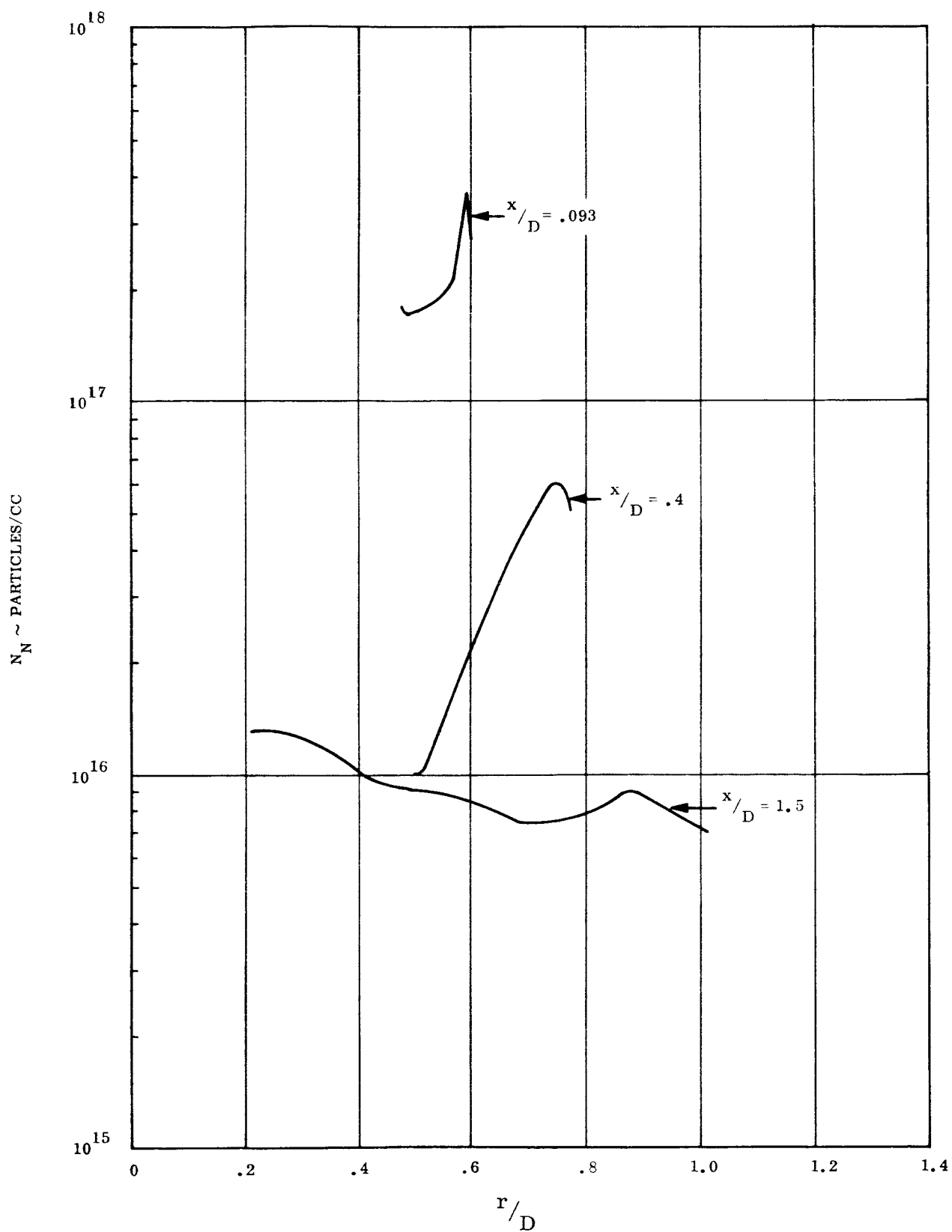


Figure 23. N Concentration vs r/D on Lines of Constant x/D in Supersonic Region of Flow Field

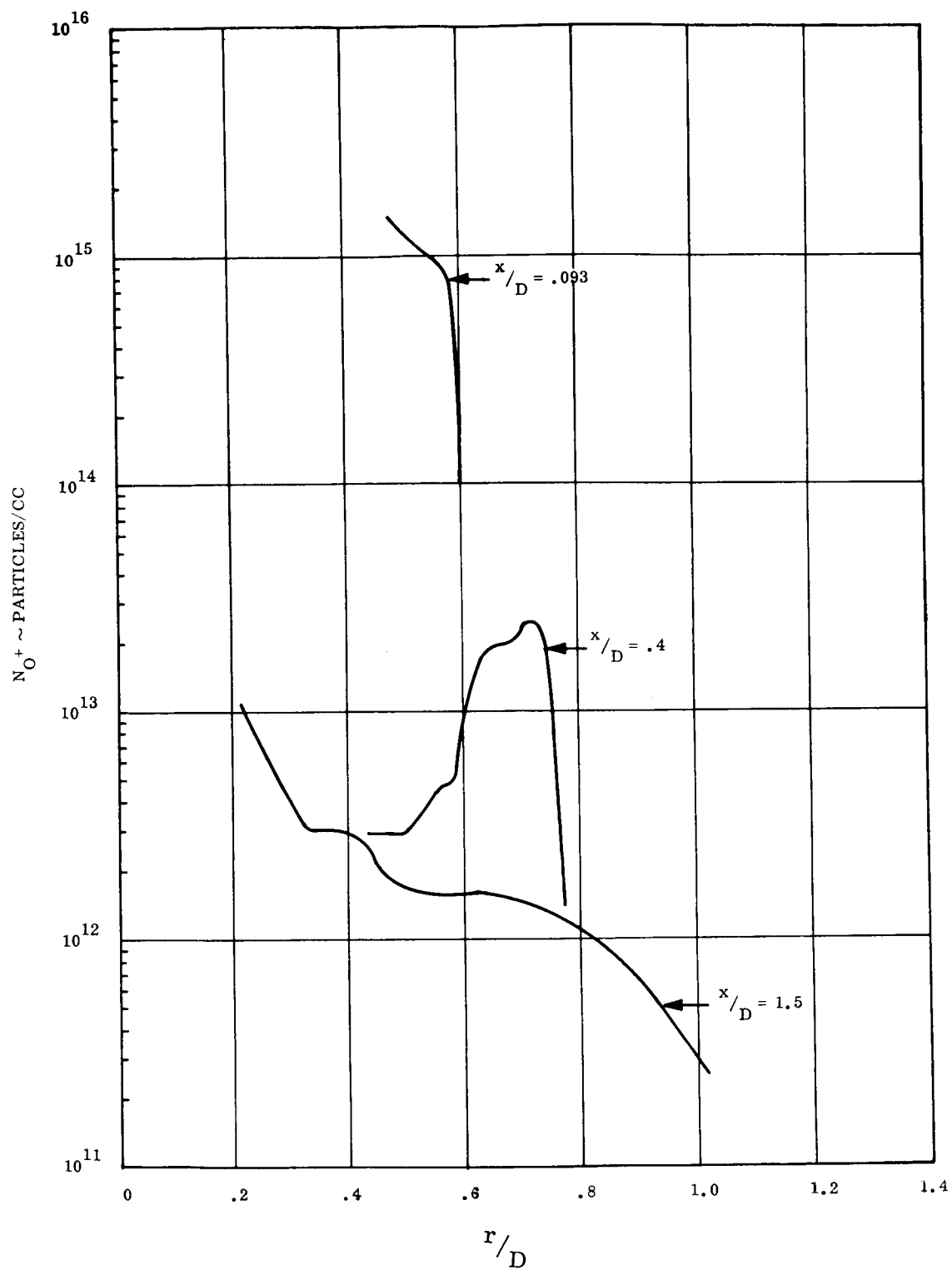


Figure 24. O^+ Concentration vs r/D on Lines of Constant x/D in Supersonic Region of Flow Field

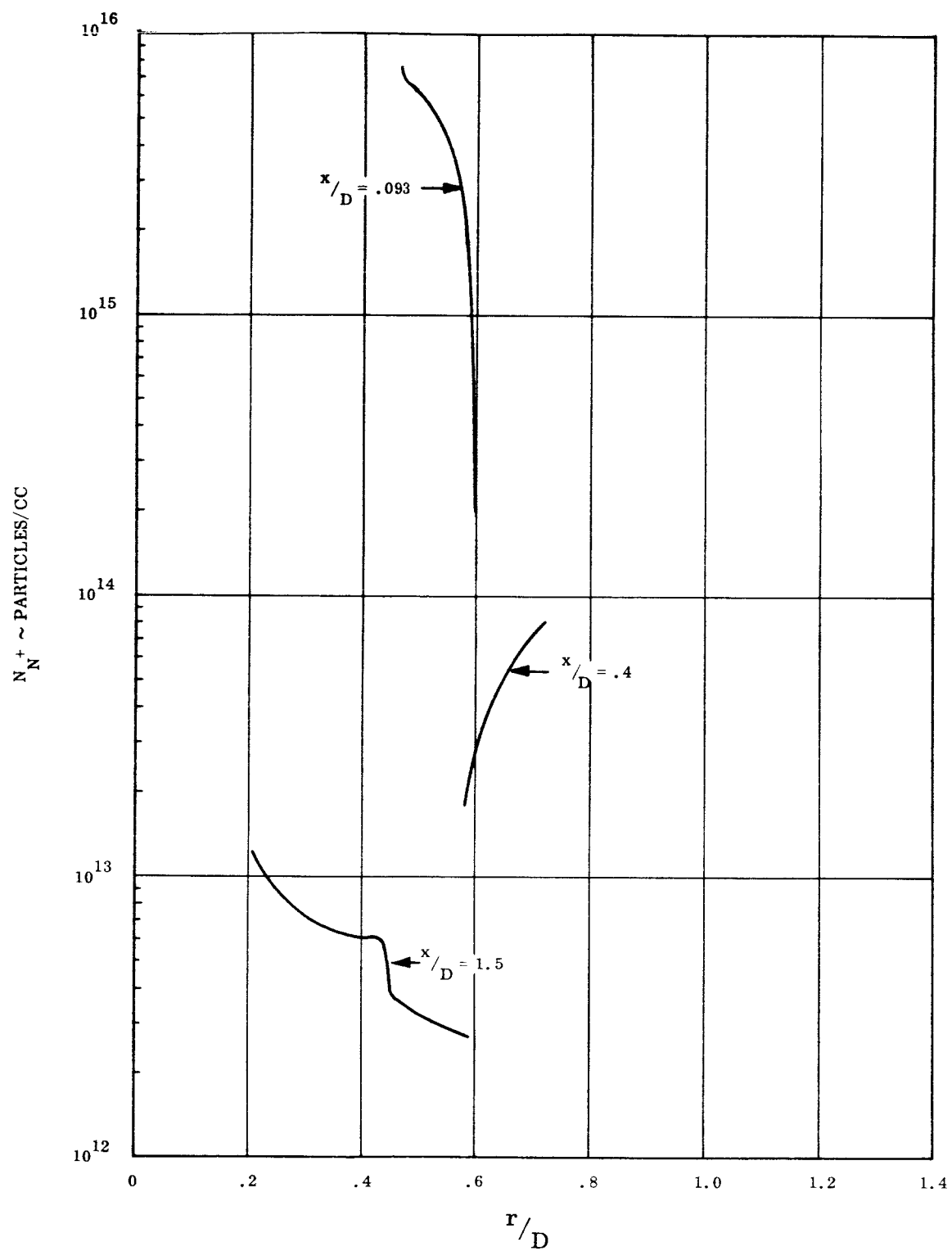


Figure 25. N^+ Concentration vs r/D on Lines of Constant x/D in Supersonic Region of Flow Field

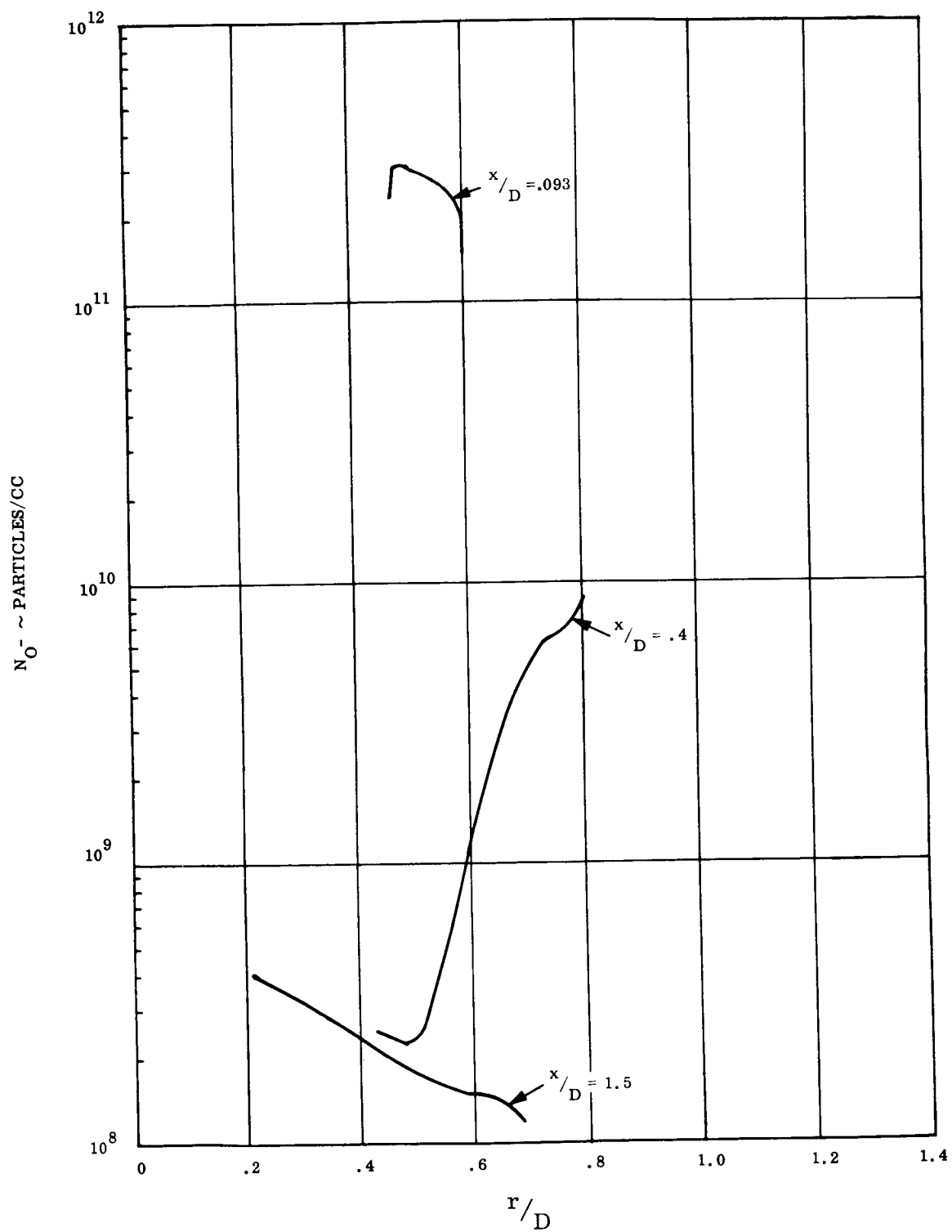


Figure 26. O^- Concentration vs r/D on Lines of Constant x/D in Supersonic Region of Flow Field

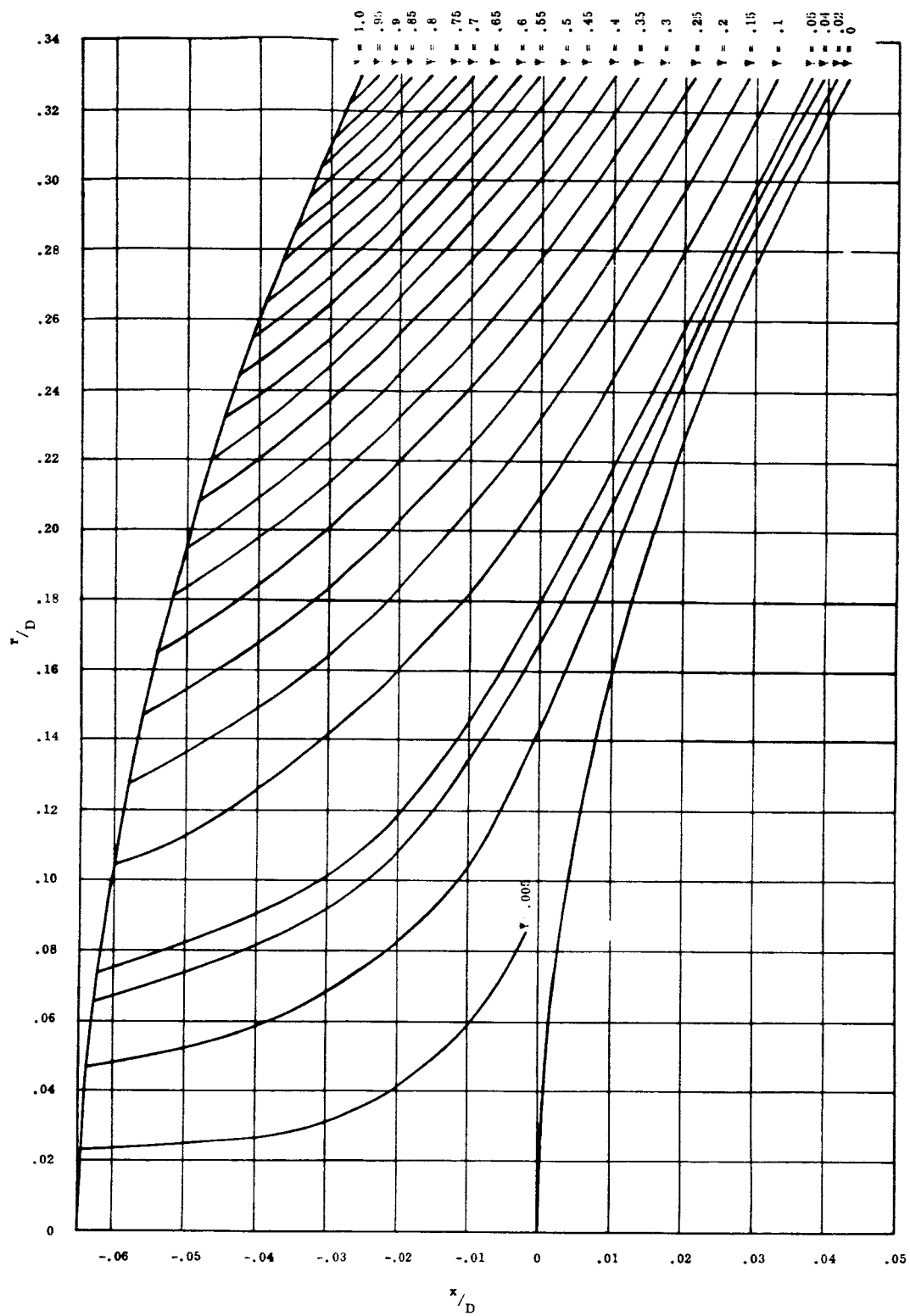


Figure 27. Streamlines in the Subsonic Region of the Flow Field

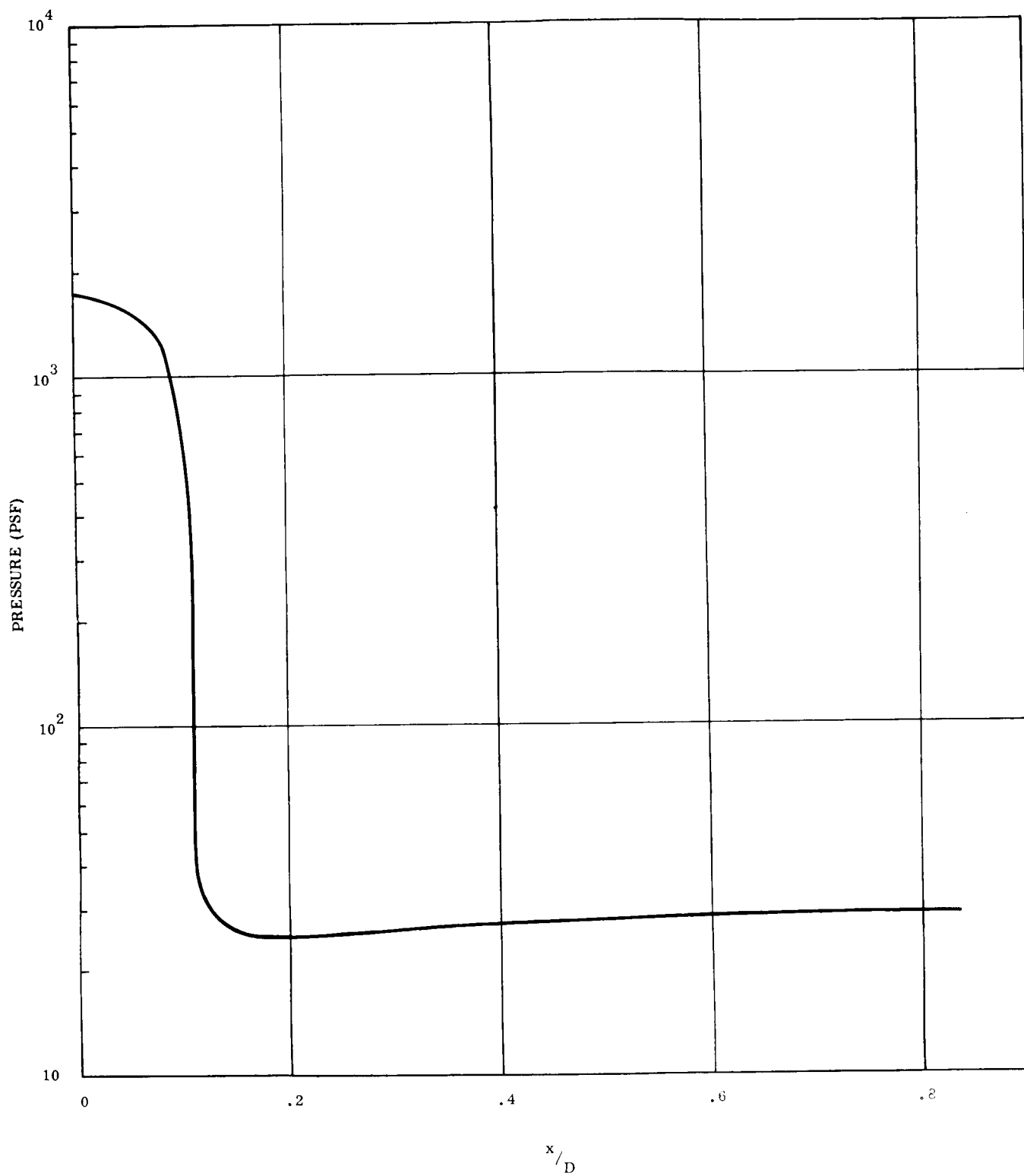


Figure 28. Pressure at the Body Surface

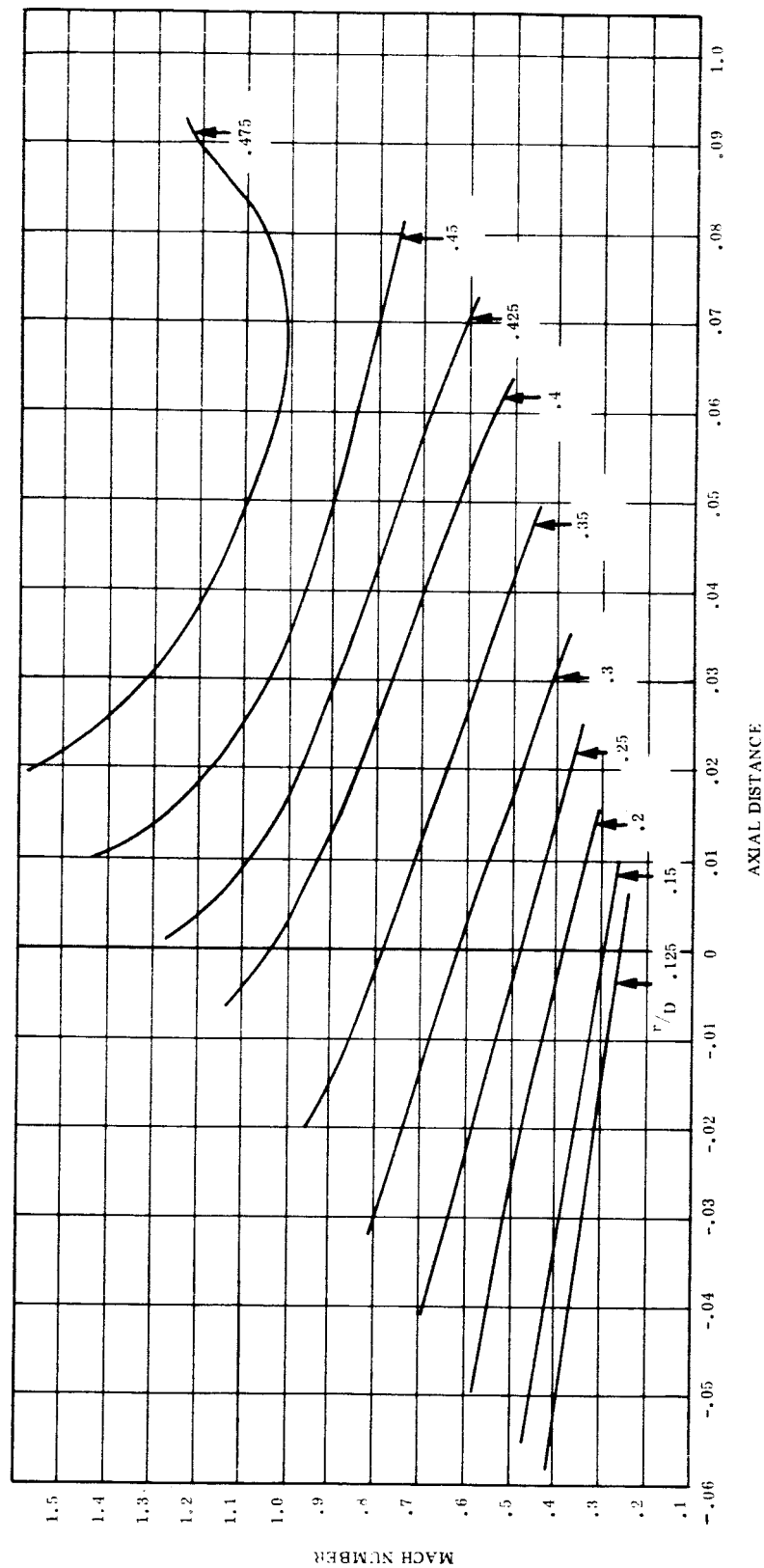


Figure 29. Mach Number vs x/D on Lines of Constant r/D in Subsonic and Transonic Region of Flow Field

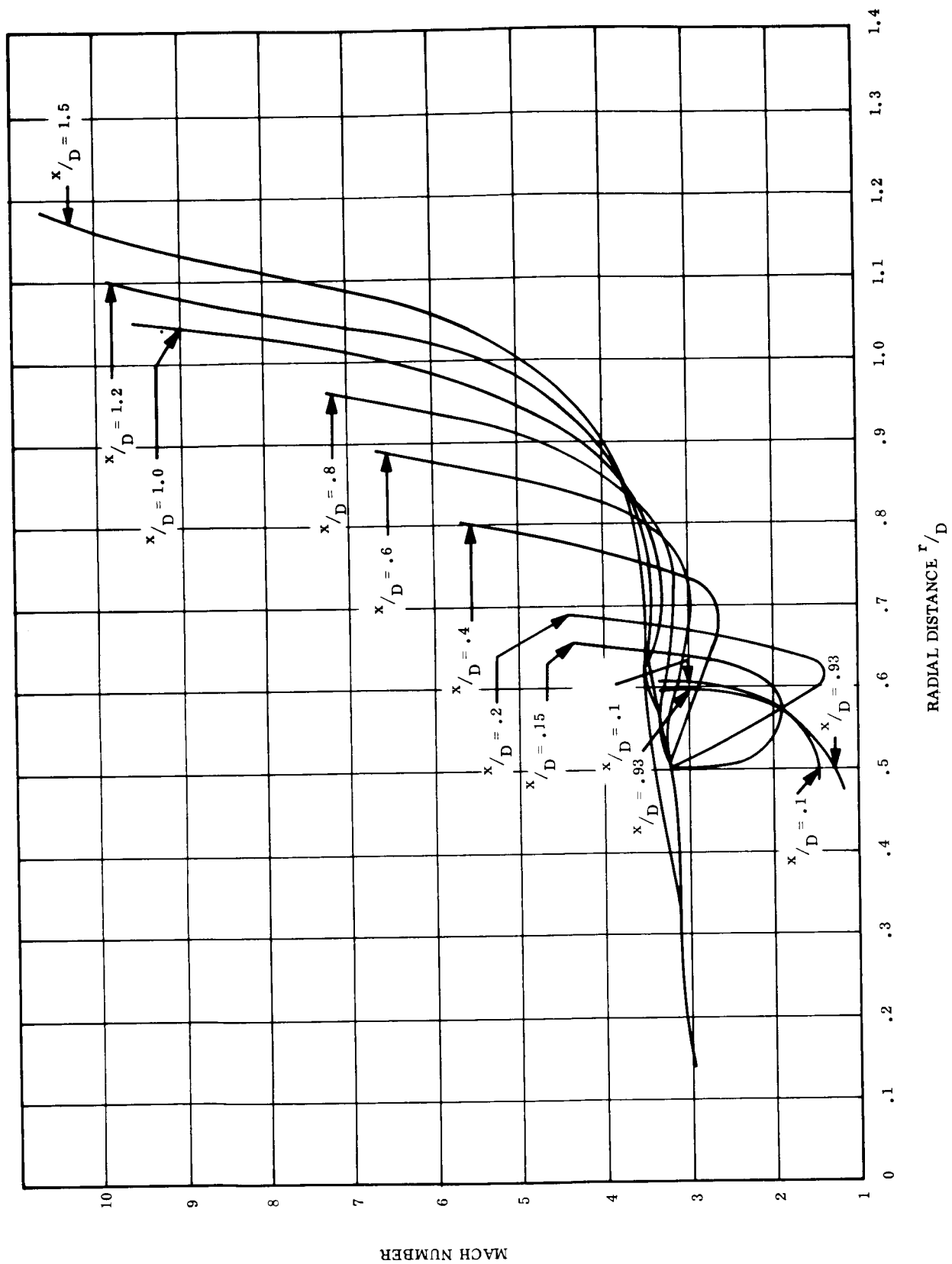


Figure 30. Mach Number vs. r/D on Lines of Constant x/D in Supersonic Region of Flow Field

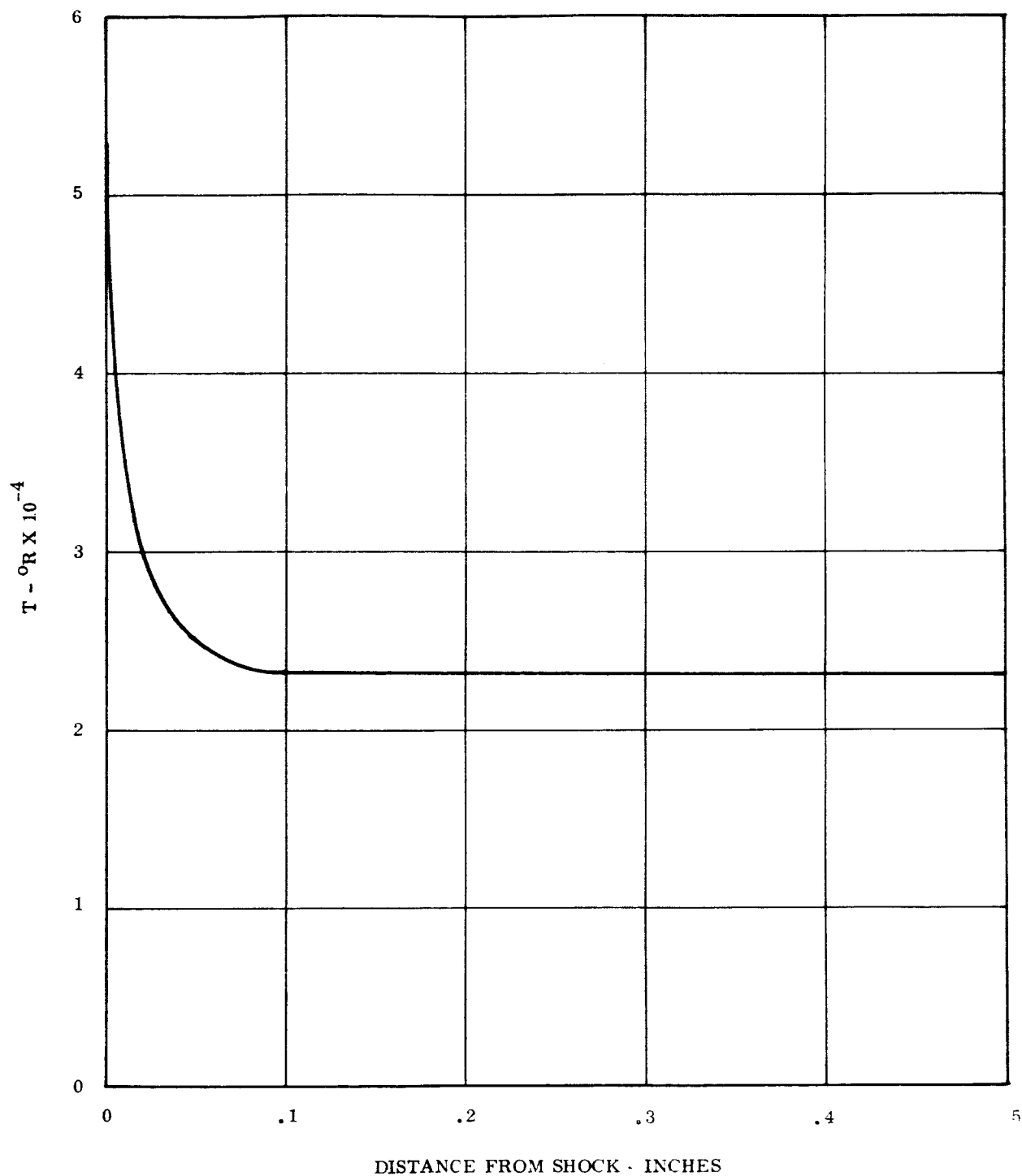


Figure 31. Temperature vs Distance Downstream of a Normal Shock
for Non-equilibrium Flow

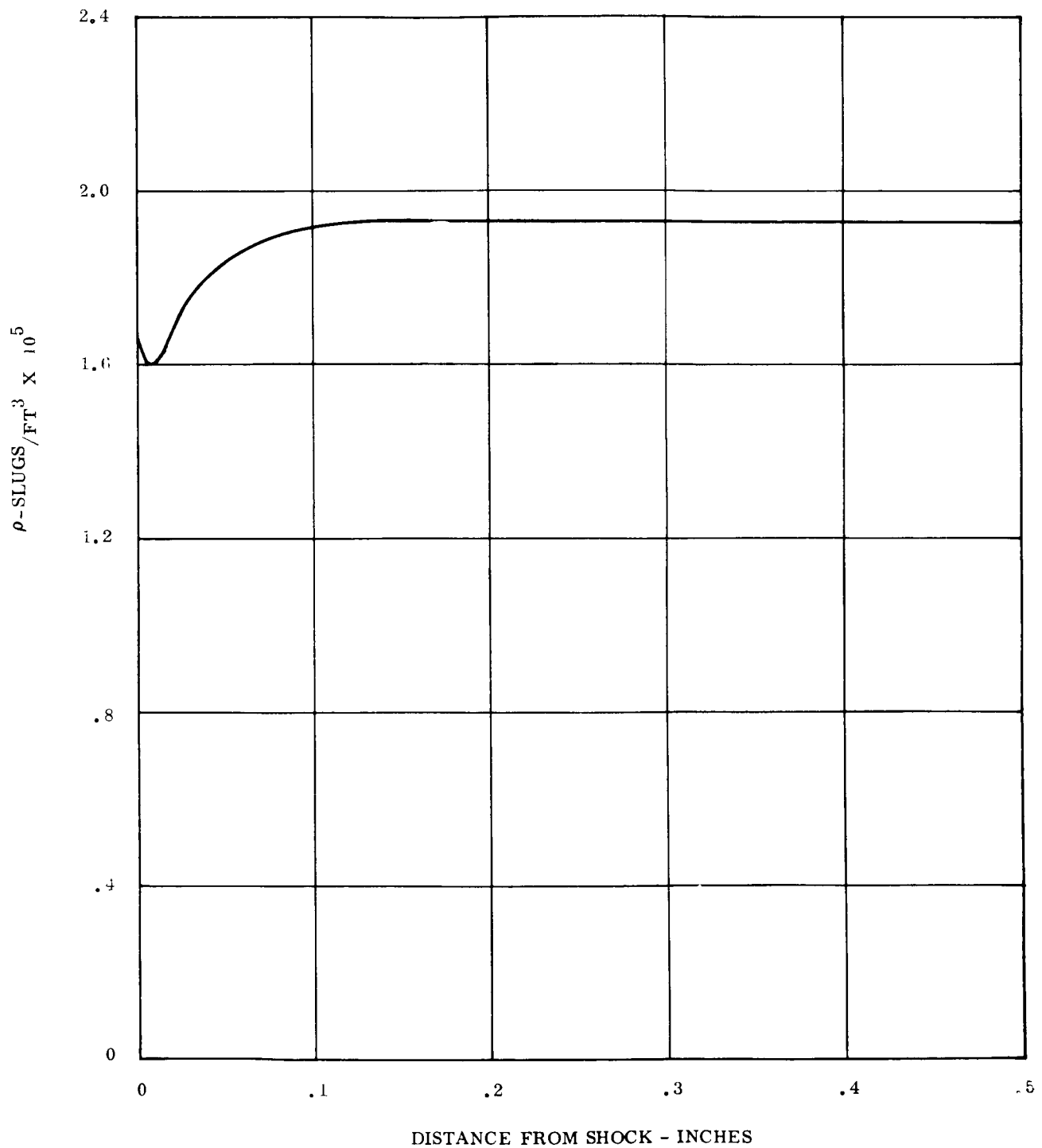


Figure 32. Density vs Distance Downstream of a Normal Shock
For Non-equilibrium Flow

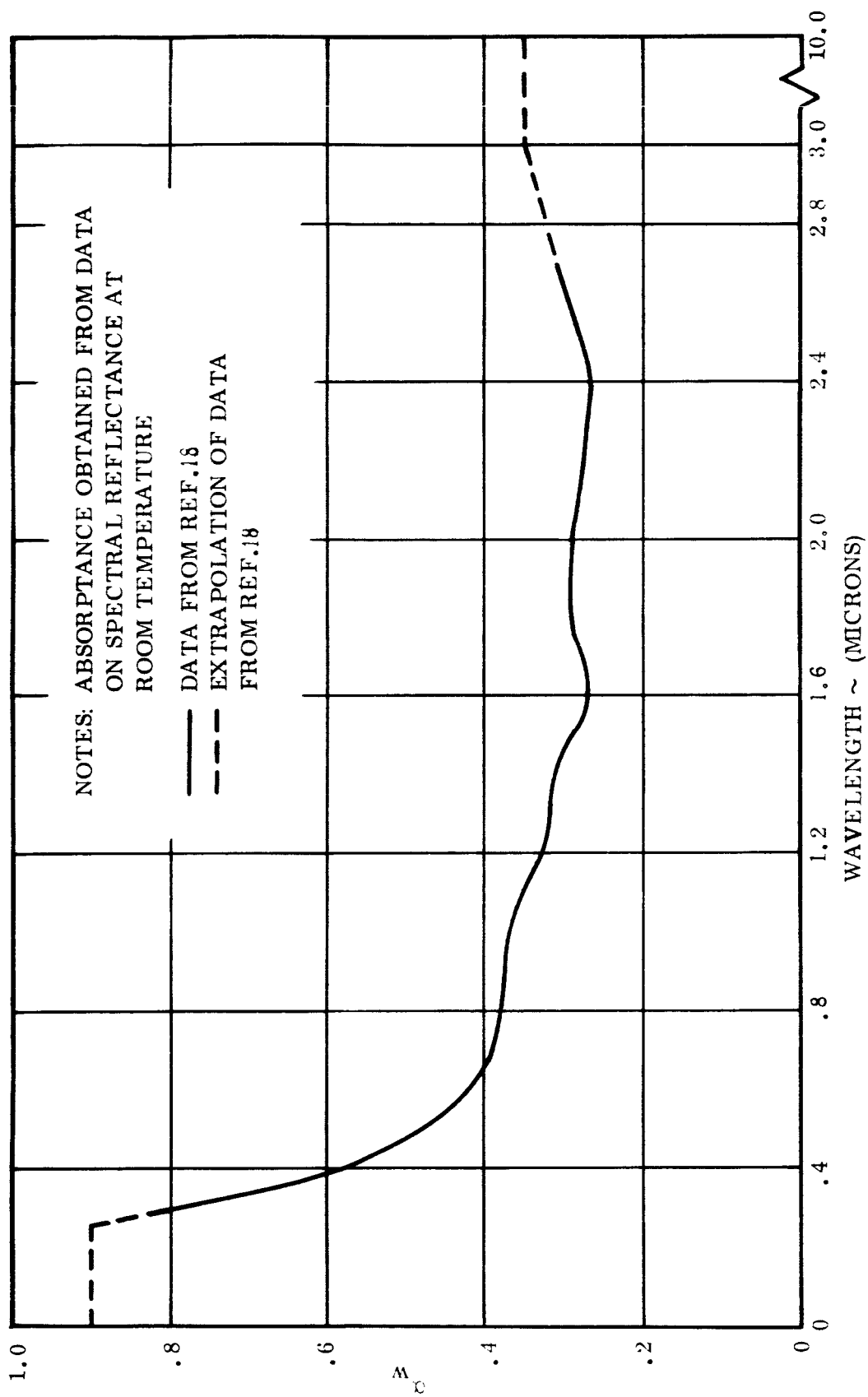


Figure 33. Spectral Absorptance of Beryllium Oxide

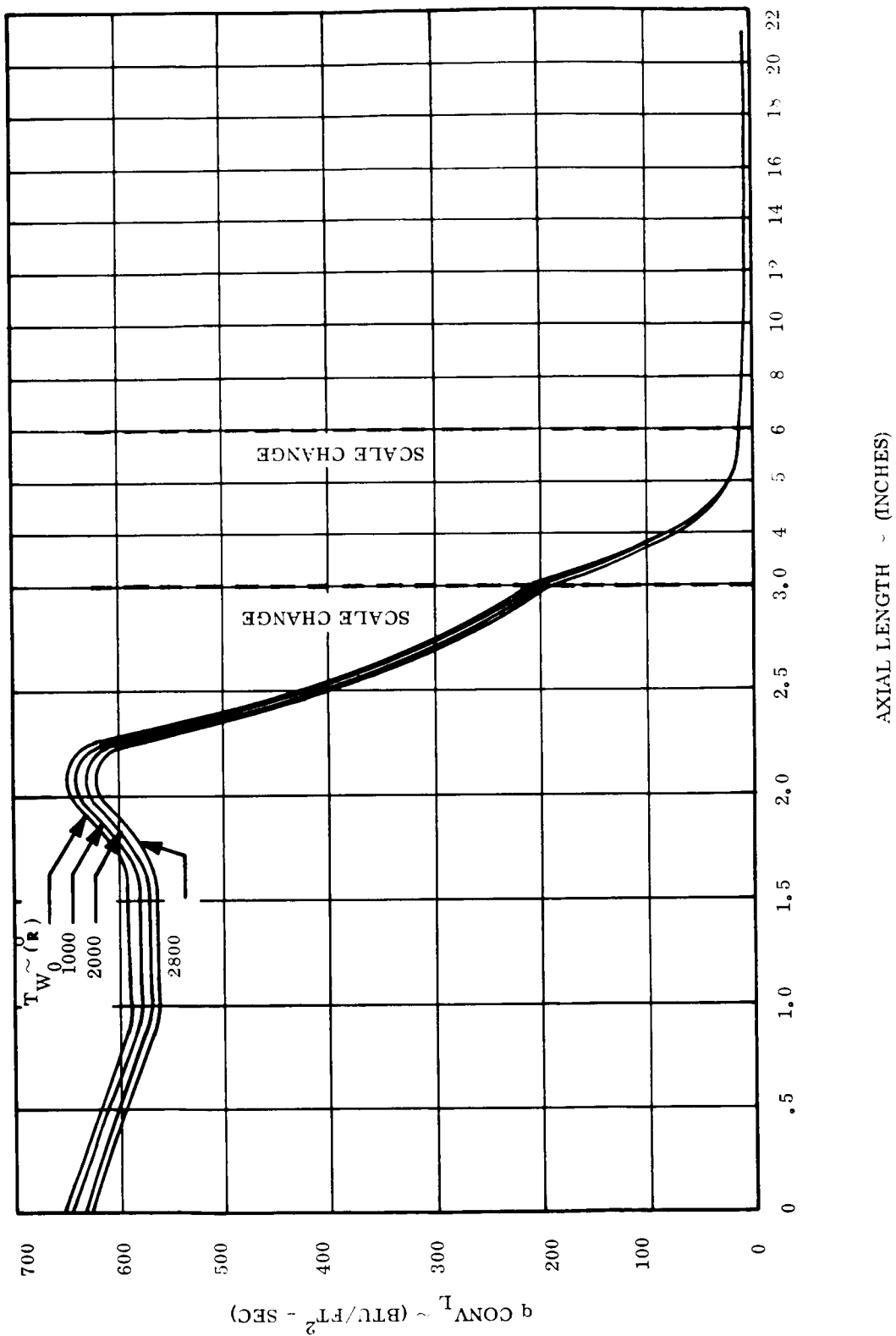


Figure 34. Laminar Convective Heat Flux on FIRE Vehicle

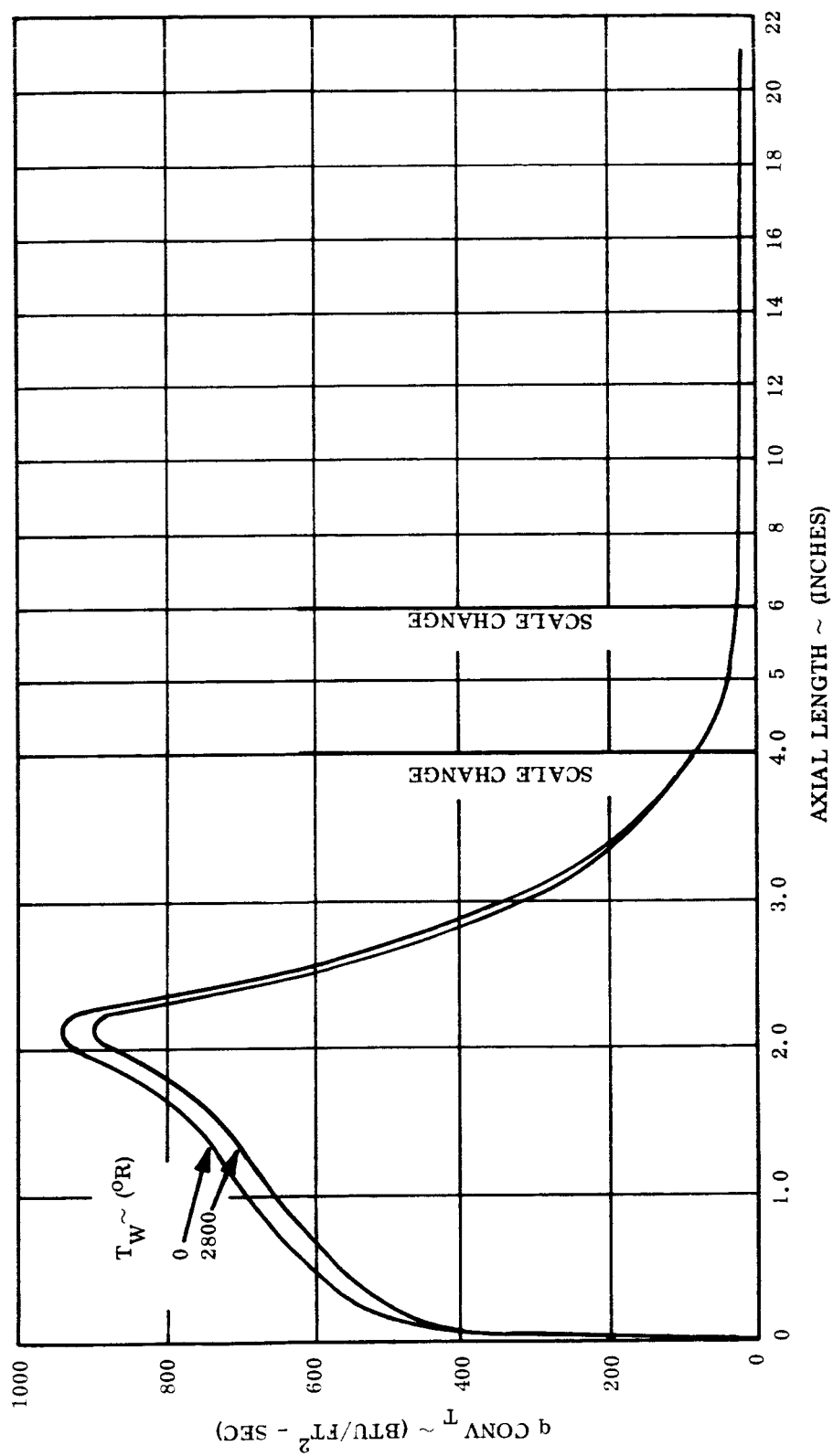


Figure 35. Turbulent Convective Heat Flux on FIRE Vehicle

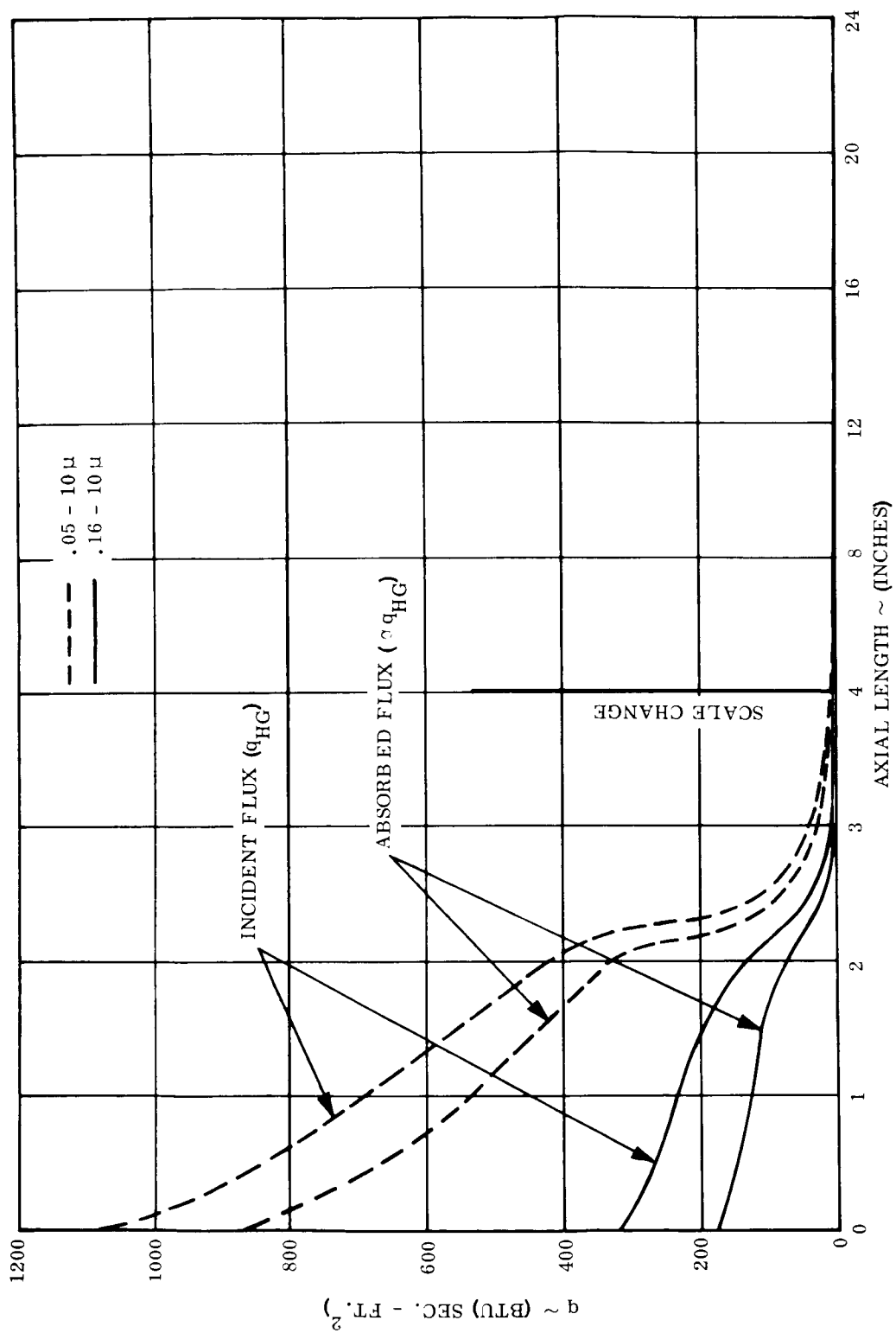


Figure 36. Radiative Heat Flux on FIRE Vehicle

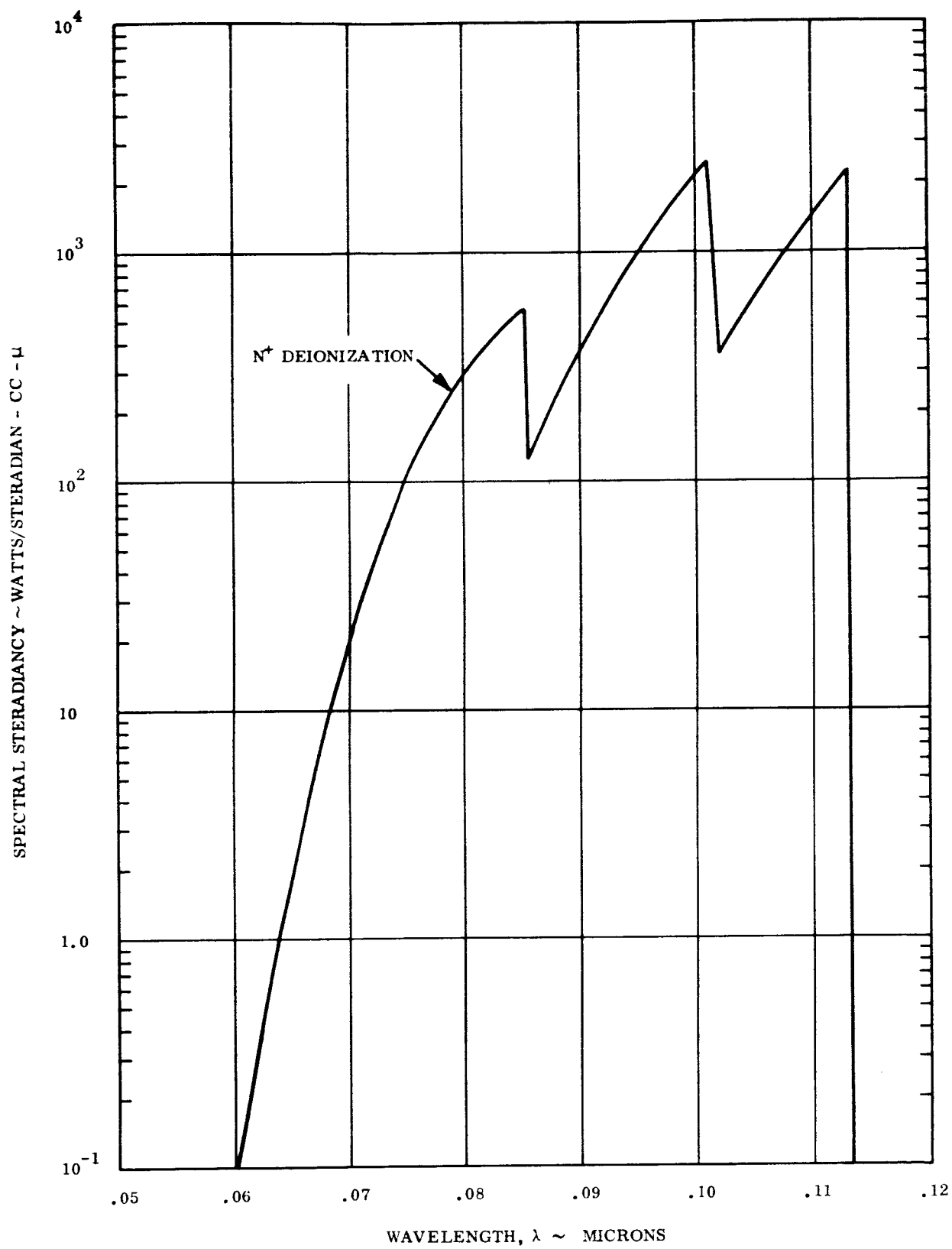


Figure 37. Spectral Steradiance of N^+ Deionization - Wavelength .05 μ to .16 μ

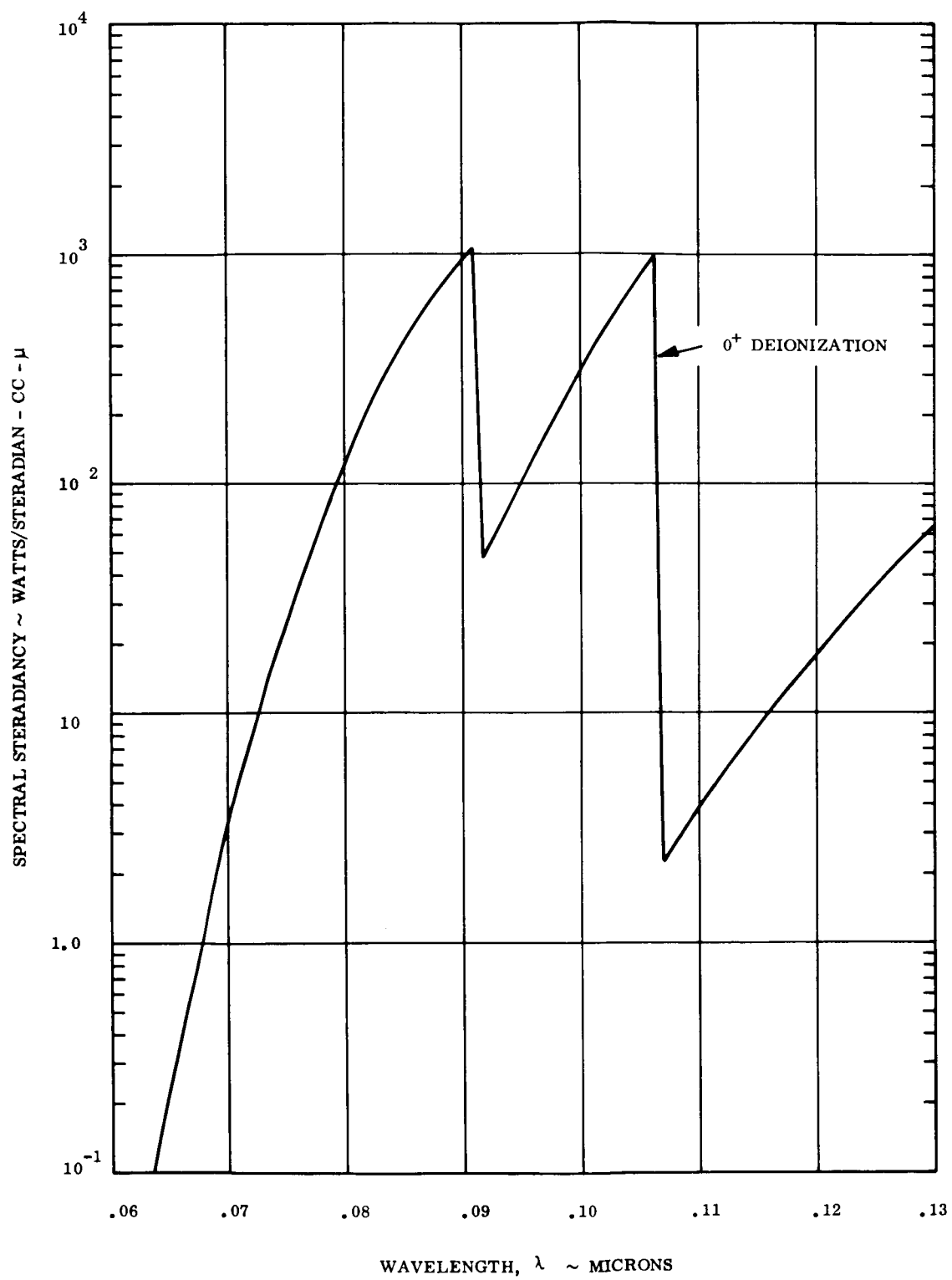


Figure 38. Spectral Steradiance of O⁺ Deionization - Wavelength .05 to .13 μ

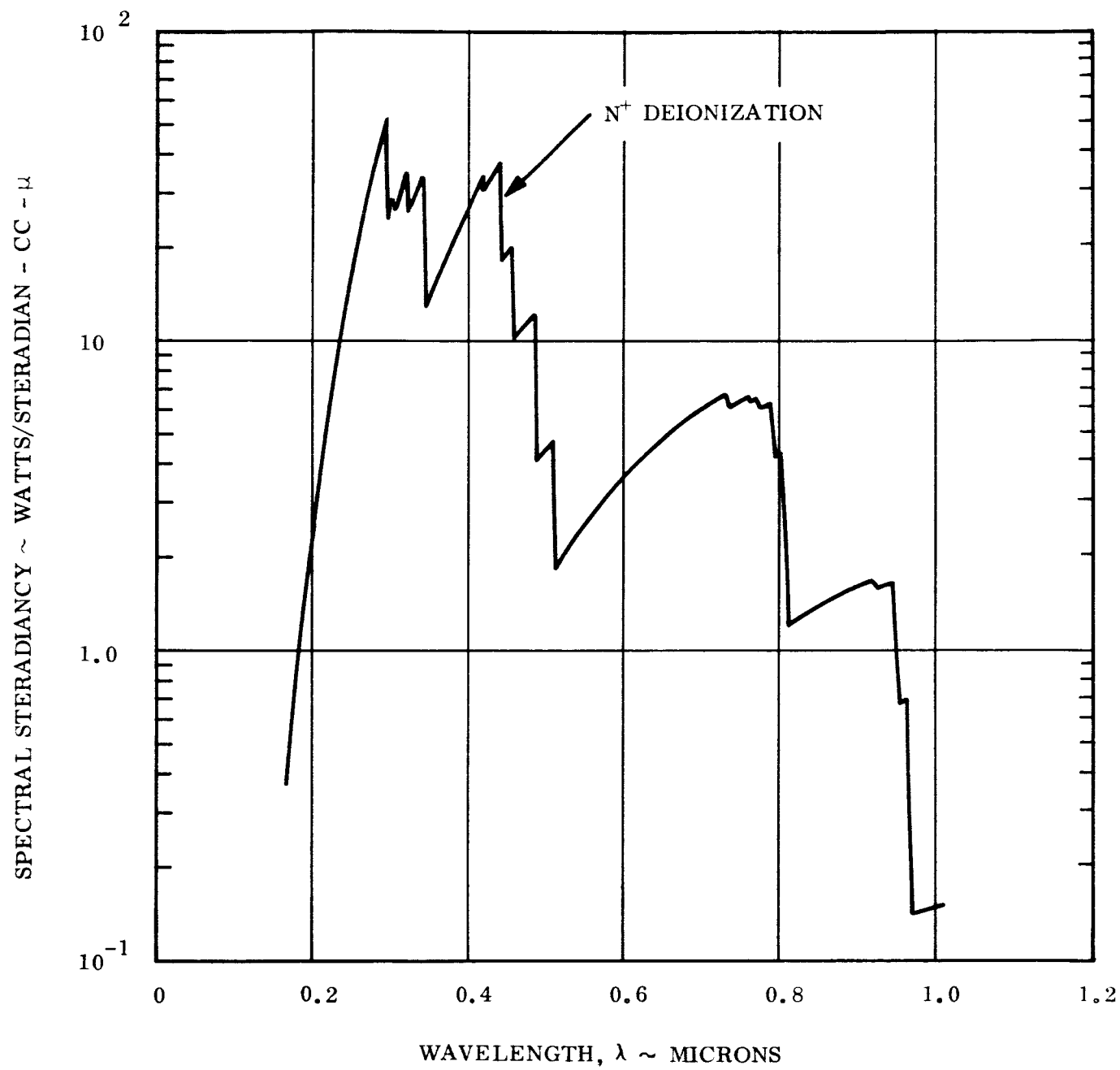


Figure 39. Spectral Steradiance of N⁺ Deionization - Wavelength .16 to 10μ

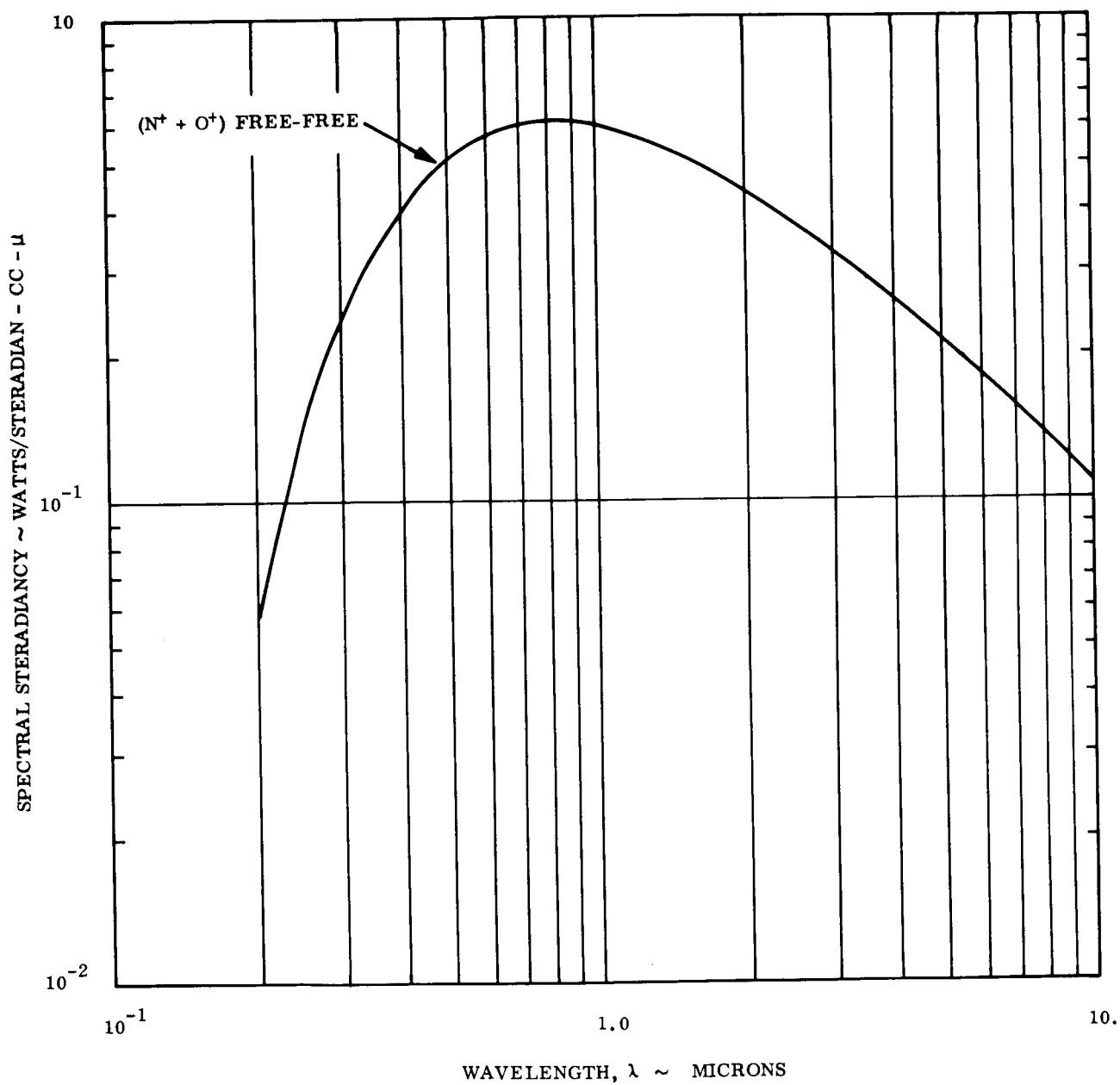


Figure 40. Spectral Steradiance of $(N^+ + O^+)$ Free-Free - Wavelength .16 to 10 μ

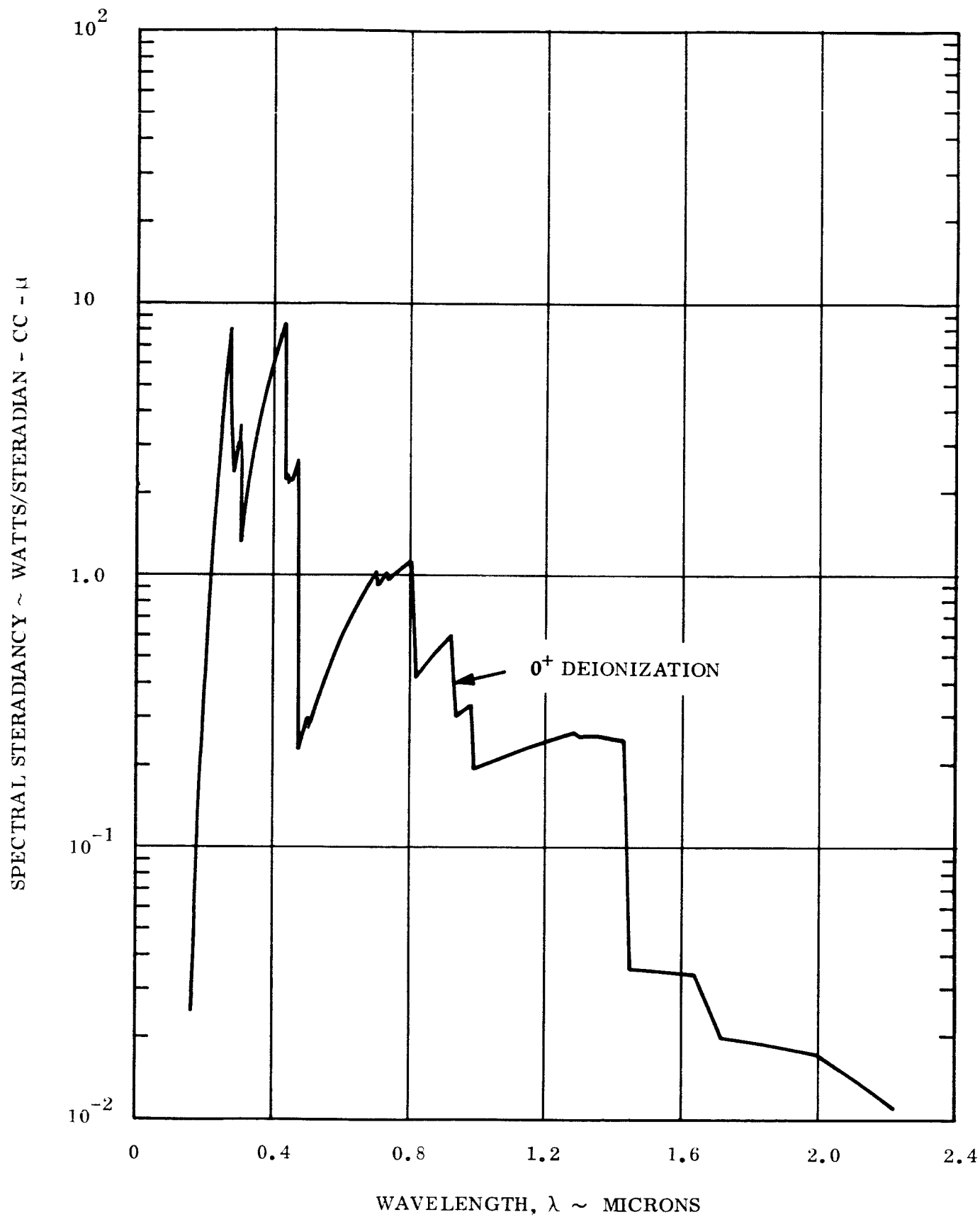


Figure 41. Spectral Steradiance of O^+ Deionization - Wavelength .16 to 10 μ

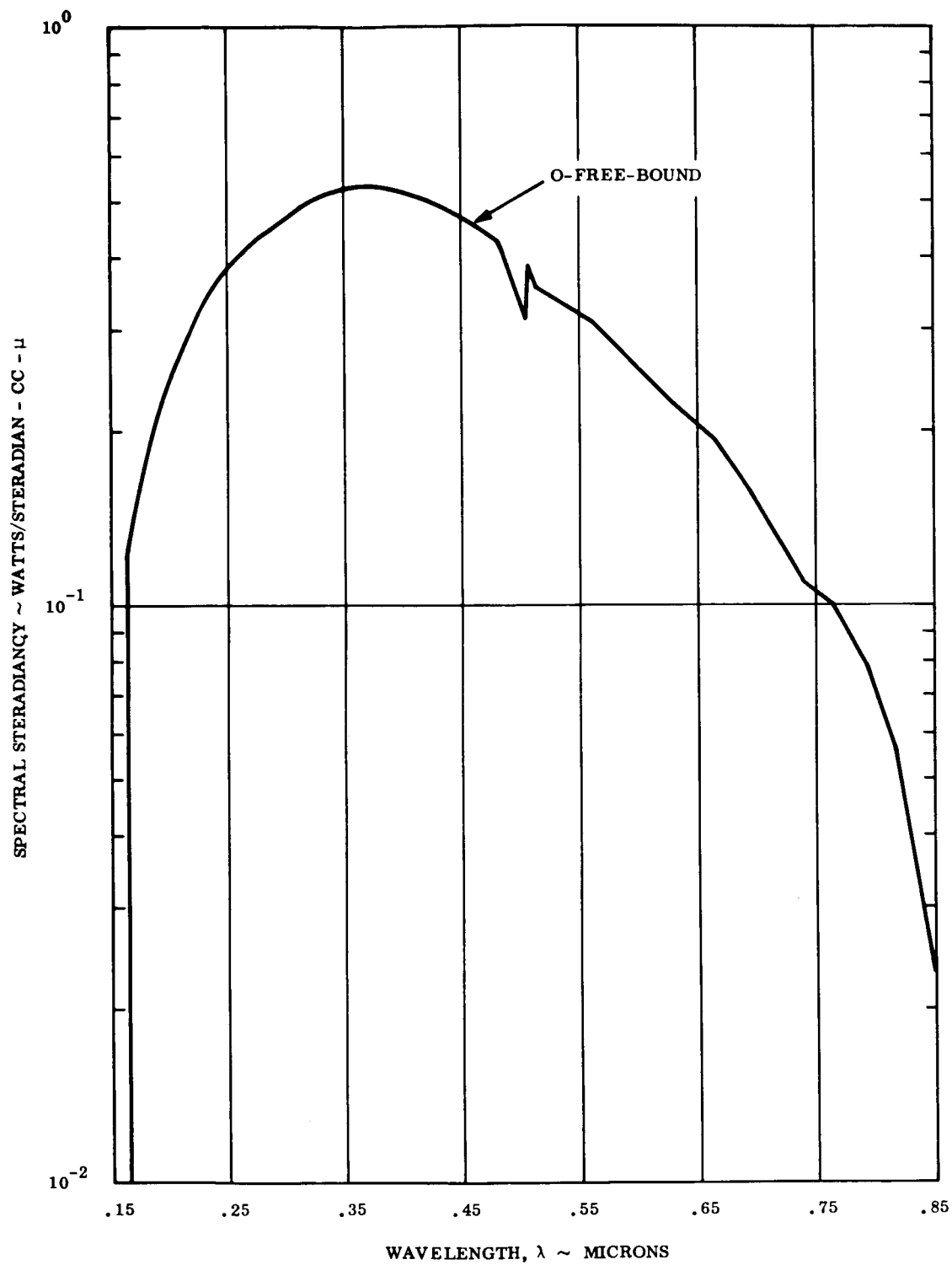


Figure 42. Spectral Steradiance of O^- Free-Bound Wavelength .16 to 10 μ

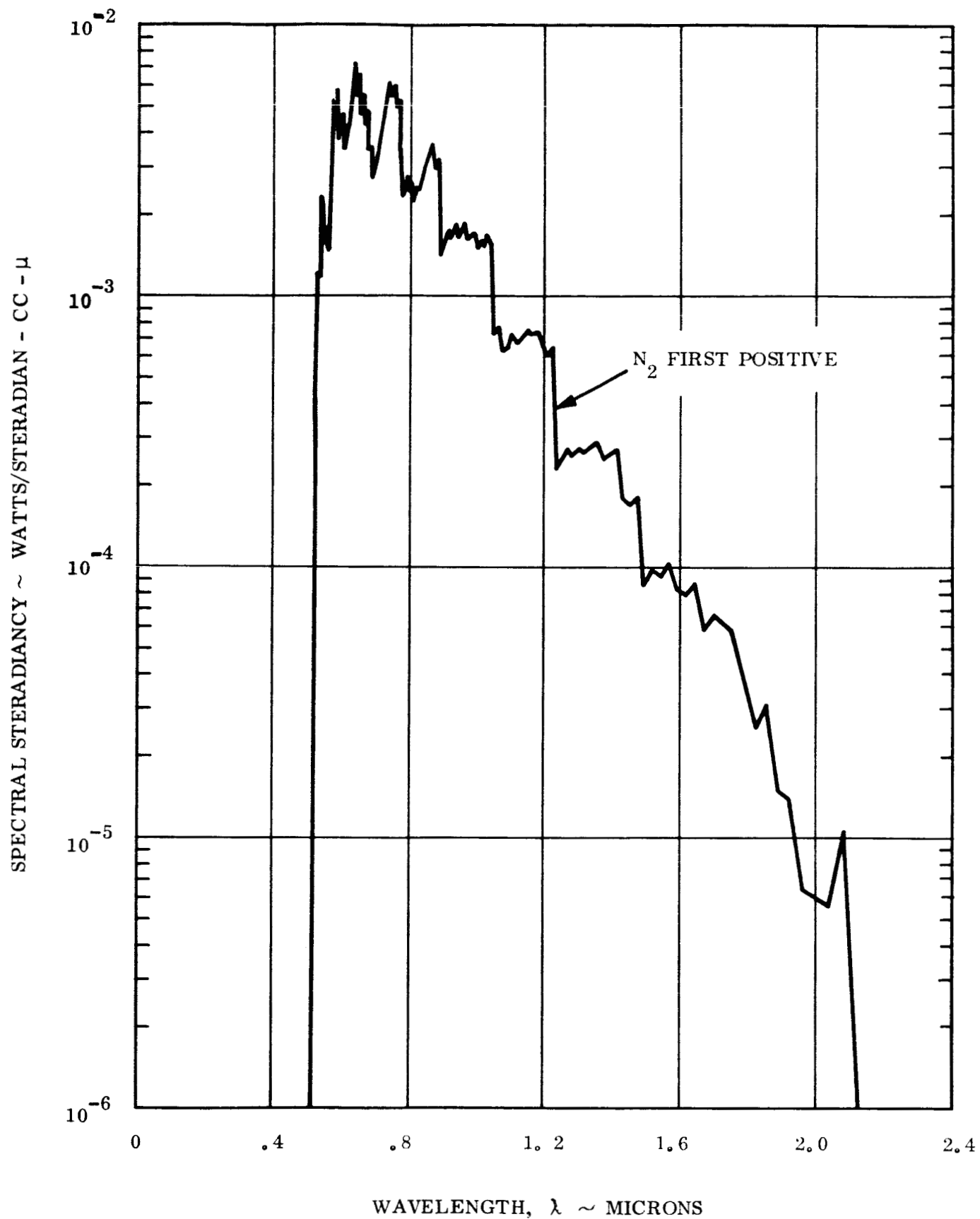


Figure 43. Spectral Steradiance of N_2 First Positive-Wavelength .16 to 10μ

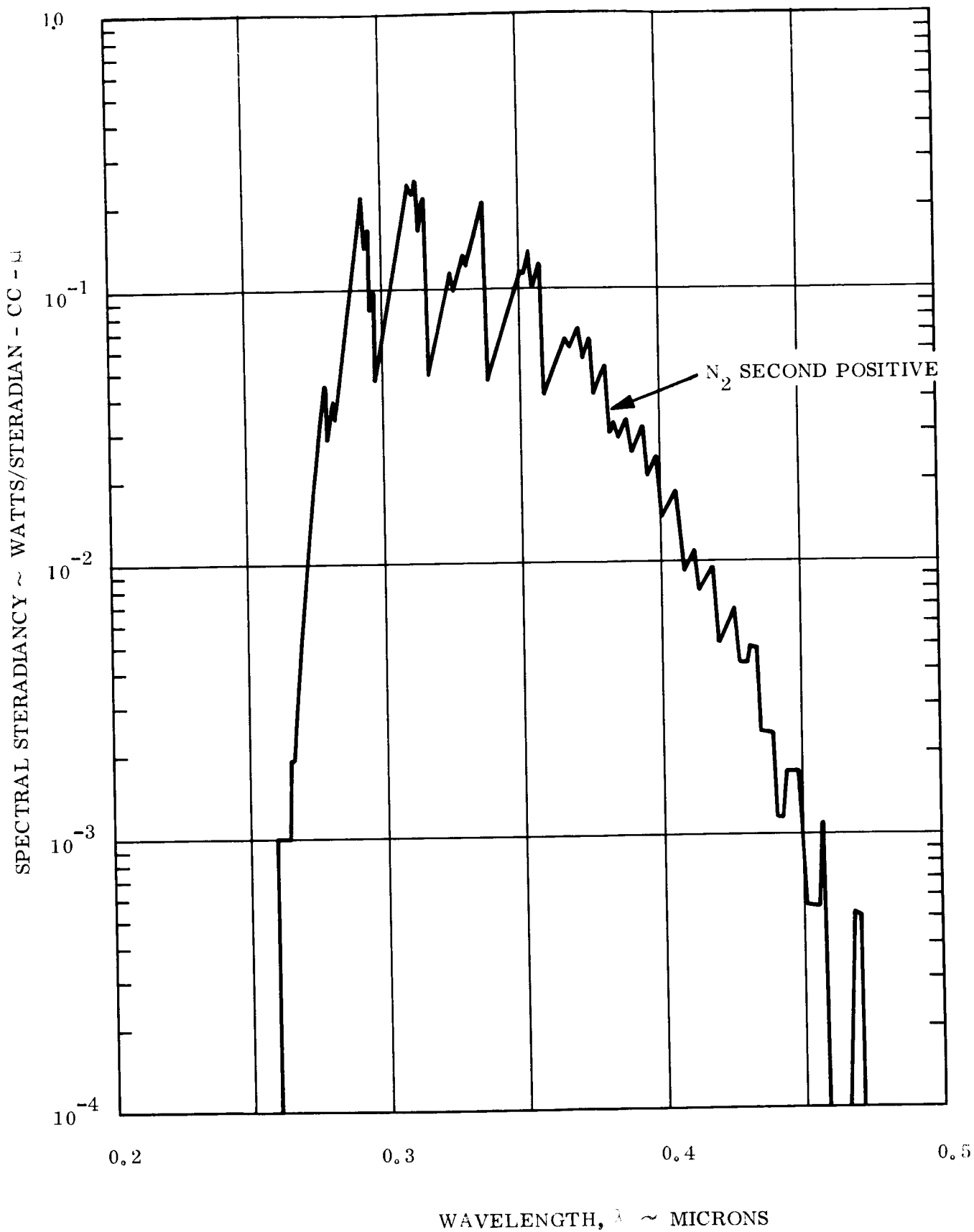


Figure 44. Spectral Steradiancy of N₂ Second Positive-Wavelength .16 to 10μ

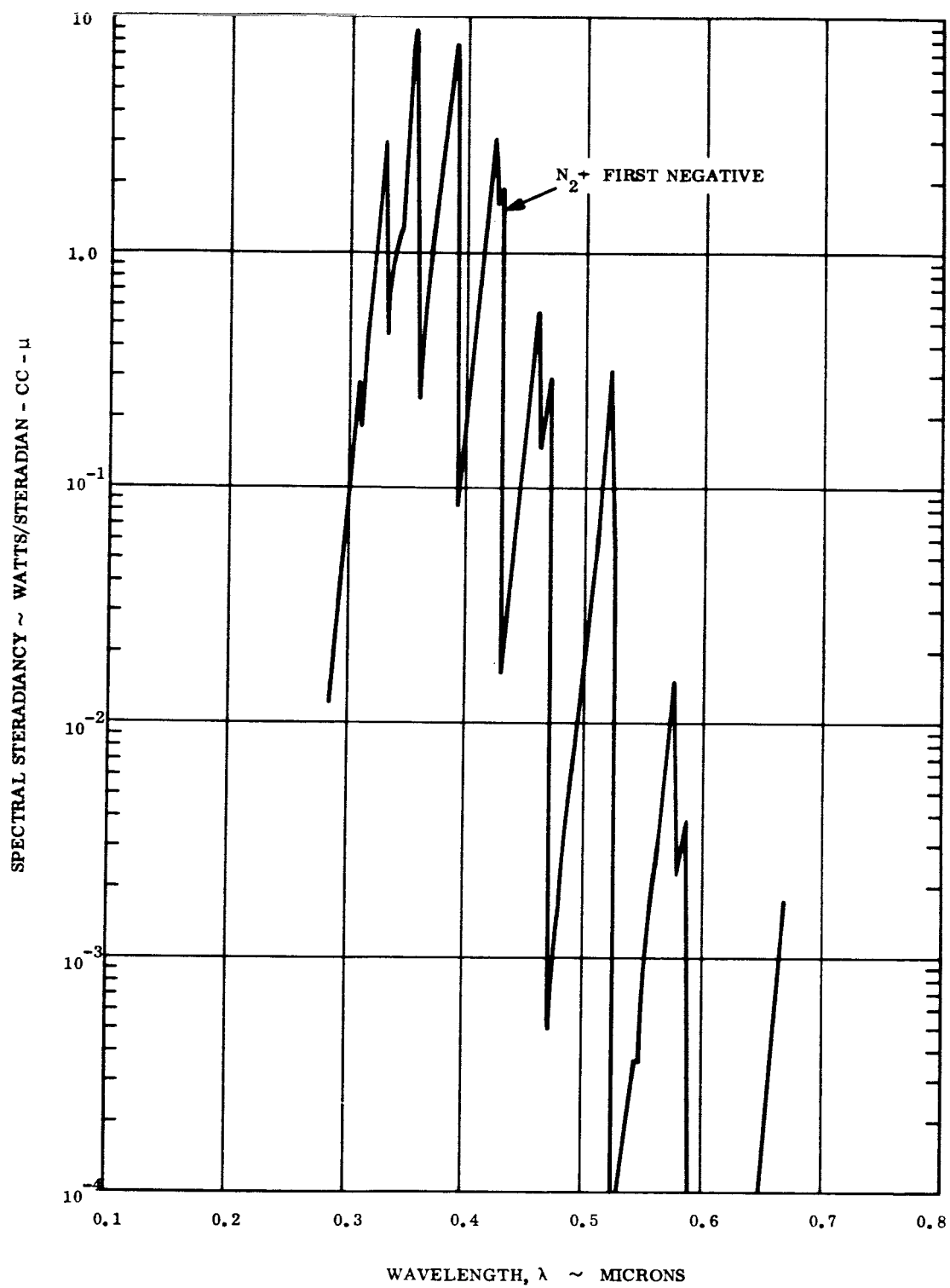


Figure 45. Spectral Steradiance of N_2 First Negative - Wavelength .16 to 10μ

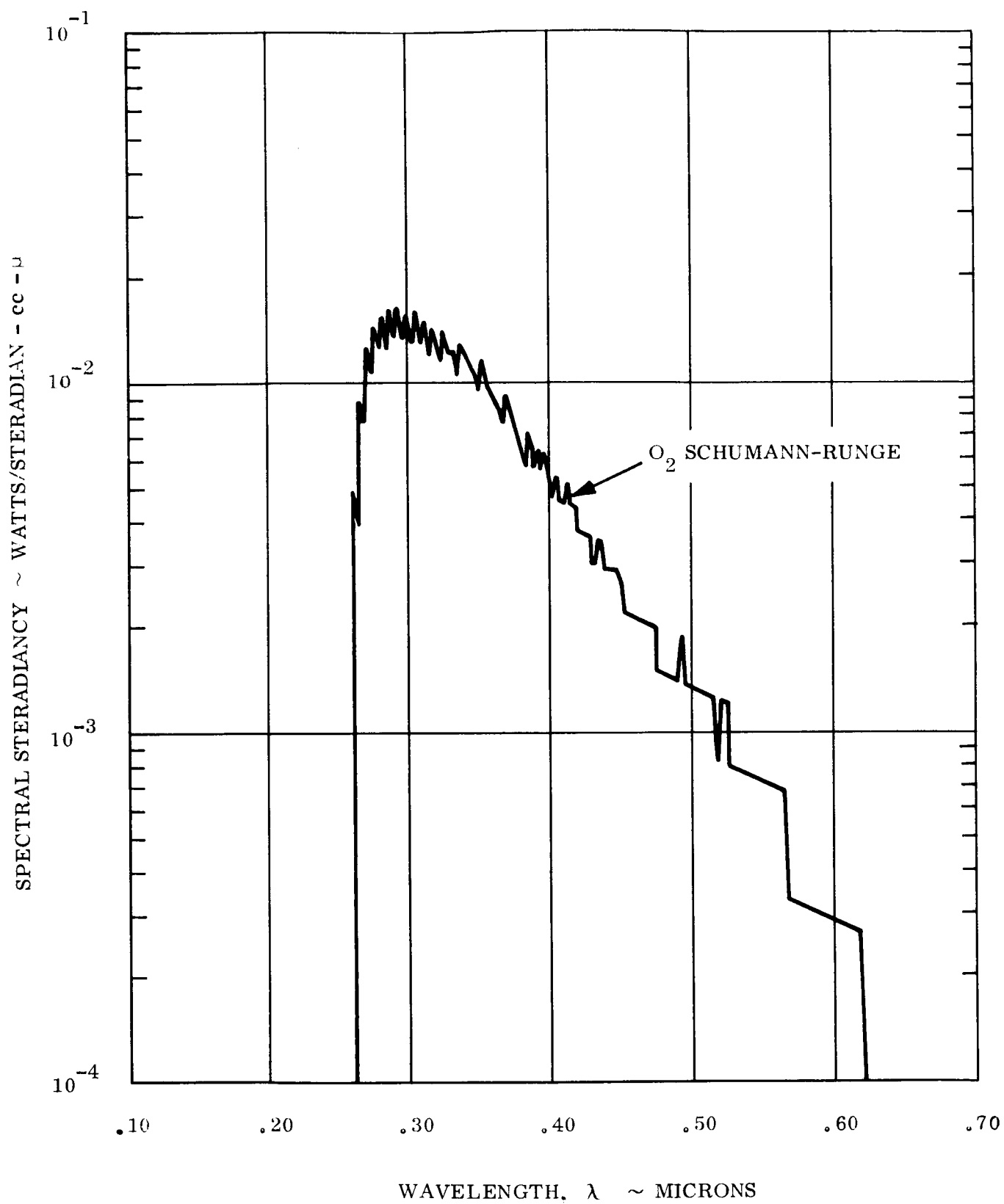


Figure 46. Spectral Steradiance of O_2 Schumann-Runge - Wavelength .16 to 10μ

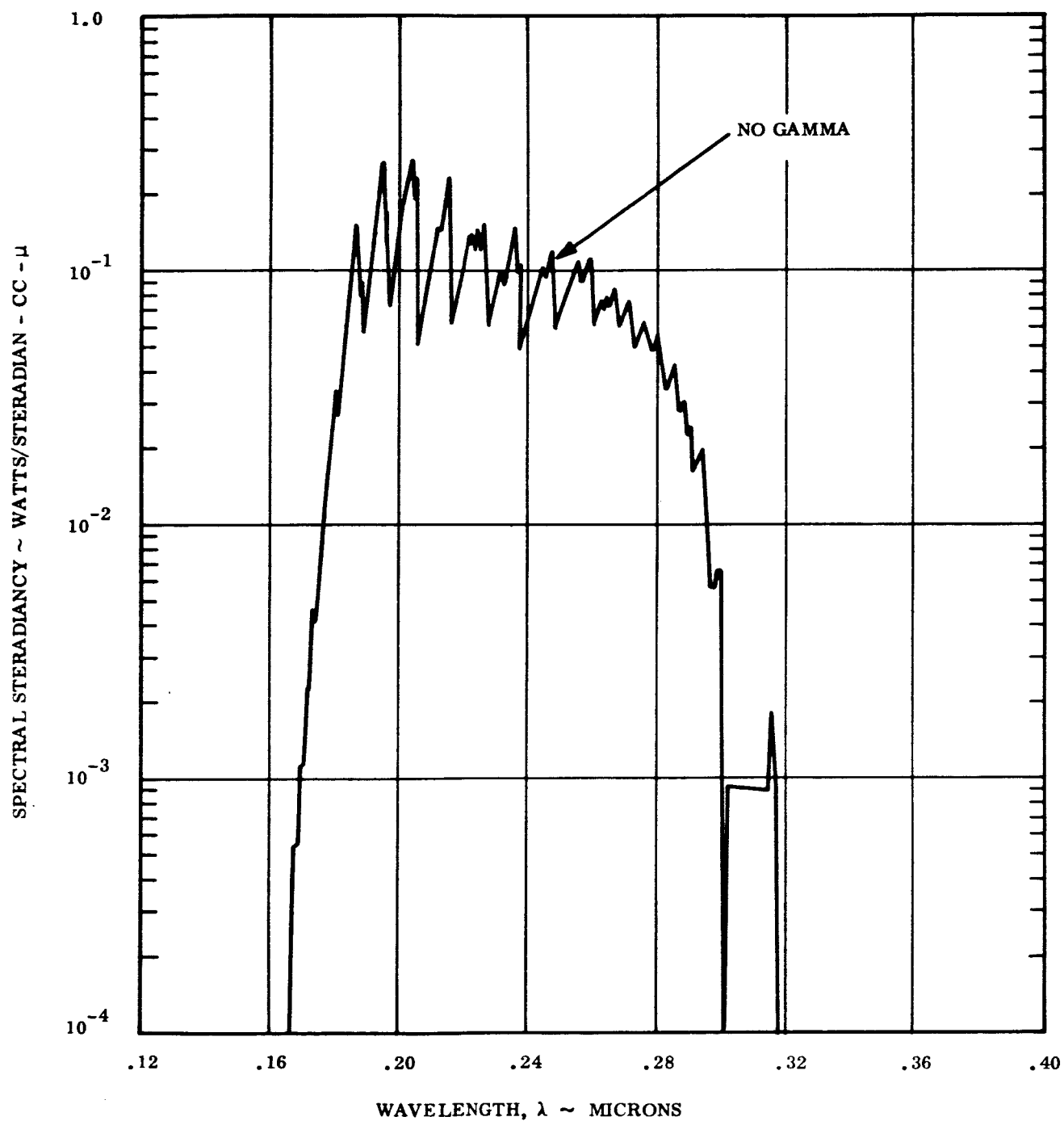


Figure 47. Spectral Steradiancy of NO Gamma - Wavelength .16 to 10 μ

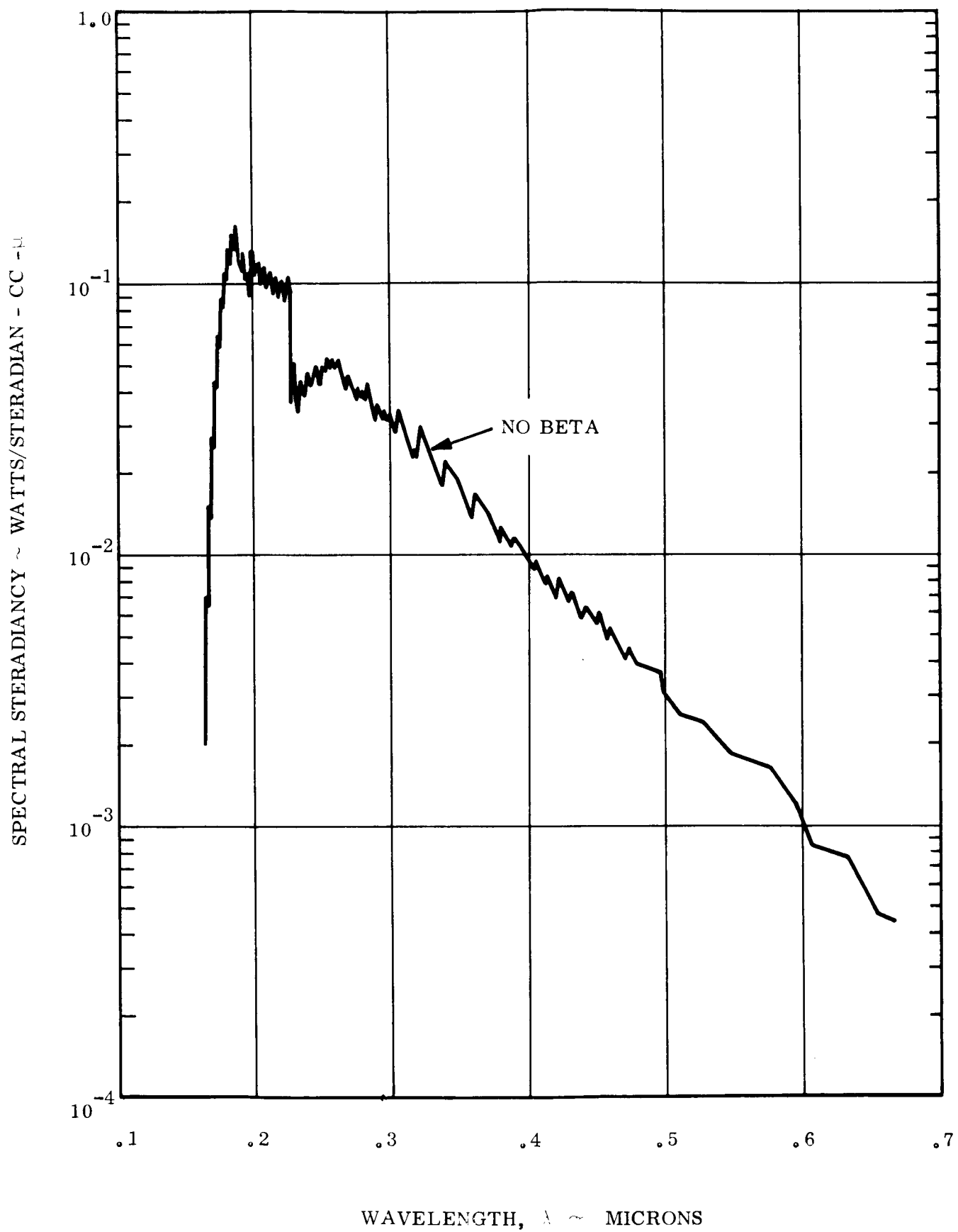


Figure 48. Spectral Steradiancy of NO Beta - Wavelength .16 to 10μ

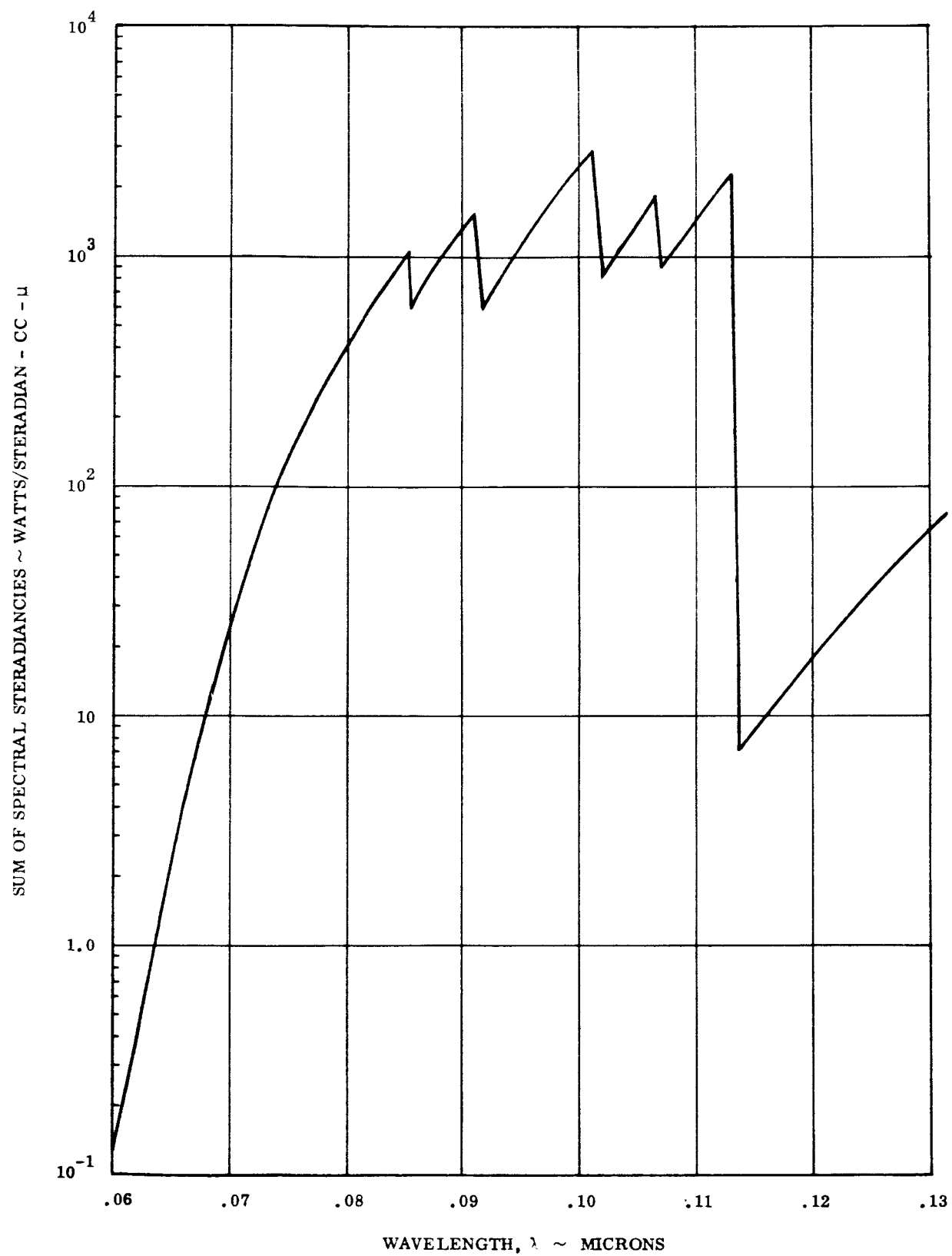


Figure 49. Sum of Spectral Steradiancey - Wavelength .05 to 16 μ

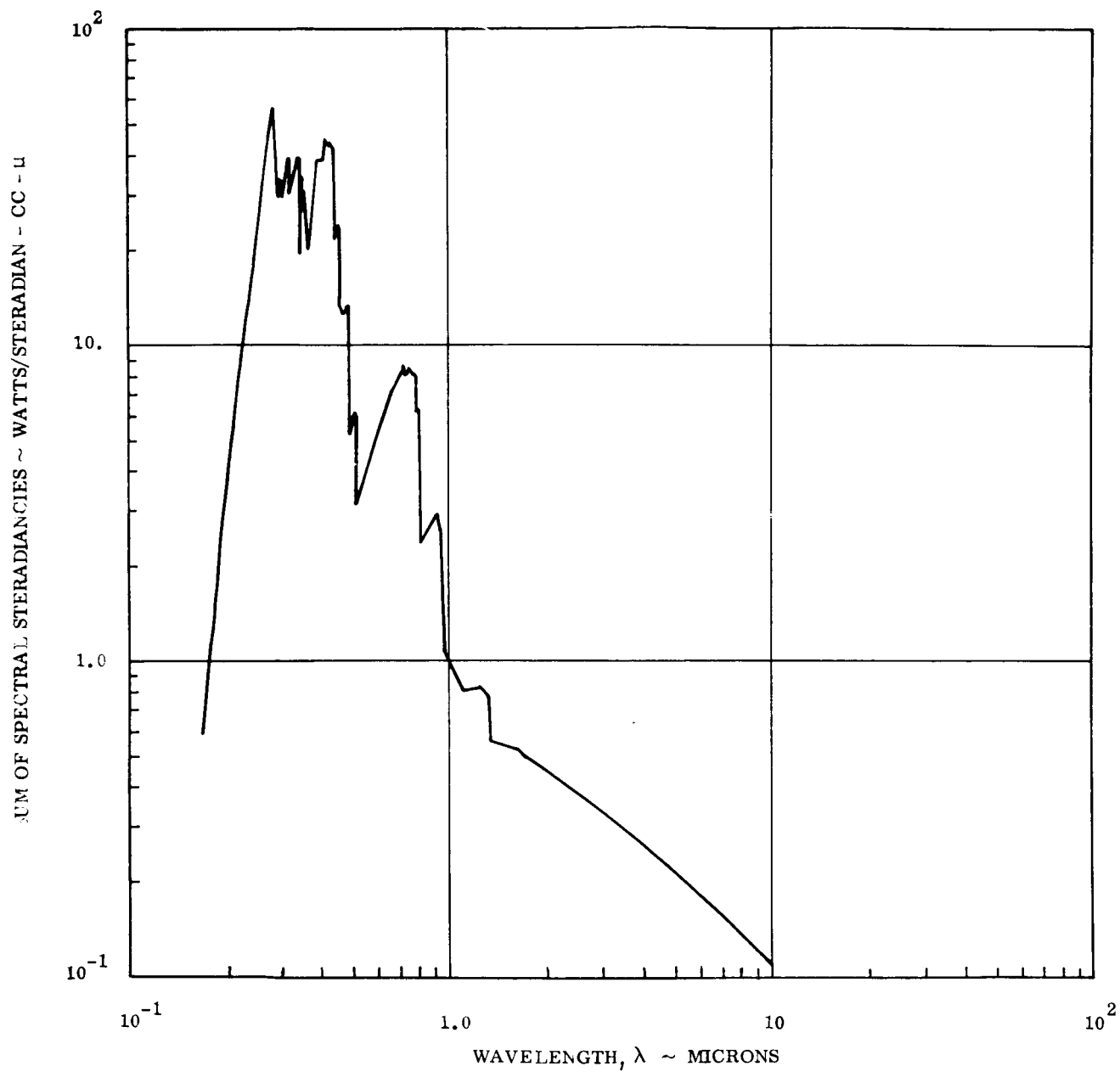


Figure 50. Sum of Spectral Steradiancy - Wavelength .16 to 10 μ

TABLE 1. SUBSONIC AND TRANSONIC REGION-TABULATION OF RESULTS

χ/D	r/D	$T(^{\circ}K)$	$\log_{10}(p/p_0)$	N_e	N_{O_2}	N_{N_2}	N_{NO}	N_O	N_N	N_{O^+}	N_{N^+}	N_{O^-}
.00688	.125	11125	-2.04	4.00×10^{16}	3.3×10^{11}	2.5×10^{14}	1.4×10^{13}	9.7×10^{16}	3.3×10^{17}	5.0×10^{15}	2.8×10^{16}	1.9×10^{12}
.00640	.125	11127	-2.04	4.00×10^{16}	3.3×10^{11}	2.5×10^{14}	1.3×10^{13}	9.7×10^{16}	3.3×10^{17}	5.0×10^{15}	2.8×10^{16}	1.9×10^{12}
.00498	.125	11126	-2.04	4.00×10^{16}	3.3×10^{11}	2.5×10^{14}	1.3×10^{13}	9.7×10^{16}	3.3×10^{17}	5.0×10^{15}	2.8×10^{16}	1.9×10^{12}
.00266	.125	11124	-2.04	4.00×10^{16}	3.3×10^{11}	2.5×10^{14}	1.4×10^{13}	9.7×10^{16}	3.3×10^{17}	5.0×10^{15}	2.8×10^{16}	1.9×10^{12}
-.00048	.125	11123	-2.04	4.00×10^{16}	3.3×10^{11}	2.5×10^{14}	1.4×10^{13}	9.7×10^{16}	3.3×10^{17}	5.0×10^{15}	2.8×10^{16}	1.9×10^{12}
-.00436	.125	11121	-2.04	4.00×10^{16}	3.4×10^{11}	2.5×10^{14}	1.4×10^{13}	9.7×10^{16}	3.3×10^{17}	5.0×10^{15}	2.8×10^{16}	1.9×10^{12}
-.00888	.125	11118	-2.04	3.90×10^{16}	3.4×10^{11}	2.6×10^{14}	1.4×10^{13}	9.7×10^{16}	3.4×10^{17}	5.0×10^{15}	2.7×10^{16}	1.8×10^{12}
-.01397	.125	11112	-2.04	3.90×10^{16}	3.4×10^{11}	2.6×10^{14}	1.4×10^{13}	9.7×10^{16}	3.4×10^{17}	5.0×10^{15}	2.7×10^{16}	1.8×10^{12}
-.01953	.125	11111	-2.04	3.85×10^{16}	3.4×10^{11}	2.6×10^{14}	1.4×10^{13}	9.7×10^{16}	3.4×10^{17}	5.0×10^{15}	2.7×10^{16}	1.8×10^{12}
-.02552	.125	11108	-2.04	3.85×10^{16}	3.5×10^{11}	2.6×10^{14}	1.5×10^{13}	9.7×10^{16}	3.4×10^{17}	5.0×10^{15}	2.7×10^{16}	1.8×10^{12}
-.03186	.125	11102	-2.04	3.80×10^{16}	3.5×10^{11}	2.6×10^{14}	1.5×10^{13}	9.7×10^{16}	3.5×10^{17}	5.0×10^{15}	2.6×10^{16}	1.8×10^{12}
-.03843	.125	11093	-2.04	3.75×10^{16}	3.5×10^{11}	2.6×10^{14}	1.5×10^{13}	9.7×10^{16}	3.5×10^{17}	5.0×10^{15}	2.6×10^{16}	1.7×10^{12}
-.04186	.125	11089	-2.04	3.70×10^{16}	3.5×10^{11}	2.6×10^{14}	1.5×10^{13}	9.7×10^{16}	3.5×10^{17}	5.0×10^{15}	2.6×10^{16}	1.7×10^{12}
.07282	.425	10898	-2.104	3.1×10^{16}	2.8×10^{11}	2.5×10^{14}	1.2×10^{13}	9.5×10^{16}	3.0×10^{17}	4.4×10^{15}	2.2×10^{16}	1.3×10^{12}
.07185	.425	10894	-2.104	3.1×10^{16}	2.8×10^{11}	2.5×10^{14}	1.2×10^{13}	9.5×10^{16}	3.1×10^{17}	4.4×10^{15}	2.2×10^{16}	1.3×10^{12}
.06902	.425	10884	-2.102	3.0×10^{16}	2.8×10^{11}	2.5×10^{14}	1.2×10^{13}	9.5×10^{16}	3.2×10^{17}	4.4×10^{15}	2.2×10^{16}	1.3×10^{12}
.06513	.425	10871	-2.100	3.0×10^{16}	2.8×10^{11}	2.5×10^{14}	1.2×10^{13}	9.5×10^{16}	3.3×10^{17}	4.0×10^{15}	2.2×10^{16}	1.3×10^{12}
.05932	.425	10850	-2.094	3.0×10^{16}	2.8×10^{11}	2.7×10^{14}	1.3×10^{13}	9.6×10^{16}	3.3×10^{17}	4.0×10^{15}	2.1×10^{16}	1.3×10^{12}
.05228	.425	10824	-2.089	2.95×10^{16}	2.9×10^{11}	2.9×10^{14}	1.3×10^{13}	9.6×10^{16}	3.4×10^{17}	4.0×10^{15}	2.1×10^{16}	1.4×10^{12}
.04552	.425	10794	-2.084	2.9×10^{16}	3.0×10^{11}	3.1×10^{14}	1.5×10^{13}	9.6×10^{16}	3.4×10^{17}	4.0×10^{15}	2.0×10^{16}	1.4×10^{12}
.03676	.425	10751	-2.077	2.8×10^{16}	3.1×10^{11}	3.3×10^{14}	1.6×10^{13}	9.7×10^{16}	3.4×10^{17}	3.9×10^{15}	1.9×10^{16}	1.4×10^{12}
.02737	.425	10694	-2.070	2.7×10^{16}	3.5×10^{11}	3.5×10^{14}	1.6×10^{13}	9.8×10^{16}	3.5×10^{17}	3.8×10^{15}	1.9×10^{16}	1.4×10^{12}

NOTES: $p_0 = 2.509 \times 10^{-13}$ Slugs/Ft³

All Concentrations are given in PARTICLES/CC

TABLE 1. SUBSONIC AND TRANSONIC REGION-TABULATION OF RESULTS (Cont.)

χ/D	r/D	T (°K)	$\log_{10}(\rho/\rho_0)$	N_e	N_{O_2}	N_{N_2}	N_{NO}	N_O	N_N	N_{O^+}	N_{N^+}	N_{O^-}
.01865	.425	10627	-2.062	2.6×10^{16}	4.0×10^{11}	4.0×10^{14}	1.9×10^{13}	1.0×10^{17}	3.6×10^{17}	3.6×10^{15}	1.9×10^{16}	1.4×10^{12}
.01125	.425	10542	-2.054	2.5×10^{16}	4.4×10^{11}	4.5×10^{14}	2.0×10^{13}	1.1×10^{17}	3.7×10^{17}	3.4×10^{15}	1.8×10^{16}	1.5×10^{12}
.09306	.475	10044	-2.34	1.2×10^{16}	1.6×10^{11}	2.2×10^{14}	7.0×10^{12}	5.1×10^{16}	1.9×10^{17}	1.6×10^{15}	8.7×10^{15}	3.0×10^{11}
.09256	.475	10052	-2.34	1.2×10^{16}	1.6×10^{11}	2.2×10^{14}	7.0×10^{12}	5.1×10^{16}	1.9×10^{17}	1.6×10^{15}	8.8×10^{15}	3.0×10^{11}
.09106	.475	10075	-2.33	1.3×10^{16}	1.6×10^{11}	2.2×10^{14}	7.0×10^{12}	5.5×10^{16}	2.0×10^{17}	1.7×10^{15}	9.0×10^{15}	3.5×10^{11}
.08888	.475	10146	-2.30	1.4×10^{16}	1.8×10^{11}	2.8×10^{14}	7.5×10^{12}	6.0×10^{16}	2.1×10^{17}	1.9×10^{15}	9.7×10^{15}	4.0×10^{11}
.08649	.475	10221	-2.27	1.5×10^{16}	1.9×10^{11}	3.0×10^{14}	8.0×10^{12}	7.0×10^{16}	2.2×10^{17}	2.2×10^{15}	1.2×10^{16}	5.3×10^{11}
.08296	.475	10312	-2.24	1.6×10^{16}	1.9×10^{11}	3.0×10^{14}	9.0×10^{12}	7.0×10^{16}	2.5×10^{17}	2.4×10^{15}	1.2×10^{16}	6.2×10^{11}
.07877	.475	10394	-2.21	1.75×10^{16}	2.3×10^{11}	3.2×10^{14}	9.5×10^{12}	7.5×10^{16}	2.7×10^{17}	2.5×10^{15}	1.4×10^{16}	7.0×10^{11}
.07398	.475	10458	-2.18	1.9×10^{16}	2.7×10^{11}	3.4×10^{14}	9.5×10^{12}	7.5×10^{16}	3.0×10^{17}	2.6×10^{15}	1.6×10^{16}	8.0×10^{11}
.06980	.475	10488	-2.17	2.0×10^{16}	2.7×10^{11}	3.4×10^{14}	9.5×10^{12}	7.0×10^{16}	3.0×10^{17}	2.7×10^{15}	1.7×10^{16}	8.5×10^{11}
.06413	.475	10496	-2.15	2.1×10^{16}	2.7×10^{11}	3.8×10^{14}	9.5×10^{12}	7.0×10^{16}	3.0×10^{17}	2.8×10^{15}	1.7×10^{16}	8.5×10^{11}
.05807	.475	10468	-2.14	2.0×10^{16}	2.7×10^{11}	4.0×10^{14}	9.5×10^{12}	7.0×10^{16}	3.0×10^{17}	2.6×10^{15}	1.8×10^{16}	9.0×10^{11}
.05164	.475	10432	-2.13	2.0×10^{16}	2.8×10^{11}	4.1×10^{14}	9.5×10^{12}	7.0×10^{16}	3.0×10^{17}	2.8×10^{15}	1.6×10^{16}	9.0×10^{11}
.04594	.475	10391	-2.12	1.9×10^{16}	2.8×10^{11}	4.5×10^{14}	9.5×10^{12}	7.0×10^{16}	3.1×10^{17}	2.8×10^{15}	1.5×10^{16}	9.0×10^{11}
.03915	.475	10318	-2.11	1.8×10^{16}	2.9×10^{11}	5.5×10^{14}	1.0×10^{13}	7.5×10^{16}	3.1×10^{17}	2.7×10^{15}	1.4×10^{16}	9.0×10^{11}
.03238	.475	10206	-2.10	1.6×10^{16}	2.9×10^{11}	6.0×10^{14}	1.0×10^{13}	7.5×10^{16}	3.2×10^{17}	2.6×10^{15}	1.3×10^{16}	9.0×10^{11}
.02677	.475	10058	-2.08	1.4×10^{16}	3.0×10^{11}	8.1×10^{14}	1.2×10^{13}	7.5×10^{16}	3.4×10^{17}	2.4×10^{15}	1.1×10^{16}	8.5×10^{11}
.02261	.475	9918	-2.06	1.2×10^{16}	3.0×10^{11}	1.2×10^{15}	1.5×10^{13}	7.5×10^{16}	3.6×10^{17}	2.1×10^{15}	1.0×10^{16}	8.5×10^{11}
.02014	.475	9781	-2.05	1.0×10^{16}	3.2×10^{11}	1.4×10^{15}	1.6×10^{13}	7.5×10^{16}	3.8×10^{17}	1.8×10^{15}	8.0×10^{15}	8.5×10^{11}

TABLE 2. SUPERSONIC REGION-TABULATION OF RESULTS

χ	r	$T(^{\circ}K)$	$\log_{10}(\rho/\rho_0)$	N_e	N_{O_2}	N_{N_2}	N_{NO}	N_O	N_N	N_{O^+}	N_{N^+}	N_{O^-}
.093	.47616	10028	-2.344	1.1×10^{16}	1.9×10^{11}	2.8×10^{14}	7.5×10^{12}	5.5×10^{16}	1.8×10^{17}	1.5×10^{15}	7.5×10^{15}	2.3×10^{11}
.093	.47829	9987	-2.353	9.5×10^{15}	1.8×10^{11}	2.9×10^{14}	7.0×10^{12}	5.5×10^{16}	1.8×10^{17}	1.5×10^{15}	7.0×10^{15}	2.5×10^{11}
.093	.47959	9959	-2.359	9.0×10^{15}	1.8×10^{11}	2.9×10^{14}	7.0×10^{12}	5.5×10^{16}	1.8×10^{17}	1.5×10^{15}	7.0×10^{15}	3.0×10^{11}
.093	.48775	9862	-2.372	8.5×10^{15}	1.9×10^{11}	3.0×10^{14}	7.0×10^{12}	5.2×10^{16}	1.7×10^{17}	1.4×10^{15}	6.5×10^{15}	3.0×10^{11}
.093	.50985	9792	-2.349	8.0×10^{15}	2.0×10^{11}	3.2×10^{14}	8.5×10^{12}	5.5×10^{16}	1.7×10^{17}	1.2×10^{15}	6.0×10^{15}	3.0×10^{11}
.093	.52677	9687	-2.341	7.0×10^{15}	2.1×10^{11}	4.0×10^{14}	9.0×10^{12}	5.5×10^{16}	1.8×10^{17}	1.1×10^{15}	5.5×10^{15}	2.8×10^{11}
.093	.56928	9129	-2.278	4.8×10^{15}	4.0×10^{11}	1.0×10^{15}	2.2×10^{13}	6.5×10^{16}	2.0×10^{17}	8.5×10^{14}	3.2×10^{15}	2.5×10^{11}
.093	.58803	8322	-2.184	1.9×10^{15}	8.0×10^{11}	7.0×10^{15}	7.0×10^{13}	8.6×10^{16}	2.7×10^{17}	3.5×10^{14}	1.4×10^{15}	2.2×10^{11}
.093	.59223	7838	-2.136	1.1×10^{15}	1.7×10^{12}	1.1×10^{16}	1.4×10^{14}	9.0×10^{16}	3.6×10^{17}	2.0×10^{14}	6.2×10^{14}	1.7×10^{11}
.093	.59698	7331	-2.066	5.9×10^{14}	3.4×10^{12}	3.5×10^{16}	3.7×10^{14}	1.3×10^{17}	2.8×10^{17}	1.4×10^{14}	2.5×10^{14}	1.5×10^{11}
.093	.59967	7158	-2.024	4.5×10^{14}	5.0×10^{12}	6.0×10^{16}	5.2×10^{14}	1.4×10^{17}	2.7×10^{17}	1.0×10^{14}	2.0×10^{14}	1.4×10^{11}
.4	.80357	6383	-2.68	6.0×10^{13}	9.5×10^{11}	1.8×10^{16}	8.0×10^{13}	2.9×10^{16}	5.0×10^{16}	1.4×10^{13}	1.5×10^{13}	6.5×10^9
.4	.77145	6390	-2.71	7.0×10^{13}	7.0×10^{13}	1.5×10^{16}	6.0×10^{14}	2.5×10^{16}	5.5×10^{16}	1.5×10^{13}	1.7×10^{13}	9.0×10^9
.4	.74425	6784	-2.81	9.5×10^{13}	1.8×10^{11}	7.0×10^{15}	3.2×10^{13}	2.0×10^{16}	6.0×10^{16}	1.8×10^{13}	7.0×10^{13}	6.2×10^9
.4	.71956	7012	-2.90	1.2×10^{14}	1.5×10^{11}	3.0×10^{15}	1.9×10^{13}	1.7×10^{16}	5.0×10^{16}	2.5×10^{13}	8.0×10^{13}	5.7×10^9
.4	.68161	7043	-3.00	1.1×10^{14}	6.5×10^{10}	2.4×10^{15}	1.0×10^{13}	1.4×10^{16}	4.0×10^{16}	2.0×10^{13}	6.5×10^{13}	4.0×10^9
.4	.64518	6953	-3.10	9.0×10^{13}	5.0×10^{10}	2.0×10^{15}	6.0×10^{12}	1.0×10^{16}	3.0×10^{16}	1.9×10^{13}	4.5×10^{13}	2.5×10^9
.4	.61078	6816	-3.19	7.5×10^{13}	3.2×10^{10}	1.7×10^{15}	6.0×10^{12}	9.0×10^{15}	2.5×10^{16}	1.2×10^{16}	3.4×10^{13}	1.4×10^9
.4	.58086	6641	-3.29	3.8×10^{13}	3.0×10^{10}	1.7×10^{15}	5.0×10^{12}	6.2×10^{15}	1.8×10^{16}	5.0×10^{12}	1.8×10^{13}	8.0×10^8
.4	.55020	6436	-3.40	2.4×10^{13}	2.9×10^{10}	1.3×10^{15}	4.0×10^{12}	5.0×10^{15}	1.4×10^{16}	4.5×10^{12}	1.6×10^{13}	4.5×10^8
.4	.52035	6297	-3.50	1.8×10^{13}	2.4×10^{10}	9.0×10^{14}	3.0×10^{12}	4.0×10^{15}	1.0×10^{16}	3.3×10^{12}	1.1×10^{13}	2.8×10^8
.4	.49451	6222	-3.50	1.3×10^{13}	2.3×10^{10}	1.0×10^{15}	3.2×10^{12}	4.0×10^{15}	1.0×10^{16}	2.8×10^{12}	6.0×10^{12}	2.3×10^8

NOTES: $\rho_0 = 2.509 \times 10^{-3}$ Slugs/Ft³

All Concentrations are given in PARTICLES/CC

TABLE 2. SUPERSONIC REGION-TABULATION OF RESULTS (Cont.)

χ	r	$T(^{\circ}K)$	$\log_{10}(c/c_0)$	N_e	N_{O_2}	N_{N_2}	N_{NO}	N_O	N_N	N_{O^+}	N_{N^+}	N_{O^-}
.4	.45459	6257	-3.5	1.35×10^{13}	2.2×10^{10}	1.0×10^{15}	3.3×10^{12}	4.0×10^{15}	1.0×10^{16}	2.9×10^{12}	--	2.4×10^8
.4	.43576	6264	-3.5	1.4×10^{13}	2.2×10^{10}	1.0×10^{15}	3.4×10^{12}	4.0×10^{15}	1.0×10^{16}	2.9×10^{12}	--	2.5×10^8
1.5	1.18543	2663	-2.36	8.5×10^8	--	--	--	--	--	--	--	--
1.5	1.11608	3496	-2.81	8.0×10^{10}	9.5×10^{14}	2.3×10^{16}	9.0×10^{14}	1.5×10^{16}	5.0×10^{13}	--	--	2.7×10^6
1.5	1.01036	5469	-3.27	4.8×10^{12}	1.6×10^{11}	6.5×10^{15}	2.3×10^{13}	6.5×10^{15}	7.0×10^{15}	2.7×10^{11}	--	2.2×10^8
1.5	.87065	5845	-3.47	8.0×10^{12}	4.5×10^{10}	2.0×10^{15}	6.0×10^{12}	4.5×10^{15}	9.0×10^{15}	8.0×10^{11}	--	1.8×10^8
1.5	.68887	5906	-3.60	6.5×10^{12}	2.5×10^{10}	8.7×10^{14}	3.3×10^{12}	3.0×10^{15}	7.5×10^{15}	1.5×10^{12}	--	1.2×10^8
1.5	.64449	5951	-3.58	7.0×10^{12}	2.5×10^{10}	9.0×10^{14}	3.2×10^{12}	3.2×10^{15}	8.0×10^{15}	1.5×10^{12}	--	1.4×10^8
1.5	.58750	6000	-3.57	7.7×10^{12}	2.6×10^{10}	9.5×10^{14}	3.0×10^{12}	3.2×10^{15}	8.5×10^{15}	1.5×10^{12}	2.7×10^{12}	1.5×10^8
1.5	.52735	6065	-3.52	9.0×10^{12}	2.7×10^{10}	1.3×10^{15}	3.7×10^{12}	3.6×10^{15}	9.0×10^{15}	1.6×10^{12}	3.0×10^{12}	1.7×10^8
1.5	.45340	6142	-3.52	1.2×10^{13}	2.5×10^{10}	1.0×10^{15}	3.8×10^{12}	3.7×10^{15}	9.0×10^{15}	2.0×10^{12}	3.8×10^{12}	2.0×10^8
1.5	.42899	6170	-3.51	1.3×10^{13}	2.3×10^{10}	9.0×10^{14}	3.5×10^{12}	3.8×10^{15}	9.5×10^{15}	2.7×10^{12}	6.0×10^{12}	2.2×10^8
1.5	.33349	6274	-3.48	1.6×10^{13}	4.3×10^{10}	8.5×10^{14}	3.7×10^{12}	4.2×10^{15}	1.2×10^{16}	3.1×10^{12}	6.5×10^{12}	3.0×10^8
1.5	.20921	6423	-3.43	2.1×10^{13}	2.6×10^{10}	8.0×10^{14}	4.5×10^{12}	4.7×10^{15}	1.3×10^{16}	1.2×10^{13}	1.2×10^{13}	4.0×10^8

TABLE 3. SHOCK WAVE SHAPE
(x-r ORIGIN AT STAGNATION POINT)

x/D	r/D	SHOCK WAVE ANGLE FROM AXIAL (RADIAN)
-.064	0	1.571
-.059	.115	1.487
-.047	.219	1.417
-.027	.325	1.346
+.003	.430	1.237
.015	.463	1.181
.027	.497	1.104
.038	.520	1.099
.049	.541	1.053
.059	.557	.983
.074	.577	.917
.087	.594	.867
.098	.606	.832
.107	.616	.807
.120	.629	.773
.133	.641	.744
.151	.658	.706
.176	.678	.663
.224	.713	.600
.310	.767	.521
.477	.853	.430
.748	.964	.349
1.010	1.053	.305

TABLE 4. PRESSURE AT BODY SURFACE

x/D	r/D	PRESSURE (PSF)
0	0	1735
.004	.100	1690
.016	.200	1640
.036	.300	1600
.064	.400	1495
.075	.432	1400
.087	.464	1140
.092	.474	750
.093	.475	740
.094	.476	716
.095	.478	656
.096	.479	616
.098	.481	567
.099	.483	514
.102	.486	440
.107	.489	356
.112	.493	269
.118	.495	205
.124	.497	177
.140	.500	26
remainder of body		~ 26

TABLE 5. FIRE FLOW FIELD - CONDITIONS AT STAGNATION POINT

P	=	1735.	lb/ft ²
T	=	20114.	°R
ρ	=	.2338 x 10 ⁻⁴	slugs/ft ³
concentrations:			
e ⁻	=	4.0 x 10 ¹⁶	electrons/cc
O ₂	=	3.0 x 10 ¹¹	particles/cc
N ₂	=	2.0 x 10 ¹⁴	particles/cc
NO	=	8.0 x 10 ¹²	particles/cc
O	=	9.5 x 10 ¹⁷	particles/cc
N	=	3.0 x 10 ¹⁷	particles/cc
O ⁺	=	5.5 x 10 ¹⁵	particles/cc
N ⁺	=	3.0 x 10 ¹⁶	particles/cc
O ⁻	=	2.5 x 10 ¹²	particles/cc

TABLE 6. LAMINAR CONVECTIVE HEAT FLUXES

x (in.)	\dot{q}_L (BTU/sec.-ft ²) for			
	$T_w = 0^\circ\text{R}$	$T_w = 1000^\circ\text{R}$	$T_w = 2000^\circ\text{R}$	$T_w = 2800^\circ\text{R}$
0	654	645	635	626
.7	605	598	588	580
1.0	590	582	572	565
1.2	592	584	575	567
1.4	590	583	573	565
1.6	588	581	571	564
1.8	610	602	593	584
2.0	643	634	624	615
2.1	647	628	620	510
2.15	645	637	627	618
2.20	641	630	620	610
2.4	500	494	485	480
2.8	269	265	260	257
3.0	207	204	200	198
5	24.2	23.9	23.7	23.5
8	9.1	9.0	8.9	8.8
12	6.5	6.4	6.3	6.2
16	5.3	5.2	5.2	5.1
20	4.6	4.6	4.5	4.5
21	4.4	4.4	4.3	4.3
21.28	4.0	4.0	3.9	3.9

TABLE 7. TURBULENT CONVECTIVE HEAT FLUXES

x (in.)	\dot{q}_T (BTU/sec.-ft. ²) for			
	Tw = 0°R	Tw = 1000°R	Tw = 2000°R	Tw = 2800°R
0	0	0	0	0
.7	642	630	615	606
1.0	687	677	663	652
1.2	720	710	696	684
1.4	748	736	722	710
1.6	772	760	745	733
1.8	828	816	800	787
2.0	906	892	874	860
2.1	930	920	906	892
2.15	936	922	907	896
2.20	942	926	910	900
2.4	771	758	743	731
2.8	437	430	421	414
3.0	343	337	330	325
5	34.2	33.9	33.5	33.3
8	23.0	23.0	22.7	22.5
12	20.5	20.3	20.1	19.9
16	19.2	19.0	18.8	18.6
20	18.6	18.4	18.2	18.1
21	18.2	18.0	17.8	17.7
21.28	17.5	17.4	17.2	17.1

x (in)	Reynolds Number (Re _s)
0	0
.7	9,972
1.0	13,277
1.2	15,748
1.4	18,164
1.6	20,574
1.8	24,120
2.0	28,879
2.1	31,053
2.15	31,978
2.20	33,284
2.4	31,446
2.8	22,125
3.0	18,946

TABLE 8. RADIATIVE HEAT FLUXES

x (in.)	ABSORBED ($\alpha \dot{q}_{HG}$) (BTU/sec.-ft. ²)		INCIDENT (\dot{q}_{HG}) (BTU/sec.-ft. ²)	
	.16 - 10 μ	.05 - 10 μ	.16 - 10 μ	.05 - 10 μ
0	173	875	320	1,100
.25	157.5		290	
.65	139	625.5	256	797
1.10	122.5	520.5	225	668
1.50	107		197	
2.00	74.3	334	137	425
2.15	56		103	
2.48	21.5	79.7	39.3	104
3.40	3.6	11.6	6.1	15
10.00	.13		.198	

TABLE 9. RE-RADIATIVE HEAT FLUXES

T_w (°R)	\dot{q}_{rr} (BTU/sec.-ft ²)
0	0
1000	.29
2000	4.57
2800	17.56

TABLE 10. SPECTRAL STERADIANCY N⁺ DEIONIZATION

λ (μ)	(Watts/Ster.-CC- μ)	λ (μ)	(Watts/Ster.-CC- μ)	λ (μ)	(Watts/Ster.-CC- μ)
.0570	1.51×10^{-2}	.0791	$2.49 \times 10^{+2}$.2036	3.20
.0573	2.28×10^{-2}	.0797	$2.75 \times 10^{+2}$.2105	4.40
.0577	2.94×10^{-2}	.0804	$3.03 \times 10^{+2}$.2179	6.02
.0580	3.72×10^{-2}	.0810	$3.32 \times 10^{+2}$.2252	8.05
.0583	4.63×10^{-2}	.0817	$3.64 \times 10^{+2}$.2315	$1.01 \times 10^{+1}$
.0587	5.69×10^{-2}	.0824	$3.98 \times 10^{+2}$.2375	$1.25 \times 10^{+1}$
.0590	6.93×10^{-2}	.0831	$4.36 \times 10^{+2}$.2433	$1.51 \times 10^{+1}$
.0594	8.35×10^{-2}	.0838	$4.76 \times 10^{+2}$.2481	$1.75 \times 10^{+1}$
.0597	1.03×10^{-1}	.0845	$5.21 \times 10^{+2}$.2545	$2.11 \times 10^{+1}$
.0601	1.225×10^{-1}	.0852	$5.69 \times 10^{+2}$.2801	$4.02 \times 10^{+1}$
.0605	1.37×10^{-1}	.0855	$1.27 \times 10^{+2}$.2933	$5.29 \times 10^{+1}$
.0608	1.58×10^{-1}	.0862	$1.41 \times 10^{+2}$.2941	$2.50 \times 10^{+1}$
.0612	1.87×10^{-1}	.0870	$1.73 \times 10^{+2}$.3021	$2.88 \times 10^{+1}$
.0616	2.31×10^{-1}	.0877	$2.11 \times 10^{+2}$.3030	$2.675 \times 10^{+1}$
.0620	2.835×10^{-1}	.0885	$2.56 \times 10^{+2}$.3205	$3.505 \times 10^{+1}$
.0623	3.74×10^{-1}	.0893	$3.105 \times 10^{+2}$.3215	$2.63 \times 10^{+1}$
.0627	4.80×10^{-1}	.0901	$3.77 \times 10^{+2}$.3425	$3.42 \times 10^{+1}$
.0631	6.04×10^{-1}	.0909	$4.51 \times 10^{+2}$.3436	$1.27 \times 10^{+1}$
.0635	8.30×10^{-1}	.0917	$5.41 \times 10^{+2}$.3663	$1.80 \times 10^{+1}$
.0639	1.14	.0926	$6.45 \times 10^{+2}$.4098	$3.03 \times 10^{+1}$
.0644	1.45	.0935	$7.66 \times 10^{+2}$.4202	$3.35 \times 10^{+1}$
.0648	1.81	.0943	$9.045 \times 10^{+2}$.4219	$3.15 \times 10^{+1}$
.0652	2.28	.0952	$1.06 \times 10^{+3}$.4425	$3.76 \times 10^{+1}$
.0656	2.88	.0962	$1.24 \times 10^{+3}$.4444	$1.83 \times 10^{+1}$
.0661	3.51	.0971	$1.435 \times 10^{+3}$.4566	$2.01 \times 10^{+1}$
.0665	4.38	.0980	$1.65 \times 10^{+3}$.4587	$1.015 \times 10^{+1}$
.0669	5.45	.0990	$1.89 \times 10^{+3}$.4854	$1.22 \times 10^{+1}$
.0674	6.75	.1000	$2.14 \times 10^{+3}$.4878	4.09
.0678	8.33	.1010	$2.41 \times 10^{+3}$.5102	4.80
.0683	$1.03 \times 10^{+1}$.1020	$3.60 \times 10^{+2}$.5128	1.86
.0688	$1.26 \times 10^{+1}$.1031	$4.40 \times 10^{+2}$.5714	3.04
.0693	$1.55 \times 10^{+1}$.1042	$5.37 \times 10^{+2}$.6579	5.04
.0697	$1.89 \times 10^{+1}$.1053	$6.53 \times 10^{+2}$.7299	6.73
.0702	$2.30 \times 10^{+1}$.1064	$7.94 \times 10^{+2}$.7353	6.17
.0707	$2.78 \times 10^{+1}$.1070	$8.74 \times 10^{+2}$.7576	6.58
.0712	$3.36 \times 10^{+1}$.1081	$1.06 \times 10^{+3}$.7634	6.40
.0717	$4.03 \times 10^{+1}$.1093	$1.28 \times 10^{+3}$.7692	6.50
.0723	$4.83 \times 10^{+1}$.1105	$1.54 \times 10^{+3}$.7752	6.10
.0728	$5.75 \times 10^{+1}$.1117	$1.845 \times 10^{+3}$.7874	6.28
.0733	$6.80 \times 10^{+1}$.1130	$2.21 \times 10^{+3}$.7937	4.26
.0739	$7.98 \times 10^{+1}$.1135	0	.8000	4.32
.0744	$9.30 \times 10^{+1}$.1675	3.70×10^{-1}	.8065	2.53

TABLE 10. SPECTRAL STERADIANCEY N⁺ DEIONIZATION (Cont.)

λ (μ)	(Watts/Ster.-CC- μ)	λ (μ)	(Watts/Ster.-CC- μ)	λ (μ)	(Watts/Ster.-CC- μ)
.0750	$1.08 \times 10^{+2}$.1733	4.20×10^{-1}	.8130	1.22
.0755	$1.24 \times 10^{+2}$.1733	5.60×10^{-1}	.9174	1.69
.0761	$1.42 \times 10^{+2}$.1757	6.60×10^{-1}	.9259	1.61
.0767	$1.61 \times 10^{+2}$.1802	8.80×10^{-1}	.9434	1.67
.0773	$1.81 \times 10^{+2}$.1825	1.015	.9524	6.79×10^{-1}
.0779	$2.02 \times 10^{+2}$.1897	1.555	.9615	6.92×10^{-1}
.0785	$2.25 \times 10^{+2}$.1953	2.10	.9709	1.42×10^{-1}
				1.010	1.52×10^{-1}

TABLE 11. SPECTRAL STERADIANCY O⁺ DEIONIZATION

λ (μ)	(Watts/Ster.-CC- μ)	λ (μ)	(Watts/Ster.-CC- μ)	λ (μ)	(Watts/Ster.-CC- μ)
.0587	3.60×10^{-4}	.0824	$2.41 \times 10^{+2}$.1650	$.350 \times 10^{-1}$
.0590	1.99×10^{-3}	.0831	$2.84 \times 10^{+2}$.1779	1.03×10^{-1}
.0594	4.41×10^{-3}	.0838	$3.33 \times 10^{+2}$.2160	1.01
.0597	7.31×10^{-3}	.0845	$3.88 \times 10^{+2}$.2309	1.95
.0601	1.40×10^{-2}	.0852	$4.49 \times 10^{+2}$.2770	$.846 \times 10^{-1}$
.0605	$.179 \times 10^{-2}$.0855	$4.76 \times 10^{+2}$.2778	2.57
.0608	2.305×10^{-2}	.0862	$5.45 \times 10^{+2}$.2817	2.84
.0612	2.90×10^{-2}	.0870	$6.20 \times 10^{+2}$.2825	2.40
.0616	4.02×10^{-2}	.0877	$7.06 \times 10^{+2}$.2941	$.315 \times 10^{-1}$
.0620	4.89×10^{-2}	.0885	$7.83 \times 10^{+2}$.2950	$.307 \times 10^{-1}$
.0623	5.89×10^{-2}	.0893	$8.72 \times 10^{+2}$.3021	$.359 \times 10^{-1}$
.0627	7.045×10^{-4}	.0901	$9.65 \times 10^{+2}$.3030	1.32
.0631	8.38×10^{-2}	.0909	$1.06 \times 10^{+3}$.3704	$.454 \times 10^{-1}$
.0635	$/106 \times 10^{-1}$.0917	$4.72 \times 10^{+1}$.4274	$.858 \times 10^{-1}$
.0639	1.31×10^{-1}	.0926	$5.84 \times 10^{+1}$.4292	$.852 \times 10^{-1}$
.0644	1.77×10^{-1}	.0935	$7.21 \times 10^{+1}$.4310	2.28
.0648	2.13×10^{-1}	.0943	$8.89 \times 10^{+1}$.4348	2.35
.0652	2.735×10^{-1}	.0952	$1.095 \times 10^{+2}$.4367	2.14
.0656	3.445×10^{-1}	.0962	$1.35 \times 10^{+2}$.4405	2.21
.0661	4.27×10^{-1}	.0971	$1.66 \times 10^{+2}$.4425	2.17
.0665	5.485×10^{-1}	.0980	$2.04 \times 10^{+2}$.4695	2.66
.0669	6.90×10^{-1}	.0990	$2.50 \times 10^{+2}$.4717	2.28×10^{-1}
.0674	8.85×10^{-1}	.1000	$3.06 \times 10^{+2}$.4975	.300
.0678	1.11	.1010	$3.74 \times 10^{+2}$.5000	2.76×10^{-1}
.0683	1.38	.1020	$4.57 \times 10^{+2}$.5076	.298
.0688	1.72	.1031	$5.57 \times 10^{+2}$.5917	.590
.0693	2.17	.1042	$6.77 \times 10^{+2}$.6944	1.02
.0697	2.68	.1053	$8.22 \times 10^{+2}$.6993	.907
.0702	3.33	.1064	$9.94 \times 10^{+2}$.7299	1.01
.0707	4.25	.1070	2.29	.7353	.969
.0712	5.19	.1081	2.81	.8000	1.157
.0717	6.48	.1093	3.46	.8065	.789
.0723	8.04	.1105	4.24	.8130	.426
.0728	9.99	.1117	5.21	.9259	.601
.0733	$1.24 \times 10^{+1}$.1130	6.39	.9346	.302
.0739	$1.55 \times 10^{+1}$.1135	6.93	.9804	.333
.0744	$1.90 \times 10^{+1}$.1148	8.50	.9901	1.94×10^{-1}
.0750	$2.36 \times 10^{+1}$.1161	$1.04 \times 10^{+1}$	1.2821	2.67×10^{-1}
.0755	$2.91 \times 10^{+1}$.1175	$1.27 \times 10^{+1}$	1.2987	2.54×10^{-1}
.0761	$3.58 \times 10^{+1}$.1189	$1.56 \times 10^{+1}$	1.3333	2.57×10^{-1}
.0767	$4.40 \times 10^{+1}$.1203	$1.90 \times 10^{+1}$	1.4286	2.51×10^{-1}

TABLE 11. SPECTRAL STERADIANCY O⁺ DEIONIZATION (Cont.)

λ (μ)	(Watts/Ster.-CC- μ)	λ (μ)	(Watts/Ster.-CC- μ)	λ (μ)	(Watts/Ster.-CC- μ)
.0773	$5.39 \times 10^{+1}$.1218	$2.32 \times 10^{+1}$	1.4493	$.359 \times 10^{-1}$
.0779	$6.59 \times 10^{+1}$.1233	$2.835 \times 10^{+1}$	1.6393	$.345 \times 10^{-1}$
.0785	$8.02 \times 10^{+1}$.1248	$3.46 \times 10^{+1}$	1.7241	2.00×10^{-2}
.0791	$9.74 \times 10^{+1}$.1264	$4.21 \times 10^{+1}$	1.8182	1.92×10^{-2}
.0797	$1.18 \times 10^{+2}$.1280	$5.13 \times 10^{+1}$	2.0000	1.74×10^{-2}
.0804	$1.42 \times 10^{+2}$.1297	$6.235 \times 10^{+1}$	2.2222	1.09×10^{-2}
.0810	$1.70 \times 10^{+2}$.1314	$7.58 \times 10^{+1}$		
.0817	$2.03 \times 10^{+2}$.1616	2.50×10^{-2}		

TABLE 12. SPECTRAL STERADIANCY

 $(N^+ + O^+)$ FREE - FREE

$\lambda (\mu)$	(Watts/Ster.-CC- μ)	$\lambda (\mu)$	(Watts/Ster.-CC- μ)
.20	5.76×10^{-2}	.787	6.09×10^{-1}
.202	5.99×10^{-2}	.855	6.09×10^{-1}
.216	8.05×10^{-2}	.962	6.01×10^{-1}
.229	1.01×10^{-1}	1.56	5.04×10^{-1}
.283	2.00×10^{-1}	2.27	4.00×10^{-1}
.338	2.99×10^{-1}	4.17	2.50×10^{-1}
.402	3.99×10^{-1}	5.26	2.04×10^{-1}
.490	4.99×10^{-1}	7.14	1.53×10^{-1}
.658	5.90×10^{-1}	10.0	1.08×10^{-1}

TABLE 13. SPECTRAL STERADIANCY 0^- FREE-BOUND

λ (μ)	(Watts/Ster. -CC- μ)	λ (μ)	(Watts/Ster. -CC- μ)	λ (μ)	(Watts/Ster. -CC- μ)
.1637	0	.2083	2.619×10^{-1}	.2740	4.251×10^{-1}
.1639	1.248×10^{-1}	.2105	2.697×10^{-1}	.2755	4.246×10^{-1}
.1653	1.300×10^{-1}	.2128	2.766×10^{-1}	.2778	4.307×10^{-1}
.1667	1.337×10^{-1}	.2151	2.835×10^{-1}	.2786	4.284×10^{-1}
.1672	1.377×10^{-1}	.2155	2.868×10^{-1}	.2825	4.383×10^{-1}
.1675	1.367×10^{-1}	.2160	2.857×10^{-1}	.2833	4.379×10^{-1}
.1678	1.374×10^{-1}	.2174	2.912×10^{-1}	.2849	4.419×10^{-1}
.1695	1.429×10^{-1}	.2198	2.989×10^{-1}	.2865	4.438×10^{-1}
.1709	1.463×10^{-1}	.2222	3.030×10^{-1}	.2874	4.433×10^{-1}
.1724	1.525×10^{-1}	.2247	3.124×10^{-1}	.2950	4.600×10^{-1}
.1739	1.584×10^{-1}	.2273	3.227×10^{-1}	.3030	4.728×10^{-1}
.1742	1.579×10^{-1}	.2299	3.301×10^{-1}	.3135	4.920×10^{-1}
.1745	1.585×10^{-1}	.2315	3.336×10^{-1}	.3226	5.057×10^{-1}
.1754	1.625×10^{-1}	.2320	3.322×10^{-1}	.3247	5.09×10^{-1}
.1770	1.660×10^{-1}	.2353	3.427×10^{-1}	.3268	5.09×10^{-1}
.1786	1.714×10^{-1}	.2358	3.460×10^{-1}	.3333	5.166×10^{-1}
.1802	1.750×10^{-1}	.2364	3.455×10^{-1}	.3344	5.157×10^{-1}
.1818	1.813×10^{-1}	.2381	3.526×10^{-1}	.3413	5.218×10^{-1}
.1835	1.856×10^{-1}	.2387	3.521×10^{-1}	.3448	5.202×10^{-1}
.1852	1.920×10^{-1}	.2392	3.534×10^{-1}	.3484	5.26×10^{-1}
.1869	1.992×10^{-1}	.2410	3.614×10^{-1}	.3559	5.26×10^{-1}
.1887	2.037×10^{-1}	.2439	3.681×10^{-1}	.3597	5.297×10^{-1}
.1905	2.089×10^{-1}	.2469	3.765×10^{-1}	.3650	5.269×10^{-1}
.1923	2.149×10^{-1}	.2500	3.808×10^{-1}	.3663	5.31×10^{-1}
.1942	2.178×10^{-1}	.2532	3.868×10^{-1}	.3876	5.31×10^{-1}
.1961	2.223×10^{-1}	.2564	3.935×10^{-1}	.4237	4.998×10^{-1}
.1980	2.275×10^{-1}	.2591	4.008×10^{-1}	.4425	4.779×10^{-1}
.2000	2.359×10^{-1}	.2597	3.989×10^{-1}	.4630	4.499×10^{-1}
.2020	2.428×10^{-1}	.2632	4.070×10^{-1}	.4831	4.220×10^{-1}
.2041	2.505×10^{-1}	.2667	4.137×10^{-1}	.5051	3.192×10^{-1}
.2062	2.550×10^{-1}	.2695	4.114×10^{-1}	.5076	3.862×10^{-1}
.2066	2.574×10^{-1}	.2703	4.162×10^{-1}	.5291	3.549×10^{-1}
.2070	2.564×10^{-1}	.2717	4.159×10^{-1}	.5556	3.179×10^{-1}
				.5882	2.748×10^{-1}
				.6250	2.295×10^{-1}
				.6667	1.862×10^{-1}
				.6993	1.555×10^{-1}
				.7407	1.195×10^{-1}
				.7634	1.001×10^{-1}
				.7937	7.761×10^{-2}
				.8197	5.513×10^{-2}
				.8475	2.371×10^{-2}
				.8547	0

TABLE 14. SPECTRAL STERADIANCY N₂ 1ST. POSITIVE

λ (μ)	(Watts/Ster.-CC- μ)	λ (μ)	(Watts/Ster.-CC- μ)	λ (μ)	(Watts/Ster.-CC- μ)
.5128	0	.7634	3.462×10^{-3}	1.4286	1.792×10^{-4}
.5155	4.184×10^{-4}	.7692	3.827×10^{-3}	1.4493	1.705×10^{-4}
.5208	4.088×10^{-4}	.7752	2.302×10^{-3}	1.4706	1.800×10^{-4}
.5236	8.079×10^{-4}	.7874	2.749×10^{-3}	1.4925	8.546×10^{-5}
.5263	1.197×10^{-3}	.7937	2.417×10^{-3}	1.5152	9.730×10^{-5}
.5291	1.183×10^{-3}	.8000	2.623×10^{-3}	1.5385	9.222×10^{-5}
.5348	2.309×10^{-3}	.8065	2.305×10^{-3}	1.5625	1.019×10^{-4}
.5405	1.501×10^{-3}	.8130	2.500×10^{-3}	1.5873	8.260×10^{-5}
.5435	1.852×10^{-3}	.8197	2.439×10^{-3}	1.6129	7.806×10^{-5}
.5464	1.463×10^{-3}	.8403	2.942×10^{-3}	1.6393	8.597×10^{-5}
.5495	1.805×10^{-3}	.8696	3.671×10^{-3}	1.6667	5.790×10^{-5}
.5525	1.782×10^{-3}	.8772	2.978×10^{-3}	1.6949	6.545×10^{-5}
.5587	2.429×10^{-3}	.8850	3.092×10^{-3}	1.7544	5.786×10^{-5}
.5650	3.714×10^{-3}	.8929	1.410×10^{-3}	1.8182	2.545×10^{-5}
.5714	5.255×10^{-3}	.9174	1.728×10^{-3}	1.8519	3.176×10^{-5}
.5747	4.857×10^{-3}	.9259	1.679×10^{-3}	1.8868	1.485×10^{-5}
.5780	5.747×10^{-3}	.9346	1.793×10^{-3}	1.9231	1.386×10^{-5}
.5814	4.721×10^{-3}	.9434	1.662×10^{-3}	1.9608	6.458×10^{-6}
.5848	3.722×10^{-3}	.9615	1.863×10^{-3}	2.0408	5.583×10^{-6}
.5882	4.585×10^{-3}	.9709	1.590×10^{-3}	2.0833	1.036×10^{-5}
.5952	3.264×10^{-3}	.9901	1.697×10^{-3}	2.1277	0
.5988	3.799×10^{-3}	1.000	1.513×10^{-3}		
.6024	3.454×10^{-3}	1.0101	1.592×10^{-3}		
.6061	4.251×10^{-3}	1.0204	1.541×10^{-3}		
.6098	4.185×10^{-3}	1.0309	1.669×10^{-3}		
.6173	5.136×10^{-3}	1.0417	1.557×10^{-3}		
.6289	7.209×10^{-3}	1.0526	7.244×10^{-4}		
.6329	5.318×10^{-3}	1.0638	7.537×10^{-4}		
.6369	6.226×10^{-3}	1.0753	6.238×10^{-4}		
.6410	5.876×10^{-3}	1.0870	6.523×10^{-4}		
.6452	6.499×10^{-3}	1.0989	7.261×10^{-4}		
.6536	4.650×10^{-3}	1.1111	7.002×10^{-4}		
.6579	5.482×10^{-3}	1.1236	6.748×10^{-4}		
.6623	4.263×10^{-3}	1.1494	7.510×10^{-4}		
.6667	4.628×10^{-3}	1.1628	7.226×10^{-4}		
.6711	3.462×10^{-3}	1.1765	7.336×10^{-4}		
.6757	3.612×10^{-3}	1.2048	6.060×10^{-4}		
.6803	2.920×10^{-3}	1.2195	6.502×10^{-4}		
.6897	2.811×10^{-3}	1.2346	2.298×10^{-4}		
.7042	3.600×10^{-3}	1.2658	2.715×10^{-4}		
.7194	4.817×10^{-3}	1.2821	2.600×10^{-4}		
.7353	5.869×10^{-3}	1.2987	2.765×10^{-4}		
.7407	5.418×10^{-3}	1.3158	2.644×10^{-4}		
.7463	5.946×10^{-3}	1.3514	2.895×10^{-4}		
.7519	4.875×10^{-3}	1.3699	2.533×10^{-4}		
.7576	5.232×10^{-3}	1.4085	2.719×10^{-4}		

TABLE 15. SPECTRAL STERADIANCY N₂ 2ND POSITIVE

λ (μ)	(WATTS/STER. -CC- μ)	λ (μ)	(WATTS/STER. -CC- μ)
.2604	0	.3534	1.376×10^{-1}
.2611	9.805×10^{-4}	.3546	1.013×10^{-1}
.2639	9.807×10^{-4}	.3571	1.230×10^{-1}
.2646	1.961×10^{-3}	.3584	4.161×10^{-2}
.2660	1.961×10^{-3}	.3623	5.367×10^{-2}
.2667	2.941×10^{-3}	.3663	6.536×10^{-2}
.2688	4.899×10^{-3}	.3676	6.039×10^{-2}
.2710	7.831×10^{-3}	.3704	7.129×10^{-2}
.2725	1.076×10^{-2}	.3717	5.568×10^{-2}
.2747	1.660×10^{-2}	.3745	6.567×10^{-2}
.2770	2.730×10^{-2}	.3759	4.130×10^{-2}
.2793	4.378×10^{-2}	.3802	5.246×10^{-2}
.2801	2.819×10^{-2}	.3817	2.939×10^{-2}
.2817	3.785×10^{-2}	.3831	3.215×10^{-2}
.2825	3.491×10^{-2}	.3846	2.834×10^{-2}
.2849	5.318×10^{-2}	.3876	3.304×10^{-2}
.2874	8.096×10^{-2}	.3891	2.499×10^{-2}
.2899	1.239×10^{-1}	.3937	3.156×10^{-2}
.2933	2.168×10^{-1}	.3953	2.091×10^{-2}
.2941	1.412×10^{-1}	.3984	2.409×10^{-2}
.2950	1.619×10^{-1}	.4000	1.436×10^{-2}
.2959	8.559×10^{-2}	.4049	1.811×10^{-2}
.2967	9.779×10^{-2}	.4065	1.333×10^{-2}
.2976	4.645×10^{-2}	.4082	9.266×10^{-3}
.3003	6.696×10^{-2}	.4115	1.110×10^{-3}
.3021	8.646×10^{-2}	.4132	7.780×10^{-3}
.3040	1.105×10^{-1}	.4184	9.520×10^{-3}
.3077	1.811×10^{-1}	.4202	5.040×10^{-3}
.3106	2.445×10^{-1}	.4255	6.778×10^{-3}
.3115	2.219×10^{-1}	.4274	4.280×10^{-3}
.3125	2.507×10^{-1}	.4292	4.248×10^{-3}
.3135	1.631×10^{-1}	.4310	4.817×10^{-3}
.3155	2.079×10^{-2}	.4329	4.779×10^{-3}
.3165	4.912×10^{-2}	.4348	2.371×10^{-3}
.3195	6.769×10^{-2}	.4386	2.333×10^{-3}
.3226	9.399×10^{-1}	.4405	1.157×10^{-3}
.3247	1.166×10^{-2}	.4425	1.147×10^{-3}
.3257	9.762×10^{-1}	.4444	1.707×10^{-3}
.3289	1.345×10^{-1}	.4484	1.678×10^{-4}
.3300	1.219×10^{-1}	.4505	5.545×10^{-4}
.3333	1.571×10^{-1}	.4545	5.449×10^{-3}
.3367	2.088×10^{-1}	.4566	1.080×10^{-3}

TABLE 15. SPECTRAL STERADIANCY N₂ 2ND POSITIVE (Cont.)

λ (μ)	(WATTS/STER. -CC- μ)	λ (μ)	(WATTS/STER. -CC- μ)
.3378	4.624×10^{-2}	.4587	0
.3413	6.099×10^{-2}	.4651	0
.3460	8.678×10^{-2}	.4673	5.158×10^{-4}
.3497	1.154×10^{-1}	.4695	5.110×10^{-4}
.3509	1.133×10^{-1}	.4717	0

TABLE 16. SPECTRAL STERADIANCY $N_2^+ 1$ ST. NEGATIVE

λ (μ)	(Watts/Ster. -CC- μ)	λ (μ)	(Watts/Ster. -CC- μ)
.2857	1.256×10^{-2}	.4348	3.497×10^{-2}
.2882	1.925×10^{-2}	.4405	7.057×10^{-2}
.2915	3.161×10^{-2}	.4444	1.126×10^{-1}
.2950	5.429×10^{-2}	.4545	3.602×10^{-1}
.2985	9.085×10^{-2}	.4587	5.727×10^{-1}
.3021	1.513×10^{-1}	.4608	1.490×10^{-1}
.3067	2.885×10^{-1}	.4695	2.923×10^{-1}
.3077	1.811×10^{-1}	.4717	5.061×10^{-4}
.3135	4.096×10^{-1}	.4739	5.012×10^{-4}
.3175	7.031×10^{-1}	.4762	9.927×10^{-4}
.3205	1.055	.4785	1.474×10^{-3}
.3236	1.582	.4854	3.338×10^{-3}
.3289	3.104	.4902	6.072×10^{-3}
.3300	9.187×10^{-1}	.4950	1.052×10^{-2}
.3311	4.465×10^{-1}	.5025	2.523×10^{-2}
.3333	5.999×10^{-1}	.5076	4.460×10^{-2}
.3356	8.080×10^{-1}	.5128	7.873×10^{-2}
.3378	1.086	.5155	1.046×10^{-1}
.3436	2.276	.5181	3.267×10^{-2}
.3484	4.110	.5236	5.696×10^{-2}
.3546	8.592	.5263	0
.3571	3.436	.5405	0
.3584	2.440×10^{-1}	.5435	3.705×10^{-4}
.3650	5.559×10^{-1}	.5464	3.658×10^{-4}
.3704	1.074	.5495	7.221×10^{-4}
.3788	2.874	.5525	1.069×10^{-3}
.3831	4.698	.5618	3.423×10^{-3}
.3906	7.517	.5682	6.994×10^{-3}
.3922	8.397×10^{-2}	.5714	1.051×10^{-2}
.3937	1.024×10^{-1}	.5747	1.522×10^{-2}
.4000	2.209×10^{-1}	.5780	2.235×10^{-3}
.4082	5.765×10^{-1}	.5848	4.963×10^{-3}
.4115	8.448×10^{-1}	.5882	0
.4167	1.500	.6494	0
.4237	3.061	.6536	2.325×10^{-4}
.4255	1.622	.6579	4.568×10^{-4}
.4274	1.959	.6623	8.975×10^{-4}
.4292	1.699×10^{-2}	.6667	1.763×10^{-3}

TABLE 17. SPECTRAL STERADIANCY 0^2 SCHUMANN-RUNGE

λ (μ)	(Watts/Ster.-CC- μ)	λ (μ)	(Watts/Ster.-CC- μ)	λ (μ)	(Watts/Ster.-CC- μ)
.2618	0	.2857	1.352×10^{-2}	.3145	1.280×10^{-2}
.2625	4.903×10^{-3}	.2865	1.254×10^{-2}	.3155	1.277×10^{-2}
.2632	4.903×10^{-3}	.2874	1.638×10^{-2}	.3165	1.182×10^{-2}
.2639	3.923×10^{-3}	.2882	1.540×10^{-2}	.3175	1.452×10^{-2}
.2646	3.923×10^{-3}	.2890	1.538×10^{-2}	.3185	1.448×10^{-2}
.2653	3.922×10^{-3}	.2899	1.440×10^{-2}	.3195	1.354×10^{-2}
.2660	3.922×10^{-3}	.2907	1.439×10^{-2}	.3205	1.350×10^{-2}
.2667	8.823×10^{-3}	.2915	1.341×10^{-2}	.3215	1.257×10^{-2}
.2674	8.822×10^{-3}	.2924	1.339×10^{-2}	.3226	1.253×10^{-2}
.2681	8.820×10^{-3}	.2933	1.624×10^{-2}	.3236	1.160×10^{-2}
.2688	7.838×10^{-3}	.2941	1.621×10^{-2}	.3247	1.424×10^{-2}
.2695	7.836×10^{-3}	.2950	1.524×10^{-2}	.3257	1.331×10^{-2}
.2703	7.834×10^{-3}	.2959	1.426×10^{-2}	.3268	1.327×10^{-2}
.2710	7.831×10^{-3}	.2967	1.424×10^{-2}	.3279	1.235×10^{-2}
.2717	1.272×10^{-2}	.2976	1.327×10^{-2}	.3289	1.231×10^{-2}
.2725	1.272×10^{-2}	.2985	1.420×10^{-2}	.3300	1.227×10^{-2}
.2732	1.173×10^{-2}	.2994	1.512×10^{-2}	.3311	1.223×10^{-2}
.2740	1.173×10^{-2}	.3003	1.509×10^{-2}	.3322	1.219×10^{-2}
.2747	1.074×10^{-2}	.3012	1.412×10^{-2}	.3333	1.129×10^{-2}
.2755	1.074×10^{-2}	.3021	1.410×10^{-2}	.3344	1.125×10^{-2}
.2762	1.073×10^{-2}	.3030	1.313×10^{-2}	.3356	1.035×10^{-2}
.2770	1.462×10^{-2}	.3040	1.311×10^{-2}	.3367	1.117×10^{-2}
.2778	1.462×10^{-2}	.3049	1.588×10^{-2}	.3378	1.285×10^{-2}
.2786	1.363×10^{-2}	.3058	1.585×10^{-2}	.3390	1.280×10^{-2}
.2793	1.362×10^{-2}	.3067	1.489×10^{-2}	.3401	1.190×10^{-2}
.2801	1.264×10^{-2}	.3077	1.393×10^{-2}	.3413	1.186×10^{-2}
.2809	1.263×10^{-2}	.3086	1.390×10^{-2}	.3425	1.097×10^{-2}
.2817	1.553×10^{-2}	.3096	1.295×10^{-2}	.3436	1.093×10^{-2}
.2825	1.552×10^{-2}	.3106	1.292×10^{-2}	.3448	1.089×10^{-2}
.2833	1.453×10^{-2}	.3115	1.473×10^{-2}	.3460	1.085×10^{-2}
.2841	1.452×10^{-2}	.3125	1.469×10^{-2}	.3472	9.973×10^{-3}
.2849	1.354×10^{-3}	.3135	1.374×10^{-3}	.3484	9.934×10^{-3}
.3497	9.069×10^{-3}	.3922	6.350×10^{-3}	.4464	2.821×10^{-3}
.3509	9.032×10^{-3}	.3937	5.611×10^{-3}	.4484	2.797×10^{-3}
.3521	9.812×10^{-3}	.3953	6.273×10^{-3}	.4505	2.773×10^{-3}
.3534	1.140×10^{-2}	.3968	5.542×10^{-3}	.4525	2.199×10^{-3}
.3546	1.054×10^{-2}	.3984	5.507×10^{-3}	.4545	2.180×10^{-3}
.3559	1.049×10^{-3}	.400	5.472×10^{-3}	.4566	2.160×10^{-3}
.3571	9.644×10^{-3}	.4016	4.757×10^{-3}	.4587	2.141×10^{-3}
.3584	9.601×10^{-3}	.4032	4.726×10^{-3}	.4608	2.122×10^{-3}
.3597	9.558×10^{-3}	.4049	5.366×10^{-3}	.4630	2.102×10^{-3}
.3610	8.722×10^{-3}	.4065	4.664×10^{-3}	.4651	2.083×10^{-3}
.3623	8.681×10^{-3}	.4082	4.633×10^{-3}	.4673	2.063×10^{-3}

TABLE 17. SPECTRAL STERADIANCY 10^2 SCHUMANN-RUNGE (Cont.)

λ (μ)	(Watts/Ster.-CC- μ)	λ (μ)	(Watts/Ster.-CC- μ)	λ (μ)	(Watts/Ster.-CC- μ)
.3636	8.641×10^{-3}	.4098	4.602×10^{-3}	.4695	2.044×10^{-3}
.3650	7.818×10^{-3}	.4115	4.570×10^{-3}	.4717	2.024×10^{-3}
.3663	7.780×10^{-3}	.4132	5.187×10^{-3}	.4739	2.005×10^{-3}
.3676	7.743×10^{-3}	.4149	4.507×10^{-3}	.4762	1.489×10^{-3}
.3690	9.245×10^{-3}	.4167	4.475×10^{-3}	.4902	1.401×10^{-3}
.3704	8.433×10^{-3}	.4184	4.443×10^{-3}	.4926	1.849×10^{-3}
.3717	9.390×10^{-3}	.4202	3.780×10^{-3}	.4950	1.372×10^{-3}
.3731	8.347×10^{-3}	.4219	3.753×10^{-3}	.5051	1.313×10^{-3}
.3745	7.549×10^{-3}	.4237	3.725×10^{-3}	.5155	1.255×10^{-3}
.3759	7.509×10^{-3}	.4255	3.697×10^{-3}	.5181	8.272×10^{-4}
.3774	7.469×10^{-3}	.4274	3.669×10^{-3}	.5208	1.226×10^{-3}
.3788	7.429×10^{-3}	.4292	3.641×10^{-3}	.5236	1.212×10^{-3}
.3802	6.650×10^{-3}	.4310	3.011×10^{-3}	.5263	7.983×10^{-4}
.3817	6.613×10^{-3}	.4329	2.987×10^{-3}	.5405	7.505×10^{-4}
.3831	5.846×10^{-3}	.4348	3.556×10^{-3}	.5556	7.033×10^{-4}
.3846	5.813×10^{-3}	.4367	3.528×10^{-3}	.5650	6.753×10^{-4}
.3861	7.224×10^{-3}	.4386	2.916×10^{-3}	.5682	3.330×10^{-4}
.3876	6.464×10^{-3}	.4405	2.892×10^{-3}	.5882	3.057×10^{-4}
.3891	6.427×10^{-3}	.4425	2.869×10^{-3}	.6173	2.703×10^{-4}
.3906	5.679×10^{-3}	.4444	2.845×10^{-3}	.6211	0

TABLE 18. SPECTRAL STERADIANCE NO GAMMA

λ (μ)	(Watts/Ster.-CC- μ)	λ (μ)	(Watts/Ster.-CC- μ)	λ (μ)	(Watts/Ster.-CC- μ)
.1669	0	.1818	4.281×10^{-2}	.2033	2.368×10^{-1}
.1672	5.421×10^{-4}	.1825	5.192×10^{-2}	.2037	1.956×10^{-1}
.1681	5.498×10^{-4}	.1832	6.231×10^{-2}	.2045	2.331×10^{-1}
.1689	5.576×10^{-4}	.1838	7.740×10^{-2}	.2049	1.442×10^{-1}
.1692	1.120×10^{-3}	.1845	9.458×10^{-2}	.2053	5.154×10^{-2}
.1701	1.136×10^{-3}	.1852	1.155×10^{-1}	.2066	6.539×10^{-2}
.1704	1.712×10^{-3}	.1862	1.555×10^{-1}	.2079	8.368×10^{-2}
.1706	1.720×10^{-3}	.1866	1.194×10^{-1}	.2092	1.074×10^{-1}
.1709	2.303×10^{-3}	.1869	8.154×10^{-2}	.2105	1.374×10^{-1}
.1715	2.324×10^{-3}	.1873	8.967×10^{-2}	.2110	1.490×10^{-1}
.1718	2.918×10^{-3}	.1880	5.736×10^{-2}	.2114	1.485×10^{-1}
.1721	3.518×10^{-3}	.1887	6.934×10^{-2}	.2119	1.489×10^{-1}
.1724	3.534×10^{-3}	.1894	8.368×10^{-2}	.2123	1.614×10^{-1}
.1727	4.141×10^{-3}	.1901	1.004×10^{-1}	.2137	1.984×10^{-1}
.1730	4.754×10^{-3}	.1912	1.333×10^{-1}	.2146	2.327×10^{-1}
.1733	4.178×10^{-3}	.1923	1.767×10^{-1}	.2151	1.497×10^{-1}
.1736	4.196×10^{-3}	.1934	2.337×10^{-1}	.2155	6.265×10^{-2}
.1739	4.817×10^{-3}	.1942	2.810×10^{-1}	.2169	7.820×10^{-2}
.1742	4.838×10^{-3}	.1946	2.216×10^{-1}	.2183	9.840×10^{-2}
.1748	6.101×10^{-3}	.1949	1.580×10^{-1}	.2198	1.180×10^{-1}
.1754	8.000×10^{-3}	.1953	1.739×10^{-1}	.2212	1.404×10^{-1}
.1761	9.932×10^{-3}	.1957	1.220×10^{-1}	.2217	1.298×10^{-1}
.1767	1.190×10^{-2}	.1961	1.332×10^{-1}	.2222	1.392×10^{-1}
.1773	1.452×10^{-2}	.1965	7.304×10^{-2}	.2227	1.276×10^{-1}
.1779	1.783×10^{-2}	.1972	8.760×10^{-2}	.2237	1.483×10^{-1}
.1786	2.247×10^{-2}	.1980	1.039×10^{-1}	.2247	1.222×10^{-1}
.1792	2.719×10^{-2}	.1992	1.359×10^{-1}	.2262	1.543×10^{-1}
.1799	3.395×10^{-2}	.2004	1.765×10^{-1}	.2268	1.083×10^{-1}
.1805	2.830×10^{-2}	.2016	2.202×10^{-1}	.2273	6.119×10^{-2}
.1812	3.451×10^{-2}	.2028	2.761×10^{-1}	.2288	7.642×10^{-2}

TABLE 18. SPECTRAL STERADIANCY NO GAMMA (Cont.)

λ (μ)	(WATTS/STER. -CC- μ)	λ (μ)	(WATTS/STER. -CC- μ)
.2304	9.460×10^{-2}	.2667	8.725×10^{-2}
.2309	1.013×10^{-1}	.2681	6.174×10^{-2}
.2320	9.316×10^{-2}	.2710	7.733×10^{-2}
.2336	1.144×10^{-1}	.2725	5.086×10^{-2}
.2353	1.414×10^{-1}	.2755	6.345×10^{-2}
.2358	1.511×10^{-1}	.2778	4.872×10^{-2}
.2364	9.995×10^{-2}	.2801	5.639×10^{-2}
.2370	1.077×10^{-1}	.2817	3.494×10^{-2}
.2375	4.963×10^{-2}	.2849	4.351×10^{-2}
.2392	6.034×10^{-2}	.2865	2.798×10^{-2}
.2410	7.401×10^{-2}	.2882	3.081×10^{-2}
.2427	8.967×10^{-2}	.2890	2.308×10^{-2}
.2439	1.024×10^{-1}	.2899	2.401×10^{-2}
.2451	9.872×10^{-2}	.2907	1.630×10^{-2}
.2469	1.194×10^{-1}	.2941	2.003×10^{-2}
.2475	9.031×10^{-2}	.2950	1.238×10^{-2}
.2481	6.026×10^{-2}	.2959	5.706×10^{-3}
.2500	7.207×10^{-2}	.2976	5.688×10^{-3}
.2519	8.391×10^{-2}	.2985	6.625×10^{-3}
.2538	9.772×10^{-2}	.2994	6.613×10^{-3}
.2551	1.105×10^{-1}	.3003	3.773×10^{-3}
.2564	9.299×10^{-2}	.3012	0
.2584	1.117×10^{-1}	.3021	9.397×10^{-4}
.2597	6.175×10^{-2}	.3067	9.306×10^{-4}
.2611	6.961×10^{-2}	.3115	9.206×10^{-4}
.2625	7.747×10^{-2}	.3145	9.141×10^{-4}
.2632	7.355×10^{-2}	.3155	1.824×10^{-3}
.2639	7.845×10^{-2}	.3165	9.096×10^{-4}
.2646	7.355×10^{-2}	.3175	0

TABLE 19. SPECTRAL STERADIANCY NO BETA

λ (μ)	(Watts/Ster.-CC- μ)	λ (μ)	(Watts/Ster.-CC- μ)	λ (μ)	(Watts/Ster.-CC- μ)
.1613	2.434×10^{-3}	.1764	9.351×10^{-2}	.2016	1.069×10^{-1}
.1618	2.459×10^{-3}	.1767	1.108×10^{-1}	.2024	1.181×10^{-1}
.1621	1.977×10^{-3}	.1770	1.081×10^{-1}	.2041	1.071×10^{-1}
.1623	1.987×10^{-3}	.1776	1.034×10^{-1}	.2053	9.892×10^{-2}
.1626	4.493×10^{-3}	.1786	9.632×10^{-2}	.2058	1.017×10^{-1}
.1629	7.023×10^{-3}	.1789	1.161×10^{-1}	.2066	1.165×10^{-1}
.1634	7.093×10^{-3}	.1792	1.353×10^{-1}	.2079	1.073×10^{-1}
.1637	6.619×10^{-3}	.1802	1.259×10^{-1}	.2096	9.654×10^{-2}
.1642	6.684×10^{-3}	.1812	1.168×10^{-1}	.2105	1.108×10^{-1}
.1645	1.085×10^{-2}	.1815	1.139×10^{-1}	.2119	1.021×10^{-1}
.1647	1.506×10^{-2}	.1818	1.338×10^{-1}	.2137	9.178×10^{-2}
.1650	1.461×10^{-2}	.1821	1.525×10^{-1}	.2146	1.072×10^{-1}
.1653	1.468×10^{-2}	.1835	1.378×10^{-1}	.2165	9.752×10^{-2}
.1658	1.376×10^{-2}	.1845	1.277×10^{-1}	.2183	8.946×10^{-2}
.1661	1.383×10^{-2}	.1848	1.455×10^{-1}	.2193	1.024×10^{-1}
.1664	1.336×10^{-2}	.1852	1.628×10^{-1}	.2208	9.494×10^{-2}
.1669	2.698×10^{-2}	.1862	1.506×10^{-1}	.2222	8.734×10^{-2}
.1675	2.560×10^{-2}	.1873	1.395×10^{-1}	.2227	1.021×10^{-1}
.1681	2.474×10^{-2}	.1883	1.317×10^{-1}	.2232	1.014×10^{-1}
.1686	2.386×10^{-2}	.1898	1.190×10^{-1}	.2242	1.055×10^{-1}
.1692	4.369×10^{-2}	.1908	1.100×10^{-1}	.2252	1.003×10^{-1}
.1701	4.089×10^{-2}	.1916	1.286×10^{-1}	.2268	9.163×10^{-2}
.1709	3.800×10^{-2}	.1927	1.187×10^{-1}	.2273	3.616×10^{-2}
.1712	5.206×10^{-2}	.1946	1.039×10^{-1}	.2288	4.940×10^{-2}
.1715	6.508×10^{-2}	.1949	1.097×10^{-1}	.2294	4.855×10^{-2}
.1724	6.066×10^{-2}	.1965	1.002×10^{-1}	.2299	3.647×10^{-2}
.1736	5.515×10^{-2}	.1980	9.053×10^{-2}	.2309	3.377×10^{-2}
.1739	8.912×10^{-2}	.1984	1.098×10^{-1}	.2320	3.576×10^{-2}
.1748	8.297×10^{-2}	.1988	1.283×10^{-1}	.2326	3.487×10^{-2}
.1760	7.573×10^{-2}	.2000	1.184×10^{-1}	.2342	4.355×10^{-2}

TABLE 19. SPECTRAL STERADIANCY NO BETA (Cont.)

λ (μ)	(Watts/Ster.-CC- μ)	λ (μ)	(Watts/Ster.-CC- μ)	λ (μ)	(Watts/Ster.-CC- μ)
.2364	3.903×10^{-2}	.2849	3.674×10^{-2}	.3891	1.143×10^{-2}
.2375	4.199×10^{-2}	.2882	3.177×10^{-2}	.3953	1.046×10^{-2}
.2381	4.109×10^{-2}	.2899	3.553×10^{-2}	.4000	9.576×10^{-3}
.2392	4.693×10^{-2}	.2915	3.257×10^{-2}	.4032	8.778×10^{-3}
.2410	4.229×10^{-2}	.2950	3.143×10^{-2}	.4049	9.391×10^{-3}
.2427	4.532×10^{-2}	.2959	3.328×10^{-2}	.4115	7.834×10^{-3}
.2451	5.033×10^{-2}	.2967	3.133×10^{-2}	.4132	8.428×10^{-3}
.2469	4.561×10^{-2}	.2976	3.223×10^{-2}	.4202	6.931×10^{-3}
.2488	4.182×10^{-2}	.3003	3.018×10^{-2}	.4219	8.131×10^{-3}
.2500	4.870×10^{-2}	.3012	3.107×10^{-2}	.4292	6.675×10^{-3}
.2513	4.681×10^{-2}	.3030	2.814×10^{-2}	.4310	7.226×10^{-3}
.2532	5.274×10^{-2}	.3049	3.457×10^{-2}	.4386	5.832×10^{-3}
.2551	4.793×10^{-2}	.3077	3.065×10^{-2}	.4405	6.363×10^{-3}
.2564	5.188×10^{-2}	.3115	2.578×10^{-2}	.4484	5.593×10^{-3}
.2584	4.801×10^{-2}	.3155	2.280×10^{-2}	.4505	6.100×10^{-3}
.2611	5.196×10^{-2}	.3165	2.365×10^{-2}	.4566	4.861×10^{-3}
.2618	5.001×10^{-2}	.3185	2.262×10^{-2}	.4587	5.352×10^{-3}
.2632	5.001×10^{-2}	.3215	2.872×10^{-2}	.4695	4.088×10^{-3}
.2646	4.413×10^{-2}	.3257	2.574×10^{-2}	.4717	4.555×10^{-3}
.2667	4.020×10^{-2}	.3322	2.003×10^{-2}	.4785	3.932×10^{-3}
.2681	4.606×10^{-2}	.3367	1.805×10^{-2}	.4950	3.658×10^{-3}
.2695	4.408×10^{-2}	.3390	2.219×10^{-2}	.4975	3.167×10^{-3}
.2717	4.306×10^{-2}	.3484	1.904×10^{-2}	.5102	2.569×10^{-3}
.2732	4.009×10^{-2}	.3571	1.366×10^{-2}	.5263	2.395×10^{-3}
.2747	3.712×10^{-2}	.3597	1.673×10^{-2}	.5464	1.829×10^{-3}
.2762	4.000×10^{-2}	.3717	1.373×10^{-2}	.5747	1.619×10^{-3}
.2778	3.800×10^{-2}	.3788	1.114×10^{-2}	.5952	1.187×10^{-4}
.2786	3.895×10^{-2}	.3802	1.256×10^{-2}	.6061	8.502×10^{-4}
.2801	3.694×10^{-2}	.3831	1.169×10^{-2}	.6329	7.597×10^{-4}
.2817	4.271×10^{-2}	.3876	1.077×10^{-2}	.6539	4.650×10^{-4}
				.6667	4.408×10^{-4}

TABLE 20. SUM OF SPECTRAL STERADIANCIES

λ (μ)	(Watts/Ster.-CC- μ)	λ (μ)	(Watts/Ster.-CC- μ)	λ (μ)	(Watts/Ster.-CC- μ)
.0570	1.51×10^{-2}	.0707	3.21×10^1	.0923	7.03×10^2
.0573	2.28×10^{-2}	.0712	3.88×10^1	.0935	8.38×10^2
.0577	2.94×10^{-2}	.0717	4.68×10^1	.0943	9.93×10^2
.0580	3.72×10^{-2}	.0723	5.63×10^1	.0952	1.17×10^3
.0583	4.63×10^{-2}	.0728	6.75×10^1	.0962	1.38×10^3
.0587	5.73×10^{-2}	.0733	8.04×10^1	.0971	1.60×10^3
.0590	7.13×10^{-2}	.0739	9.53×10^1	.0980	1.85×10^3
.0594	8.79×10^{-2}	.0744	1.12×10^2	.0990	2.14×10^3
.0597	1.10×10^{-1}	.0750	1.32×10^2	.1000	2.45×10^3
.0601	1.365×10^{-1}	.0755	1.53×10^2	.1010	2.78×10^3
.0605	1.55×10^{-1}	.0761	1.78×10^2	.1020	8.17×10^2
.0608	1.81×10^{-1}	.0767	2.05×10^2	.1031	9.97×10^2
.0612	2.16×10^{-1}	.0773	2.35×10^2	.1042	1.21×10^3
.0616	2.71×10^{-1}	.0779	2.68×10^2	.1053	1.48×10^3
.0620	3.32×10^{-1}	.0785	3.05×10^2	.1064	1.79×10^3
.0623	4.33×10^{-1}	.0791	3.46×10^2	.1070	8.76×10^2
.0627	5.50×10^{-1}	.0797	3.93×10^2	.1081	1.06×10^3
.0631	6.88×10^{-1}	.0804	4.45×10^2	.1093	1.28×10^3
.0635	9.36×10^{-1}	.0810	5.02×10^2	.1105	1.54×10^3
.0639	1.27	.0817	5.67×10^2	.1117	1.85×10^3
.0644	1.63	.0824	6.39×10^2	.1130	2.22×10^3
.0648	2.02	.0831	7.20×10^2	.1135	6.93
.0652	2.55	.0838	8.09×10^2	.1148	8.50
.0656	3.22	.0845	9.09×10^2	.1161	1.04×10^1
.0661	3.94	.0852	1.02×10^3	.1175	1.27×10^1
.0665	4.93	.0855	6.03×10^2	.1189	1.56×10^1
.0669	6.14	.0862	6.86×10^2	.1203	1.90×10^1
.0674	7.64	.0870	7.93×10^2	.1218	2.32×10^1
.0678	9.44	.0877	9.17×10^2	.1233	2.835×10^1
.0683	1.17×10^1	.0885	1.04×10^3	.1248	3.46×10^1
.0688	1.43×10^1	.0893	1.18×10^3	.1264	4.21×10^1
.0693	1.77×10^1	.0901	1.34×10^3	.1280	5.13×10^1
.0697	2.16×10^1	.0909	1.51×10^3	.1297	6.235×10^1
.0702	2.63×10^1	.0917	5.88×10^2	.1314	7.58×10^1

TABLE 20. SUM OF SPECTRAL STERADIANCIES (Cont.)

$\lambda (\mu)$	(Watts/Ster. -CC- μ)	$\lambda (\mu)$	(Watts/Ster. -CC- μ)
.1675	5.69×10^{-1}	.7299	8.46
.1779	1.13	.7353	7.86
.195	2.92	.7576	8.30
.2105	4.99	.7634	8.16
.225	1.02×10^1	.7692	8.27
.255	2.58×10^1	.7752	7.86
.293	5.69×10^1	.7874	8.08
.294	2.91×10^1	.7937	6.07
.302	3.34×10^1	.8000	6.16
.303	2.92×10^1	.8065	3.99
.3205	3.91×10^1	.8130	2.32
.3215	3.06×10^1	.9174	2.89
.3425	3.95×10^1	.9259	2.81
.3436	1.92×10^1	.9434	2.58
.353	3.42×10^1	.9524	1.60
.3663	2.01×10^1	.9709	1.06
.390	3.84×10^1	1.010	9.43×10^{-1}
.4098	3.90×10^1	1.10	8.01×10^{-1}
.4202	4.51×10^1	1.282	8.17×10^{-1}
.4219	4.31×10^1	1.299	8.02×10^{-1}
.430	4.36×10^1	1.333	8.00×10^{-1}
.4425	4.08×10^1	1.429	7.76×10^{-1}
.4444	2.15×10^1	1.449	5.58×10^{-1}
.4566	2.37×10^1	1.639	5.25×10^{-1}
.4587	1.41×10^1	1.724	4.97×10^{-1}
.470	1.23×10^1	1.818	4.81×10^{-1}
.4854	1.34×10^1	2.000	4.52×10^{-1}
.4878	5.26	2.222	4.16×10^{-1}
.5102	6.06	4.17	2.50×10^{-1}
.5128	3.12	5.26	2.04×10^{-1}
.5714	4.39	7.14	1.53×10^{-1}
.6579	6.68	10.0	1.08×10^{-1}

NOMENCLATURE

A	radiometer collector surface area
B_v	rotational constant
B	Planck's black body function
c	velocity of light
D	frontal diameter
$\frac{D}{Dt}$	substantial derivative
e	electronic charge
f_{nm}	oscillator strength of process n to m
Fr	radiation - flow field coupling ratio
F_s	spectral radiation factor
g	statistical weight factor
$G_{er, v}$	energies of the electronic-vibrational term value
h	Planck's constant
h	enthalpy
J	radiance
k	Boltzmann constant
L	thickness of gas
m	mass of electron
N	number density
p	pressure
Pr	Prandtl Number
\dot{q}	heat flux
Q	total partition function
r	radius
R	gas constant
Re	Reynolds Number
s	wetted length

S	entropy
T	temperature
U	velocity
V	gas volume
X	axial distance
Z	compressibility factor
α	absorptance coefficient
γ^*	equivalent ratio of specific heat
δ	incremental streamline length
Δ	distance of body to flow separation boundary
ϵ	emissivity
ξ	coordinate in subsonic solution
η	coordinate in subsonic solution
θ	angle from body normal
λ	wave length
μ_e	viscosity
ν	frequency of the band head
Π	indicates a product operator
ρ	density
σ_c	collision cross section
σ	Stefan - Boltzmann constant
$\tilde{\tau}$	transmittance
Σ	indicates a summation operator
ϕ	angle around body normal
Ψ	stream function

SUBSCRIPTS

e	edge boundary layer
i	incremental
L	laminar
O	stagnation point
r	recovery
T	turbulent
W	Wall
HG	hot gas radiation
LD	laminar detached
RR	re-radiation
TD	turbulent detached
Δ	based on distance Δ
λ	wave length
ν	wave number
∞	free stream

SUPERSCRIPTS

*	Eckert's reference conditions
---	-------------------------------

REFERENCES

1. F. G. Gravalos, I. H. Edelfelt, and H. W. Emmons. The Supersonic Flow about a Blunt Body of Revolution for Gases at Chemical Equilibrium. Proceedings of the 9th Annual Congress of the International Astronautical Federation, Amsterdam, 1958.
2. Photographs of Separation Lines for Apollo Vehicle in Hypersonic Flow, Provided by R. Dingeldein, NASA Langley Research Center.
3. W. Langan, and W. McCauley, ARP System Study Report, G.E. TIS 63SD593, 1963
4. E. S. Love, Base Pressure at Supersonic Speeds on Two Dimensional Air Foils and on Bodies of Revolution with and without Fins, having Turbulent Boundary Layers, NACA TN3819, 1957.
5. E. A. Brong, Solution of the Prandtl-Meyer Equation for Real, Equilibrium, γ^* Gas, G. E. TIS 59SD445, 1959
6. F. G. Gravalos and E. A. Brong, Report on the Flow Field Solution in the Subsonic Region, to be published.
7. H. W. Ridyard and E. M. Storer, Stagnation Point Shock Detachment of Blunt Bodies in Supersonic Flow, G. E. MSD ADM 136, 1962
8. D. E. Nestler and L. Musser, Correlations for Convective Heat Transfer, Pressure Distribution and Shock Detachment Distance for Blunt Axisymmetric Forebodies, G. E. MSD AETM 149, 1960.
9. W. G. Browne, Thermodynamic Properties of the Earth's Atmosphere, G.E. MSD RSPTM 2, 1962

10. L. Dewees, Re-entry Vehicle Design (Ablating) Program, G. E. -MSD Report TIS-R59SD391, July, 1959
11. G. Walker, A Particular Solution to the Turbulent Boundary Layer Equations, GE-MSD Report AETM-156, April 1960
12. J. G. Logan and C. E. Treanor, Tables of Thermodynamic Properties of Air from 3,000^oK to 10,000^oK at Intervals of 1,000^oK, Cornell Aeronautical Laboratory Report No. BE-1007-4-3, January 1957.
13. L. Dewees, Afterbody Design Program, GE-MSD Report TIS R59SD393, July 1959.
14. T. Shaw, et al, Final Summary of Aerothermodynamic Analysis, MK 2 Flight Test Data, GE-MSD Report TIS-R60SD481, January 1961 (Secret-Title Unclassified)
15. Breene, et al, Radiance of Species in High Temperature Air, GE-MSD Report TIS-R63SD3, June 1963.
16. C. V. Dohner, Hot Gas Radiation Program Procedure, GE-MSD Report PIR-HTT-8151-081, March 1963.
17. Breene, et al, Radiance of Species in High Temperature Air, GE-MSD Report TIS-R62SD52, July 1962.
18. Wood, Deem, and Lucks, Thermal Radiative Properties of Selected Materials, Battelle Memorial Institute DMIC Report 177, Volume 2 of 2, November 1962.